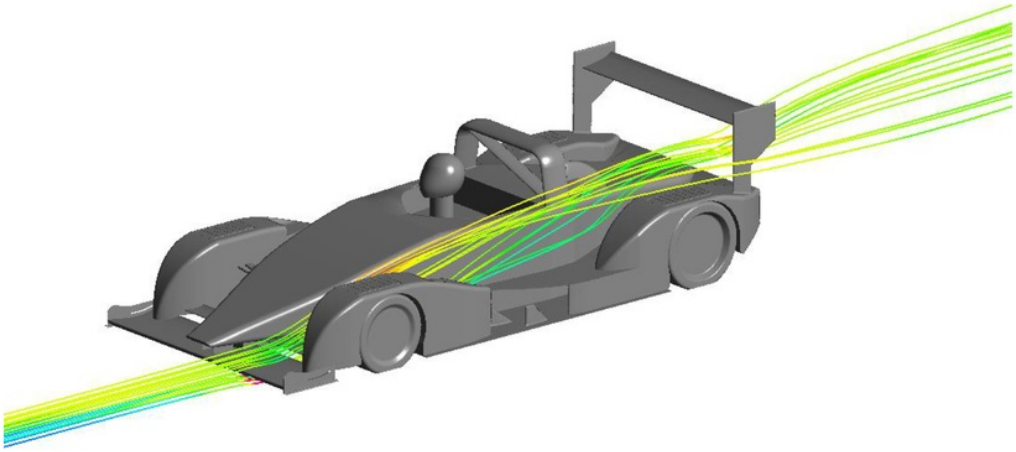
# Major Project Report

*by* John Michael Hughes


| | | | |
|---|---|---|---|
| FILE | 4209_JOHN_MICHAEL_HUGHES_MAJOR_PROJECT_REPORT_128469_1947701621.DOCX (19.78M) | | |
| TIME SUBMITTED | 26-APR-2019 08:53PM (UTC+0100) | WORD COUNT | 22064 |
| SUBMISSION ID | 105470018 | CHARACTER COUNT | 163280 |

Prifysgol Cymru
Y Drindod Dewi Sant
University of Wales
Trinity Saint David



# Aerodynamic Development and Optimisation of the Front Wing Concept for an MCR Race Car in the Open Sports Series Championship.


John Michael Hughes

P146322

BEng Motorsport Engineering

Year 3


Major Project: M6X00417

Supervisor: Tim Tudor

13th March 2019

## Abstract

This report numerically analyses the development of a multi-element front wing concept designed for an Open Sports Series Prototype racing car to replace its standard splitter geometry. Utilising Solidworks CAD and Ansys Simulation software, a series of design iterations are performed and critically analysed to gain further frontal downforce bias and maintain efficiency.

A series of standardised profiles are examined in isolation through the use of 3D CFD simulations and decisions made on profile combinations are discussed.

DOE software is utilised to then optimise design variables, such as height, AoA, overhang and chord length to find the best performing profile arrangement to subsequently be implemented upon the car in question.

An end plate development scheme is then conducted to further optimise the performance of the newly developed wing concept.

A further attitude study involving height, pitch and yaw is conducted to then build a minor aerodynamic map of the whole car to optimise its aerodynamic setup in a steady state situation.



## Acknowledgements

I would like to thank Tim Tudor for his continued dedication to further develop my understanding of aerodynamic principles and how they can be applied to a potential scenario. His constant guidance has pushed me to understand the impact of aerodynamics on car handling, thus allowing me to make well informed decisions regarding aerodynamic concepts.

Further appreciation is given to John Iley for taking time out of a busy schedule to help me gain confidence within my abilities and trust the decisions I make. Providing technical knowledge on aerodynamic characteristics regarding bodywork components considered for this project has proved valuable.

## Confirmation of Own Work

This thesis is the result of the author's personal research and conducted work. It has been composed by the author with all relevant research cited and has not been previously submitted for examination for the award of an honour's degree.

Confirmation of work:

Signed:……

Date:……

# Contents


Abbreviations ..... 6

Figures, Graphs, Tables & Equations ..... 7

1.0.0 Introduction ..... 13

1.1.0 Aims ..... 15

2.0.0 Literature Review ..... 19

2.1.0 MCR Race Cars ..... 19

2.2.0 Open Sports Series Championship (OSS) ..... 21

2.2.1 Regulations ..... 21

2.3.0 Wing Theory ..... 23

2.3.1 Boundary Layer ..... 25

2.3.2 Separation ..... 26

2.3.3 Multi – element Wings ..... 28

2.3.4 Ground Effect ..... 30

2.4.0 Aerodynamic Balance ..... 32

2.5.0 Computational Fluid Dynamics (CFD) ..... 33

2.5.1 Domain (Pre – processing) ..... 33

2.5.2 Mesh (Pre – processing) ..... 33

2.5.3 Solving (Processing) ..... 34

3.0.0 CFD Methodology Validation ..... 36

3.1.0 MIRA Car Validation Study ..... 37

3.2.0 Naca 0012 Wind – Tunnel Validation Study ..... 39

3.3.0 Wing Profile Flow Visualisation Validation Study ..... 42

3.4.0 Baseline MCR Sports2000 CFD Comparison ..... 45

4.0.0 Initial Geometries ..... 46

4.1.0 Baseline Geometry (JHTT02) ..... 46

4.2.0 Non–iterative Geometry Development ..... 50

5.0.0 Methodology, Results & Analysis ..... 53

5.1.0 Aerofoil Selection ..... 53
5.2.0 Naca 4412 & S1223 Profiles ..... 56
5.2.1 Height Study (Naca 4412 & S1223) ..... 61
5.2.2 Angle of Attack Study (AoA) (Naca 4412 & S1223) ..... 67
5.3.0 Design of Experiments ..... 72
5.3.1 Main Plane - S1223: Height vs AoA ..... 72
5.3.2 Main Plane Discussion ..... 74
5.3.3 S1223 Main Plane Optimisation ..... 74
5.4.0 Secondary Element – Naca 4412: Height vs AoA vs Positive Overhang ..... 79
5.5.0 Secondary Element – S1223: Height vs AoA vs Positive Overhang ..... 82
5.5.1 Secondary Element Discussion ..... 84
5.5.2 S1223 Secondary Element DOE (Height vs Chord Length vs Increased AoA) ..... 90
5.5.3 S1223 Secondary Element Optimisation Study ..... 95
5.5.4 S1223 Secondary Element Negative Overhang Study ..... 99
5.6.0 Isolation Comparison (New Wing vs Baseline Splitter) ..... 103
5.6.1 Modified Main Plane ..... 107
6.0.0 Whole Car Study ..... 112
6.1.0 End Plate Development ..... 117
6.2.0 Attitude Study ..... 122
6.2.1 Height ..... 122
6.2.2 Static Pitch ..... 123
6.2.3 Dynamic Pitch ..... 124
6.2.4 Yaw ..... 126
7.0.0 Conclusion & Evaluation ..... 128
7.1.0 Recommended Further Work ..... 131
8.0.0 References ..... 132
9.0.0 Appendix A ..... 137
10.0.0 Appendix B ..... 146
11.0.0 Appendix C ..... 147

12.0.0 Appendix D ..... 151

## Abbreviations

- $CFD$ – Computational Fluid Dynamics
- $CAD$ – Computer Aided Design
- $Cd$ – Coefficient of Drag
- $Cl$ – Coefficient of Lift
- $\rho$ – Air Density
- $V$ – Velocity
- $A$ – Area
- $CP$ – Centre of Pressure
- $CoP$ – Coefficient of Pressure
- $N$– Newtons
- $OSS$ – Open Sports Series
- $MSUK$ – Motorsport United Kingdom
- $Re$ – Reynolds Number
- $l$ – Length
- $\mu$ – Dynamic Viscosity
- $c$ – Chord Length
- $CoG$ – Centre of Gravity
- $RANS$ – Reynolds Averaged Navier Stokes
- $u, v, w$ – Velocity Components
- $p$ – Pressure
- $\tau$ – Shear Stress
- $E_t$ – Energy Total
- $p_r$ – Prandtl Number
- $q$ – Heat Flux
- $k\varepsilon$ – K-Epsilon
- $k\omega$ – K-Omega
- $P$ – Pressure
- $P_s$ – Static Pressure
- $h$ - Height
- $DOE$ – Design of Experiment
- $Vmax$ – Maximum Velocity

## Figures, Graphs, Tables & Equations

Figure 1 - LMP1 (Left) and LMGPT (Right) Race Cars (Carney, 2016) (Brookes, 1999) .....13
Figure 2 - Flow Around a Cylinder (Machin , 2015) .....16
Figure 3 - JHTT02 MCR Sports2000 Prototype Concept .....16
Figure 4 - Centre of Pressure on a Wing (The Great Soviet Encylopedia, 1979) .....17
Figure 5 - Performance Objective .....17
Figure 6 – UWTSD Team MCR Sports2000 Race Car (University of Wales Trinity Saint David, 2018).....19
Figure 7 - MCR Race Cars Splitter Design .....19
Figure 8 - MCR Race Cars Open Sports Series (OSS) Race Car (MCR Race Cars, Sports Racing Car Manufacturers, 2019).....20
Figure 9 - OSS/MSUK Regulation Reference Boxes .....22
Figure 10 - Aerofoil Diagram (Birchall, 2011).....23
Figure 11 - Wing Recirculation (Glownia, 2007) .....24
Figure 12 - Boundary Layer (Banihani, 2018).....25
Figure 13 - Flow Separation (history.nasa.gov, 2010) .....26
Figure 14 - Eddie Formulation (Fletcher, et al., 2014) .....27
Figure 15 - Cl vs AoA (Seljak, 2008).....27
Figure 16 - Multi - Element Aerofoil (Jackson, 2018).....28
Figure 17 - Multi - Element Wing Element Configurations (Craig & Passmore, 2014).....29
Figure 18 - Gap Size & Overlap Sensitivity Study (Craig & Passmore, 2014).....30
Figure 19 - Aerofoil in Ground Effect (S1223) (Mokhtar & Durrer, 2016).....30
Figure 20 - Aerofoil in Freestream (S1223) (Mokhtar & Durrer, 2016).....31
Figure 21 - Downforce Distribution (CP) (Quintarelli, 2018) .....32
Figure 22 - Surface & Volume Mesh (Using a Symmetry Plane) (symscape, 2013) .....33
Figure 23 - Mass Flows per Mesh Element (Sergio, 2017).....35
Figure 24 - C2 Open Loop Wind Tunnel .....39
Figure 25 - C2 Open Loop Virtual Wind Tunnel .....39
Figure 26 - C2 Wind Tunnel CFD Velocity Contours (15°) .....41
Figure 27 - Naca 0012 15° Recirculation .....41
Figure 28 - Velocity Streamlines Showing Recirculation Naca 0012 (15°) .....41
Figure 29 - Wing Lower Surface Flow Visualisation Paint Test .....42
Figure 30 - Wing Lower Surface Recirculation .....42
Figure 31 - MCR Sports2000 Rear Wing Circuit Flow Visualisation Test .....43
Figure 32 - MCR Sports2000 Rear Wing Velocity Contours (5.1°) .....43
Figure 33 - MCR Sports2000 Rear Wing Mount Interaction .....44

Figure 34 - MCR Sports2000 Rear Wing Mount Interaction Flow Visualisation.....44
Figure 35 - MCR Sports2000 Baseline Geometry .....45
Figure 36 - Baseline Geometry (JHTT02).....46
Figure 37 - JHTT02 Splitter Velocity Contours .....46
Figure 38 - JHTT02 Splitter Pressure Contours (Lower Surface) .....47
Figure 39 - JHTT02 Splitter Vortex Generation (Lower Surface).....47
Figure 40 - Concept 1 & 8 Pressure Contours.....51
Figure 41 - Concept 1 & 8 Velocity Contours.....51
Figure 42 - Standardised Aerofoils (Velocity Contours).....55
Figure 43 - Naca 4412 & S1223 Surface Pressure Contours .....56
Figure 44 - Naca 4412 & S1223 Upper Surface Vortices .....58
Figure 45 - S1223 Trailing Edge Velocity Vectors (Vortex) .....59
Figure 46 - Naca 4412 & S1223 Lower Surface Vortices .....59
Figure 47 - Leading Edge Vortex Generation .....60
Figure 48 - Naca 4412 & S1223 Maximum & Minimum Heights (Pressure Contours) .....61
Figure 49 - Naca 4412 & S1223 Maximum & Minimum Heights (Velocity Contours) .....62
Figure 50 - S1223 10mm (Velocity Vectors) .....62
Figure 51 - Height vs -Cl & Cd (Katz, 1995) .....64
Figure 52 - Naca 4412 & S1223 Lower Surface Pressure Contours (1° - 15°).....67
Figure 53 - Naca 4412 & S1223 Velocity Contours (1° - 15°).....67
Figure 54 - Naca 4412 & S1223Velocity Streamlines (15°).....68
Figure 55 - S1223 Main Plane DOE Optimisation Velocity Contours .....77
Figure 56 - S1223 Main Plane DOE Optimisation Lower Surface Pressure Contours .....78
Figure 57 - Naca 4412 & S1223 Minimum & Maximum Cl Velocity Contours .....84
Figure 58 - S1223 Secondary Element Chord DOE Study Velocity Contours.....92
Figure 59 - Chord Length Study Vortex Generation .....94
Figure 60 - S1223: Secondary Element DOE Optimisation (Lower Surface Pressure Contours) .....97
Figure 61 - Secondary Element Negative Overhang (0mm & 30mm) (Velocity Contours) ..100
Figure 62 - Trailing Edge Vortex .....101
Figure 63 - Secondary Element Overhang (0mm - 30mm) (Lower Surface Pressure Contours) .....101
Figure 64 - Baseline Splitter vs New Concept (Lower Surface Pressure Contours) .....103
Figure 65 - Baseline Splitter vs New Concept Vortices .....104
Figure 66 - Baseline Splitter vs New Concept (Velocity Contours).....105
Figure 67 - Modified Main Plane .....107
Figure 68 - Modified & Standard Main Plane Velocity Contours.....109

Figure 69 –Modified & Standard Main Plane Lower Surface Pressure Contours .....110
Figure 70 - Lower Surface Pressure Stagnation .....112
Figure 71 - New Concept vs Baseline (Velocity Contours) .....112
Figure 72 - New Concept vs Old Concept Pressure Contours .....113
Figure 73 - Front Pontoon Geometry Change .....113
Figure 74 - New Concept & Baseline Edge Vortices .....115
Figure 75 - Splitter Edge Vortex Velocity Contours .....115
Figure 76 - End Plate Development Geometries .....117
Figure 77 - End Plate Development Velocity Contours .....117
Figure 78 - End Plate Development 1 & 5 Pressure Vectors .....118
Figure 79 - End Plate Development Pressure Bleed .....119
Figure 80 - Wing Edge Velocity Contours .....119
Figure 81 - End Plate Development Vortices .....120
Figure 82 - Symmetry Plane Pressure Contours .....124
Figure 83 - Yaw Angle Pressure Contours .....126

Graph 1 - MIRA Car Pressure Distribution (CFD Validation) (Hughes, 2018) .....37
Graph 2 - Naca 0012 Wind Tunnel vs CFD (0°) .....40
Graph 3 - Naca 0012 Wind Tunnel vs CFD (15°) .....40
Graph 4 - JHTT02 Baseline Surface Pressure Distribution .....48
Graph 5 - Non-Iterative Development Cl & Cd .....50
Graph 6 - Concepts 1 & 8 Surface Pressure Distribution .....52
Graph 7 - Standardised Aerofoils - Cl & Cd .....54
Graph 8 - Naca 4412 Pressure Distribution .....57
Graph 9 – S1223 Pressure Distribution .....57
Graph 10 - Naca 4412 & S1223 - Height vs Cl .....63
Graph 11 - Naca 4412 & S1223 - Height vs Cd .....63
Graph 12 - Naca 4412 Pressure Distribution (10mm & 140mm) .....65
Graph 13 - S1223 Pressure Distribution (10mm & 140mm) .....65
Graph 14 - Naca 4412 & S1223 - Height vs Efficiency .....66
Graph 15 – Naca 4412 & S1223 – AoA vs Cl .....69
Graph 16 - Naca 4412 & S1223 - AoA vs Cd .....69
Graph 17 - Naca 4412 & S1223 - AoA vs Efficiency .....70
Graph 18 - Naca 4412 Pressure Distribution (1° - 15°) .....71
Graph 19 - S1223 Pressure Distribution (1° - 15°) .....71
Graph 20 - S1223 Main Plane DOE Study (Cl) .....72

Graph 21 - S1223 Main Plane DOE Study (Cd) ....73
Graph 22 - S1223 Main Plane - Cl Optimisation Study....75
Graph 23 - S1223 Main Plane - Cd Optimisation Study ....76
Graph 24 – S1223 Main Plane – DOE Optimisation Efficiency ....76
Graph 25 - S1223 DOE Optimisation Pressure Distribution ....78
Graph 26 - Naca 4412 Secondary Element DOE Study (Cl) ....79
Graph 27 - Naca 4412 Overhang Influence (Cl) (0mm Overhang) ....80
Graph 28 - Naca 4412 Secondary Element DOE Study (Cd) ....80
Graph 29 – Naca 4412 Overhang Influence (Cd) (0mm Overhang) ....81
Graph 30 - S1223 Secondary Element DOE Study (Cl) ....82
Graph 31 - S1223 Overhang Influence (Cl) (0mm Overhang) ....82
Graph 32 - S1223 Secondary Element DOE Study (Cd) ....83
Graph 33 - S1223 Overhang Influence (Cd) (0mm Overhang)....83
Graph 34 - Naca 4412 Secondary Element Pressure Distribution (12.9754mm/0°/37.0246mm) ....85
Graph 35 - Naca 4412 Secondary Element Pressure Distribution (32.115mm/9.875°/8.01002mm) ....86
Graph 36 - Naca 4412 Secondary Element DOE Study (Cl & Cd) ....86
Graph 37 – S1223 Secondary Element Pressure Distribution (27.0619mm/0°/22.9381mm) 87
Graph 38 – S1223 Secondary Element Pressure Distribution (41.6686mm/8.33141°/0mm) 88
Graph 39 – S1223 Secondary Element DOE Study (Cl & Cd) ....89
Graph 40 - S1223 Secondary Element DOE Study 2 (Cl) (25% Chord)....90
Graph 41 - S1223 Secondary Element DOE Study 2 (Cl) (100% Chord)....91
Graph 42 - S1223 Secondary Element DOE Study 2 (Cd) (25% Chord)....91
Graph 43 - S1223 Secondary Element DOE Study 2 (Cl) (100% Chord)....92
Graph 44 - S1223 Secondary Element Chord Length Pressure Distribution....93
Graph 45 - S1223: Secondary Element DOE Optimisation (Cl & Cd) ....95
Graph 46 – S1223: Secondary Element DOE Optimisation (Efficiency)....96
Graph 47 - S1223: Secondary Element DOE Optimisation (Forces)....97
Graph 48 - S1223: Secondary Element Negative Overhang (Cl & Cd) ....99
Graph 49 - S1223: Secondary Element Negative Overhang (Efficiency) ....100
Graph 50 - Frontal Balance (%) ....102
Graph 51 - Baseline vs New Concept Pressure Distribution ....105
Graph 52 - Splitter Concepts Cl & Cd....108
Graph 53 - Splitter Concepts Efficiency ....109
Graph 54 - Wall Shear: Modified & Standard New Concept ....110
Graph 55 - New Concept: Modified Main Plane Pressure Distribution ....111

Graph 56 - New Concept vs Old Concept Pressure Distribution ....114
Graph 57 - End Plate Development Cl & Cd....120
Graph 58 - End Plate Development Efficiency & Balance ....121
Graph 59 - Height Cl & Cd ....122
Graph 60 - Height Efficiency & Balance....122
Graph 61 - Static Pitch Cl & Cd ....123
Graph 62 - Static Pitch Efficiency & Balance ....123
Graph 63 - Dynamic Pitch Cl & Cd ....124
Graph 64 - Dynamic Pitch Efficiency & Balance ....125
Graph 65 - Yaw Study Cl & Cd ....126
Graph 66 - Yaw Study Efficiency & Balance ....127
Graph 67 - Resulting Cl & Cd ....128
Graph 68 - Total Forces....129
Graph 69 - Front + Rear Downforce & Balance ....129

Table 1 - OSS Championship Class Categories....21
Table 2 - Maximum & Minimum CoP Comparison....38
Table 3 - MCR Sports2000 Baseline CFD vs TotalSim MCR Sports2000 Baseline CFD....45
Table 4 - JHTT02 Baseline Specification....48
Table 5 - Non-Iterative Aerodynamic Development Results ....50
Table 6 - Standardised Aerofoils....53
Table 7 - S1223 Main Plane DOE Maximum & Minimum Input Variables ....72
Table 8 - S1223 Main Plane DOE Study Results ....74
Table 9 - S1223 Main Plane Optimisation Desirability Factors....74
Table 10 - Naca 4412 & S1223 Secondary Element Input Variables ....79
Table 11 - Naca 4412 Secondary Element Arrangements & Efficiencies....87
Table 12 - S1223 Secondary Element Arrangements & Efficiencies....89
Table 13 - S1223 Secondary Element Input Variables ....90
Table 14 - Chord Length Comparison....93
Table 15 - S1223 Secondary Element DOE Optimisation Desirability....95
Table 16 - Baseline Splitter & New Concept Aerodynamic Specification ....103
Table 17 - Splitter Concept (Drag & Downforce) ....108
Table 18 - New Concept vs Baseline Specifications....114
Table 19 - Baseline Car & New Concept Car Specifications ....121
Table 20 – Final Results ....128

Equation 1 - Drag Force....15
Equation 2 - Lift Force....15
Equation 3 - Aerodynamic Efficiency....17
Equation 4 - Bernoulli's Theorem....23
Equation 5 - Reynolds Number....25
Equation 6 - Aspect Ratio....28
Equation 7 - CP Balance %....32
Equation 8 - Navier Stokes....34
Equation 9 - Coefficient of Pressure (CoP)....37
Equation 10 - Distance to Ground Ratio....61

## 1.0.0 Introduction

This report will focus on the development and optimisation of a front wing concept for an MCR Race Cars, OSS Championship car.

The concept of wings within motorsport culture has been prominently exploited for several decades. The approach is to use a lift generating device, thus creating a downward direction of force, otherwise known as downforce.

The two key areas of interest in aerodynamic performance manifest themselves as downforce and drag, each of which plays a crucial role in the dynamic handling of the concerned vehicle when these forces are exerted (Abdulwahab, 2015). As drag is the aerodynamic resistive force acting against the motion of the vehicle, engineering the best downforce to drag ratio is paramount to the overall performance of the vehicle, the aim being to achieve an increase in downforce and a decrease in drag.

The most prominent use of aerodynamics within motorsport is evident within the world of Formula One, however many other series of motorsport, such as sports prototype race cars, pride themselves on the use of aerodynamic devices. However, differing series also exist within this type of race car, the highest profile being the FIA World Endurance Championship, within which the Le Mans 24-hour race is staged (Carney, 2016). The high specification sports prototype comes in the form of an LMP1 race car, which is an evolution of the LMGPT race car (Dominy, 2002).



*Figure 1 - LMP1 (Left) and LMGPT (Right) Race Cars (Carney, 2016) (Brookes, 1999)*

As *Figure 1* above illustrates, both generations of sports prototype extensively employ the use of aerodynamic devices, however, the LMP1 Audi R18 appears visually further advanced.

However, as these devices can prove to be the decisive factor between winning and losing, most racing teams keep the aerodynamic performance of their cars restricted to in house employees only.

Traditional methods of aerodynamic testing involve the use of wind tunnels and road testing, both of which are still widely used and trusted methods, however, most have recently been superseded by the use of Computational Fluid Dynamics as a result of advancements in the availability of computational power (Katz, 1995).

## 1.1.0 Aims

As aerodynamics play such a prominent role within modern day motorsport, the aerodynamic balance of the car has become a critical area for development and optimisation.

The resistive drag force produced by a race car is a vital area of analysis. As the equation below shows, drag force is relative to velocity squared. Therefore, as the velocity of the vehicle increases, so does the resistive force.

$$Drag\ Force\ (N) = \frac{1}{2}\ \rho\ Cd\ A\ V^2$$

*Equation 1 - Drag Force*

As *Equation 1* illustrates, drag is also subject to air density ($\rho$), which can differ with each circuit. As observed by NASA at the Glenn Research Centre, drag force increases linearly with air density, so if the density is halved, the drag force is also halved (www.grc.nasa.gov, 2018).

$$Lift\ Force\ (N) = \frac{1}{2}\ \rho\ Cl\ A\ V^2$$

*Equation 2 - Lift Force*

This assertion likewise applies to the produced lift (downforce), which also has a linear relationship with air density, and, therefore, this also needs to be considered. It must also be stated, that as the frontal area (A) increases, so does the produced drag and downforce, however, this is in terms of a bluff body (a body that, as a result of its shape, has separated flow over a substantial part of its surface). If it is referring to a wing, the planar area is used.

It can, however, be observed in *Equations 1* and *2*, that a number of relationships exist. It is for this reason that where an increase in downforce exists, an increase in drag will also be present. The aim, therefore, is to produce a ratio of the two factors that accommodate the demands of the vehicle and the proposed aerodynamic requirement.

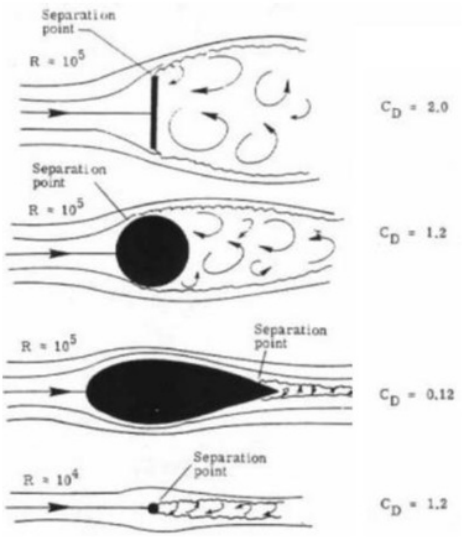



*Figure 2 - Flow Around a Cylinder (Machin , 2015)*

*Figure 2* illustrates how the shape of a given object can affect the flow characteristics around the object in question. Of the shapes illustrated it can be observed that the tear drop shape produces a much lower Cd (coefficient of drag) value than that of a flat plate or cylinder.

This characteristic is evident on many sports prototype cars, including the geometry in the case of this study.

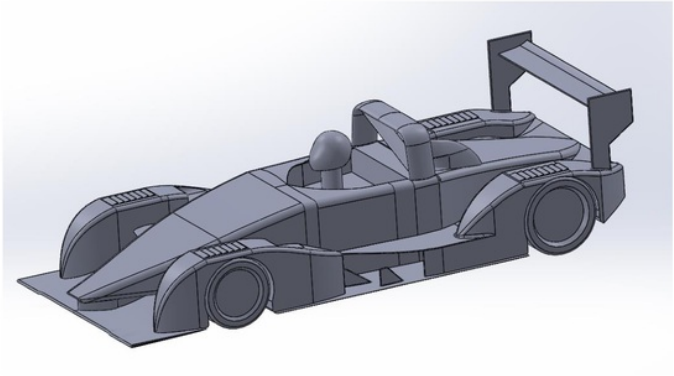


*Figure 3 - JHTT02 MCR Sports2000 Prototype Concept*

*Figure 3* illustrates a bodywork concept design for an MCR Race Cars, Sports 2000 race car, created at the University of Wales Trinity Saint David in collaboration with MCR Race Cars.

The objective of the motorsport aerodynamicist is to produce as much downforce as possible, with as little drag as possible. However, if the downforce produced is concentrated

on a particular area of the vehicle, the handling characteristics of the vehicle can be dramatically influenced in a negative manner. Therefore, the distribution of downforce is a significant aspect of aerodynamic development.

This approach demonstrates why Cp (centre of pressure) is so critical.

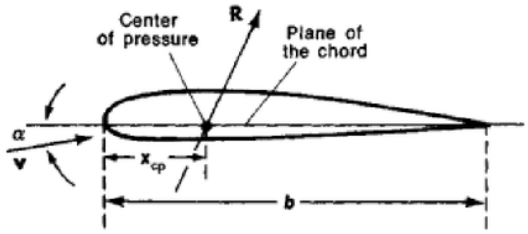



*Figure 4 - Centre of Pressure on a Wing (The Great Soviet Encylopedia, 1979)*

Cp describes the point at which the resultant lift force acts, as illustrated in *Figure 4* (McGraw-Hill Concise Encyclopedia of Physics, 2002). In this diagram, b is the chord length, v is velocity, R is the resultant force vector, Xcp is the distance from the leading edge to the Cp, and $\alpha$ is the angle of attack of the wing.

All of these methods, and more, need to be considered within the scope of this study, the purpose of which is to develop the front splitter employing the concept illustrated in *Figure 3*, in order to optimise track performance.

$$Aerodynamic\ Efficiency = \frac{Cl}{Cd}$$

*Equation 3 - Aerodynamic Efficiency*

The object of the exercise being to improve its overall performance over a wider range of circuits. It follows that aerodynamic efficiency (*Equation 3*) and Cp will perform fundamental roles in the development process of the new design.




*Figure 5 - Performance Objective*

As *Figure 5* illustrates, that the objective is to increase the performance window in which the car will operate. This may result in a reduction in the peak downforce produced by the vehicle (Iley, 2018). However, the outcome could be a greater aerodynamic performance over the course of a racing season and over a wider range of circuits.

The reason for this approach is due to the subsequent differing demands of each circuit. If a circuit incorporates fast sweeping corners, peak downforce may not be essential as downforce is relative to velocity, but a shorter, tighter cornered circuit may require a greater peak downforce, due to the low velocity nature of the circuit. Therefore, the aim of this study is to develop a splitter concept that produces a balanced aerodynamic performance.

To summarise, a splitter design will be developed based on the aerodynamic concept illustrated in *Figure 3* with the aim of enhancing its overall circuit performance over a wider range of circuits. This will therefore produce vehicle handling consistency, making the car more predictable for the driver.

## 2.0.0 Literature Review

The generation of ideas for the production of aerodynamic enhancements begins with extensive research into general concepts and then implementation employing a baseline geometry. This section will outline the development of the general concept and the in-depth research required to further advance the influence of the component on the race car.

### 2.1.0 MCR Race Cars



*Figure 6 – UWTSD Team MCR Sports2000 Race Car (University of Wales Trinity Saint David, 2018)*

Traditionally, the race car manufacturer, MCR Race Cars develop and manufacture race cars for the SRCC Sports 2000 racing series. As illustrated by the photograph above (*Figure 6*), the car is an open cockpit sports prototype based closely on traditional sports prototype vehicles. The chassis comprises a tubular steel frame with double wishbone, push rod suspension. Usually, the cars are fitted with a 2.0 litre Ford Duratec engine that produces 200 BHP (brake horse power), which is transmitted through the 5 speed sequential gearbox to power the rear wheels (MCR Race Cars, 2018). Aerodynamically, the Sports 2000 cars could be considered to be of modest design, with only a basic splitter design (displayed in *Figure 7*) and an MSA regulated rear wing that permits the addition of a Gurney flap (Morris & Williams, 2018). Additions, in the form of canards (dive planes) are also permitted on the front pontoons and pontoon louvres.

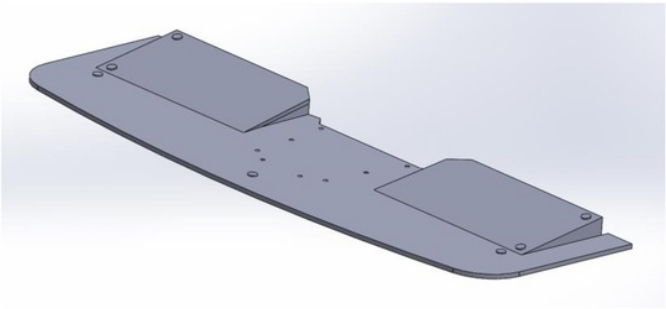


*Figure 7 - MCR Race Cars Splitter Design*

With such a simple chassis design, MCR began to develop the traditional Sports 2000 concept employing a 1.6 litre turbo charged Ford Eco-Boost engine, capable of generating in excess of 300 BHP. This design subsequently became eligible for the BRSCC Open Sports Series (OSS) championship.




*Figure 8 - MCR Race Cars Open Sports Series (OSS) Race Car (MCR Race Cars, Sports Racing Car Manufacturers, 2019)*

*Figure 8* illustrates the current design for the OSS race car. As can be observed, adjustments have been made to the bodywork, with additional air inlets introduced to cool the important working components of the car, including the engine and brakes. A twin element rear wing has been added, together with a basic diffuser (not pictured), comprising a single flat plane at an angle of 7°, with a single kick point. Larger canards have been employed on the front of the vehicle to overcome the lack of frontal grip resulting from the use of the original Sports 2000 splitter design. It has been stated that the car "*suffers with frontal downforce*" due to the increased speeds and larger rear wing, which is needed to provide the required rear traction (Hayes, 2016), therefore creating a rearward aerodynamic balance.

Due to these circumstances (in addition to others that shall be discussed later in this report), it has been decided that the Sports 2000 concept body work (*Figure 3*) will be maintained as the baseline shell for the incorporation of all further aerodynamic developments, with the purpose generating improved downforce (and aerodynamic efficiency) and an enhanced aerodynamic balance.

## 2.2.0 Open Sports Series Championship (OSS)

The OSS championship was originally established to allow any type of sports prototype race car to compete, providing the opportunity to promote advanced engineering developments. This approach resulted in the technical regulations being left moderately open, however, the use of a classification system based on engine displacement is required, as referred to in *Table 1* (BRSCC, 2019).

*Table 1 - OSS Championship Class Categories*

| Class | Minimum Displacement (cc) | Maximum Displacement (cc) | |
|---|---|---|---|
| A | 2001 | N/A | Open Top |
| B | 1501 | 2000 | Open Top |
| C | 1301 | 1500 | Open Top |
| D | 1001 | 1300 | Open Top |
| E | N/A | 1000 | Open Top |
| F | N/A | 2001 | Closed top non motorcycle or rotary engine cars over 2001 cc |
| G | N/A | 2000 | Closed top non motorcycle or rotary engine enclose cars up to 2000 cc |
| I | INVITATION | | |

This categorisation allows the car concerned to be installed in a lower class, however, maximises power due to the forced induction nature of the power train, therefore, has greater potential of winning races within its assigned class.

### 2.2.1 Regulations

Regardless of the relaxed regulations, some minor technical enforcements still exist in order to accord with Motorsport UK (MSUK, formerly Motorsport Association/MSA).

The outlined regulations below are only relative to bodywork modifications and are applicable to the particular series concerned.

OSS organisers state a minimum ride height of 25mm.

Motorsport UK regulations declare:

- Aerodynamic devices must not extend beyond the maximum width of the vehicle and the maximum height of the role over protection system.
- Devices must not extend longitudinally from the rear wheel axis by more than 1100mm.

(Motorsport UK, 2019)

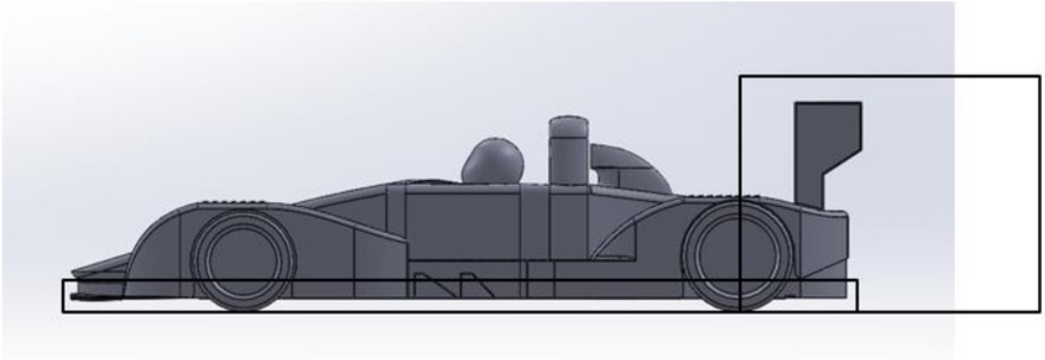


*Figure 9 - OSS/MSUK Regulation Reference Boxes*

*Figure 9* indicates a visual representation of the areas of concern. The concept illustrated in the above figure was designed for a static ride height of 40mm (in accordance with the SRCC Sports 2000 regulations), however it can now be lowered to a minimum of 25mm. Multiple wing profiles are now permitted and maximum distances from wheel centre lines are extended.

## 2.3.0 Wing Theory

Ultimately, wings produce the majority of downforce generated by a race vehicle. Employing this approach increases lateral acceleration and improves braking capabilities. However, it can have a detrimental effect on overall car performance, resulting from the induced drag that a wing will ultimately produce (Soso & Selig, 2002).

In terms of wing geometry, an aerofoil is considered to be a 2D cross-sectional area of the wing. The 2D profile being the actual design model where the intended purpose of the wing can be modified or adjusted with regard to its intended use (Katz, 1995).

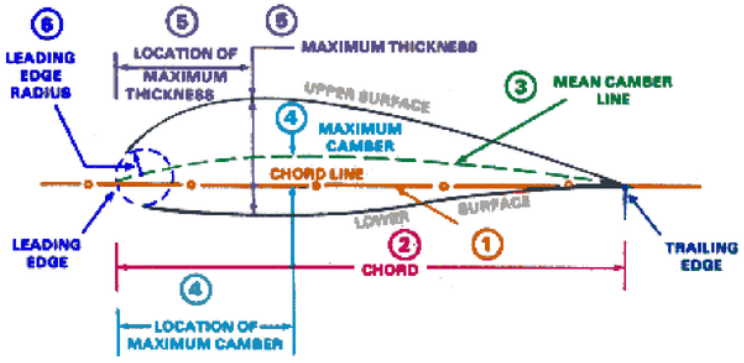



*Figure 10 - Aerofoil Diagram (Birchall, 2011)*

As the above diagram (*Figure 10*) indicates that alterations can be made through the 2D profile, with each change affecting how the wing will distribute the generated pressures along its planar surfaces when constructed as a 3D model.

The basic principle behind the working theory of the generation of lift by a wing (as per its conventional use), is the creation of a pressure differential between its upper and lower surfaces of the wing. According to Bernoulli's theorem, the relationship between pressure and velocity is that a greater air velocity will generate a lower pressure and vice versa (*Equation 4*).

$$P_1 + \frac{1}{2}\rho V_1^2 + \rho g h_1 = P_2 + \frac{1}{2}\rho V_2^2 + \rho g h_2$$

*Equation 4 - Bernoulli's Theorem*

A venturi tunnel can be used to demonstrate the basic application of this theorem. Where the throat of the tunnel begins to reduce, the fluid velocity must increase to sustain a continuity of mass if the system is to remain in equilibrium, therefore the pressure in the area of throat reduction must also reduce.

Three main theories of lift generation exist; however it can be said that a definitive answer as to the reason for lift generation is still questionable.

Theories describing the creation of wing pressure differentials include:

- Equal Transit (air molecules travel further on one side, therefore have to have a greater velocity).
- Skipping Stone (every action has an equal and opposite reaction (Newton, 1687)).
- Venturi Theory (where the free stream air acts as a wall and creates a throat section against the wing surface).

(Hall, 2018)

However, there is a fourth theory.

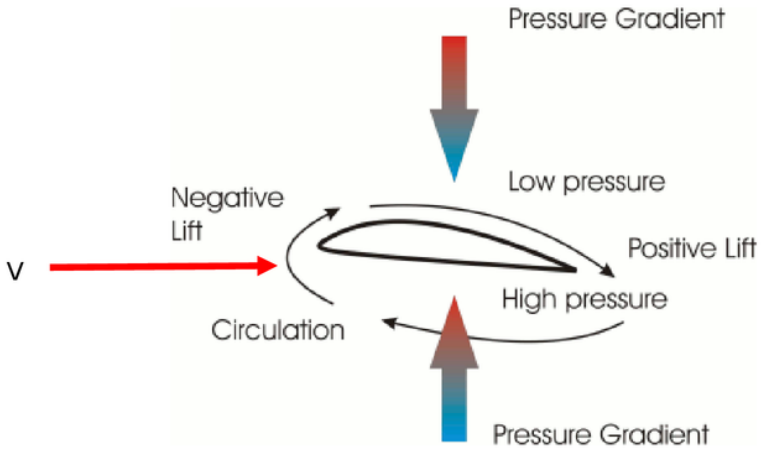



*Figure 11 - Wing Recirculation (Glownia, 2007)*

This explanation involves the phenomenon of positive pressure gradients (where high pressure travels to low pressure), causing a recirculation of air around the profile, as illustrated in *Figure 11.* As with a lift generating configuration, the air on the lower surface resists the oncoming free stream flow, thus slowing the air velocity, creating a higher pressure, whereas the air on the upper surface travels in the same vector as the free stream, hence an increase in velocity is expected. This produces the required pressure differentials, the outcome being lift. Within a race car application, the wing is simply inverted, which therefore generates downforce (Glownia, 2007).

2.3.1 Boundary Layer

Viscosity is a fundamental property of all fluids, including that of air. A boundary layer occurs due to fluid viscosity, causing a layer of 0 m/s air to be generated upon the surface of an object which the fluid flows around. Shear forces which are present when the two matters meet, halts the velocity flow that is directly parallel to the surface plane.

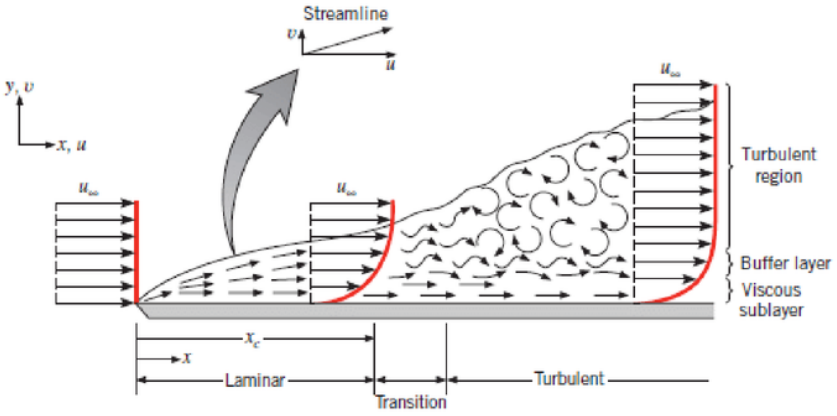



*Figure 12 - Boundary Layer (Banihani, 2018)*

*Figure 12* illustrates the formation of a boundary layer. It can be observed that as the layer is developed along the planar surface, its depth in the Y axis increases (McBeath, 1998). As the vertical distance away from the surface grows, the velocity of the fluid also rises as the free stream flow is entered.

Boundary layers can be estimated as laminar or turbulent by calculating their equivalent Reynolds Number which is considered a dimensionless factor given as a ratio scalar figure.

$$Re = \frac{\rho V l}{\mu}$$

*Equation 5 - Reynolds Number*

It is stated that:

- Laminar = $<1x10^5$
- Turbulent = $>5x10^5$

However, these values differ for internal fluid flow.

The boundary layer can be broken into six sub-sections. Horizontally, the flow begins as laminar (clean), where no turbulence exists due to the high energy nature of the fluid. As energy losses begin, the fluid then evolves into a transition state. As further energy is lost, air molecules begin to break away from the laminar trajectory of the initial flow, later

developing into a fully turbulent movement. The turbulent area exists when sufficient energy is depleted that the fluid can no longer remain attached to its original trajectory on the surface plane (McBeath, 1998).

The vertical formation of the boundary layer is also broken into three sections. The viscous sublayer is the innermost layer within the boundary. This region experiences the highest pressure gradient, thus the highest shear stress against the wall which it flows against, generating frictional forces (Bradshaw & Huang, 1995). The layer above is classified as a Buffer layer, where the fluid velocity breaks away from the overall linearity that is seen in the viscous sublayer and begins to become turbulent in nature. The Turbulent region is the outer part of the boundary layer, where the flow is fully turbulent as an outcome of the energy lost resulting from the development of friction (wall shear stresses) (Hellio & Yebra, 2009).

### 2.3.2 Separation

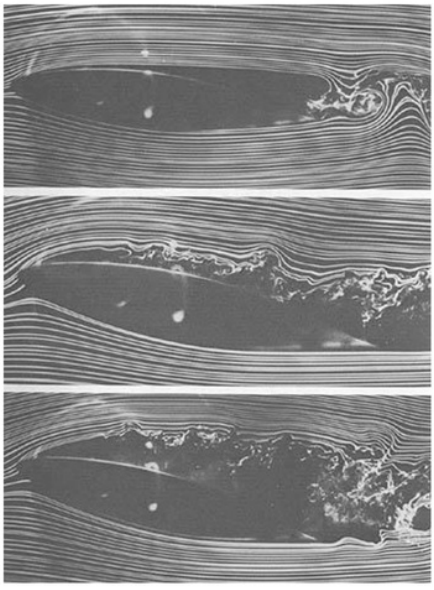


*Figure 13 - Flow Separation (history.nasa.gov, 2010)*

Separation is a flow condition governed by the depletion of energy in the boundary layer which is lost as heat. This is as a direct result of the frictional build up in the shear wall region, further resulting in the boundary lifting from the planar surface. The outcome of this is an extreme turbulence situation (*Figure 13*). Strong adverse pressure gradients also produce a flow separation condition as the energy contained within the boundary layer is insufficient to overcome that of the adverse pressure differential. It should be noted that this situation does not adhere to Bernoulli's Theorem, therefore the system struggles to remain in

equilibrium. Once the boundary layer begins to separate, the void that is left between the air and object surface has a resultant low pressure (Balmer, 2003).

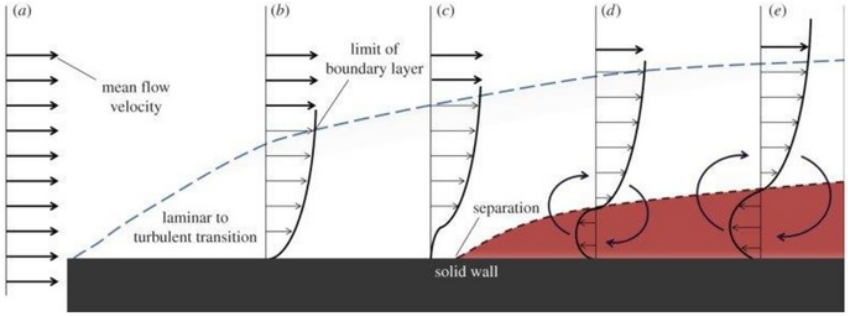



*Figure 14 - Eddie Formulation (Fletcher, et al., 2014)*

As can be observed in *Figure 14*, the vacuum that is produced in the low pressure region results in a swirling motion within the fluid flow, with an outcome of formulating eddies, which grow in size as energy is then absorbed from the oncoming free stream flow.

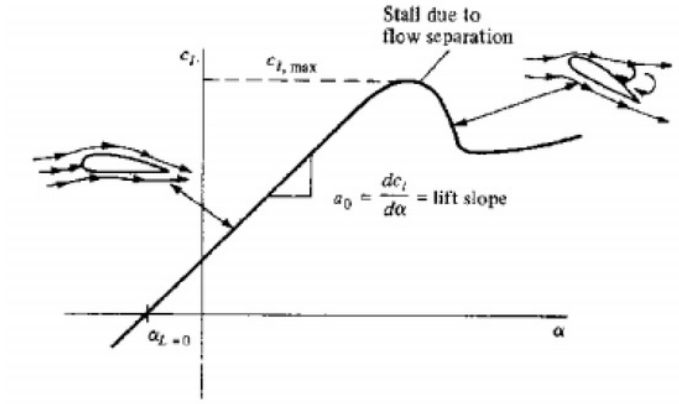



*Figure 15 - Cl vs AoA (Seljak, 2008)*

A state of flow separation often results in an increase in drag, and a decrease in lift (*Figure* 15) due to the increased pressure differential (known as pressure drag) from leading edge to trailing edge of the object concerned (Fielding, 2005).

2.3.3 Multi – element Wings

One of the most effective ways of generating an increase in downforce is through the use of a multi-element wing. This concept involves the use of a main plane (main element) which is then complimented by a secondary element, that is maintained at a set longitudinal distance, height and angle away from the main plane.

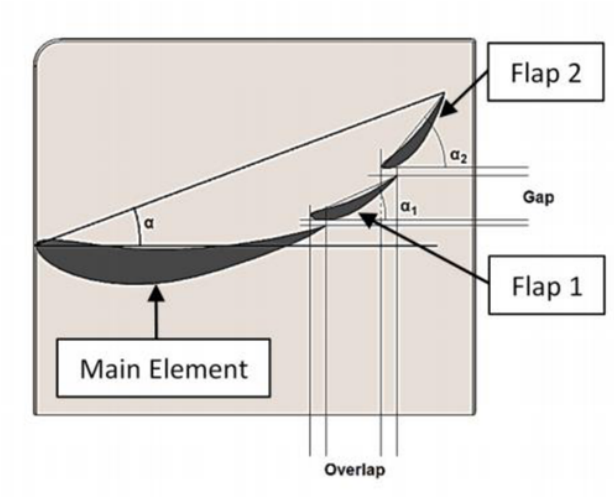



*Figure 16 - Multi - Element Aerofoil (Jackson, 2018)*

As illustrated in *Figure 16,* multiple elements can be used and the overall geometry can vary in complexity, as is the case with Formula One front wings.

$$Aspect\ Ratio = \frac{Span}{Chord}$$

*Equation 6 - Aspect Ratio*

As demonstrated in *Equation 2 (Lift Force)*, for any given increase in downforce, the planar area of the wing can be increased. McBeath states that low aspect ratio wings create a reduction in aerodynamic efficiency, and goes on to say, "*they can help by delaying stall to a steeper angle than on a high aspect ratio version*" (McBeath, 1998). So, to generate greater downforce, and maintain efficiency, the employment of multiple elements should seriously be considered.

Under careful analysis, an increase in Cl can be accomplished with only a small increase in planar area, therefore efficiency is maintained.

With consideration to the placing of the secondary element, a venturi is created between the trailing edge of the main plane and the leading edge of the secondary element, with a narrowing from its opening to its exit (McBeath, 1998). It is thought that air from the high

pressure side of the main plane is bled through onto the low pressure side of the secondary element, with an increase in velocity as a result of the venturi slot gap. This then re-energises a potentially depleted boundary layer, therefore enabling and maintaining flow attachment at greater angles of attack, thus the production of greater downforce can be achieved (Kachare, 2017).

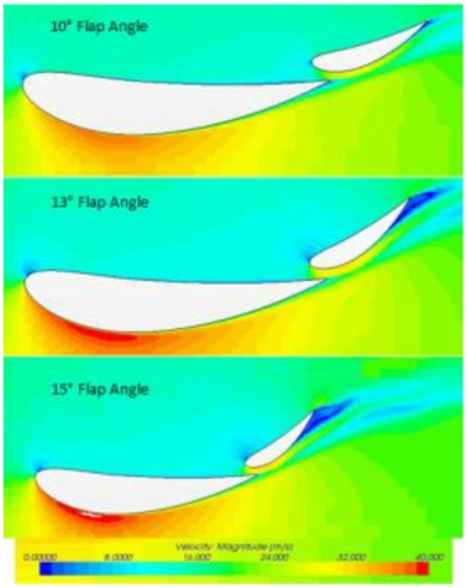



*Figure 17 - Multi - Element Wing Element Configurations (Craig & Passmore, 2014)*

*Figure 17* illustrates the effects of secondary element AoA on the main plane. It can be observed that as the secondary element is given a greater angle, the velocity profile on the underside of the main plane is increased, thus producing an increase in downforce as the pressure differential from upper and lower surfaces becomes greater. This occurs due to the greater expansion volume that now has to be filled to maintain the system in equilibrium.

However, it can also be noted that with a large AoA, flow separation is likely to occur, therefore the optimum configuration is passed. These characteristics are somewhat generalised, as changes in wing profile geometry can dramatically affect the working aerodynamic characteristics of the entire configuration (Craig & Passmore, 2014).

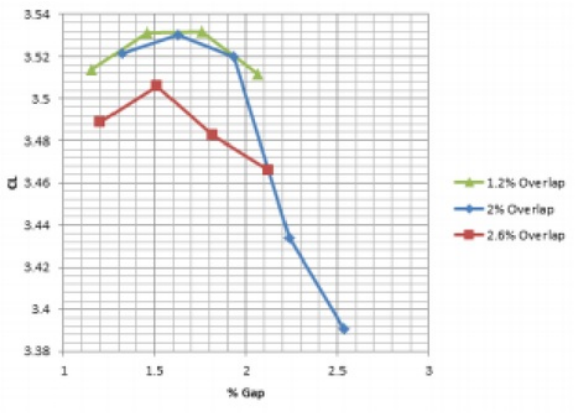



*Figure 18 - Gap Size & Overlap Sensitivity Study (Craig & Passmore, 2014)*

*Figure 18* illustrates how changing the slot gap and overlap can affect the Cl produced from a multi – element wing. These results refer to the aerofoils illustrated in *Figure 17*. *Figure 18* indicates that the optimum overlap of 1.2% c (chord length) in the $x$ direction and a slot gap of 1.6% c (green line) produces the greatest Cl over a wider working range.

This therefore, illustrates how changing these criteria can affect how the wing produces downforce.

### 2.3.4 Ground Effect

The front wing on a Formula One race car produces 25% - 35% of the total generated downforce due to its close proximity to the ground (Zhang, et al., 2006).

It has been observed that when an aerofoil is in close proximity to the ground, the velocity profile around it is modified to generate a much more intense lift component, however, if the wing is positioned too close to the ground, it will then begin to lose its generated lift (Abdullah, et al., 2017).

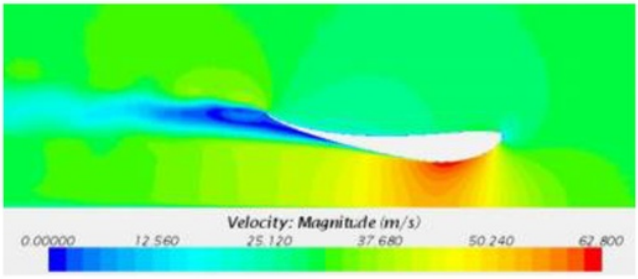



*Figure 19 - Aerofoil in Ground Effect (S1223) (Mokhtar & Durrer, 2016)*

As previously stated, it is widely recognised that as a wing comes into close proximity to the ground, its lift values begin to dramatically improve, however, studies by (Mokhtar & Durrer,

2016) show that a wing's distance to the ground can be too close. It was discovered that the boundary layers from both the wing and ground begin to merge as one, causing a blockage effect on the underside of the wing, thereby reducing the velocity and increasing the pressure.

It is therefore understood that great consideration needs to be given to the distance by which the front wing should be located above the ground. *Figure 19* illustrates an S1223 profile (designed by Michael Selig), in close proximity to the ground.

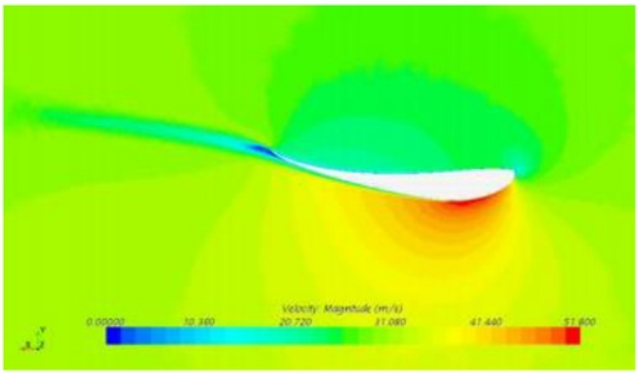



*Figure 20 - Aerofoil in Freestream (S1223) (Mokhtar & Durrer, 2016)*

The above figure (*Figure 20*) illustrates the same profile from the same study of ground effect, but in Freestream. Both studies used a mean air flow velocity of 30m/s. The most striking difference is the wake formations produced, with the ground effected wing having a much greater, non-uniform wake compared to that of the wing in *Figure 20*. It is also noted that the wing illustrated in *Figure 20* has a larger spread of high velocity air on the underside, but its peak velocity is lower than that produced by the ground effected wing. Its peak downforce being lower, however, may make the ground effected wing much less stable due to the small area in which its peak low pressure exists (Mokhtar & Durrer, 2016).

In accordance with Bernoulli's Theorem, it is understood that a reduction in the throat region would generate a higher air velocity, thus lower pressure. This is also enhanced by highly cambered wings such as with the S1223 profile, which create a much larger expansion region which the expelled air has to fill.

## 2.4.0 Aerodynamic Balance

The balance of a race vehicle is an important aspect when making considerations regarding aerodynamic development. Each race track has its own requirements in terms of aerodynamic performance, therefore a predictable aerodynamic package could be thought of as being essential.

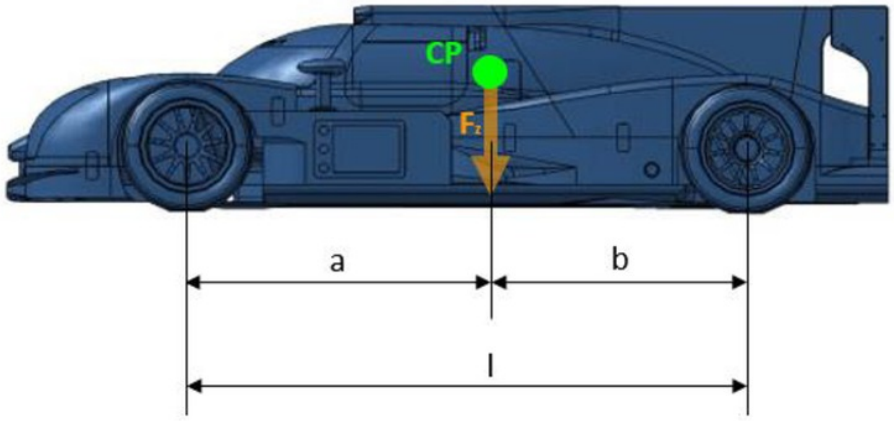



*Figure 21 - Downforce Distribution (CP) (Quintarelli, 2018)*

In terms of the concerned study, if the front wing were to generate too much downforce, this would mean that the total distribution of downforce moves forward, and therefore make the car less predictable in a dynamic environment. It therefore follows that serious consideration needs to be given to the positioning of the Cp.

As *Figure 21* indicates, the positioning of the Cp will change the distribution of force across both front and rear axles, as a turning moment is taken from the Cp distance to the CoG.

$$Cp\ Balance\ \% = \frac{F_{front}}{F_{total}} * 100$$

*Equation 7 - CP Balance %*

The above equation (*Equation* 7) is used to calculate Cp in terms of percentage with the respect to the front axle downforce.

If the Cp were to sit behind the CoG, this could cause the rear of the car to sit lower than the front, as velocity increases and vice versa depending on the location of Cp to CoG. As the car concerned has a rearward CoG due to the engine location, it is advisable to have the Cp forward of this position (Quintarelli, 2018).

The overall dynamic behaviour of the car needs to be considered, for example, performing a braking manoeuvre will cause the car to pitch forward (the front will sit lower than the rear)

as longitudinal load is transferred from the rear to the front. This will then promote the front wing/splitter to become further engulfed in a ground effect situation or even come into contact with the ground, resulting in potential damage and, or, handling issues (Katz, 1995).

### 2.5.0 Computational Fluid Dynamics (CFD)

CFD is the computational method used to predict and characterise fluid flow. In the case of this study, around wings and a car (bluff body).

Three main criteria need to be considered throughout the CFD process in order to be able to obtain suitable results.

#### 2.5.1 Domain (Pre – processing)

The fluid domain is a computational representation of the working area. In this instance, it is considered to be the virtual working area of a wind tunnel. Lengths in the $x, y$ and $z$ directions are often referred to as the lengths of the object of interest. It has been suggested that using three car lengths in front, five car lengths behind and the displacement of the object should not be greater than 1% to 1.5% of the total domain volume (Lanfrit, 2005). However, these dimensions vary from analyst to analyst, as it is further suggested that using two lengths in front and that the entire length of the domain should not exceed eight lengths in total (Christopher, 2015).

To reduce the potential computational expense, the introduction of a symmetry plane can be beneficial, though this technique can only be used for geometries of a symmetrical nature, however a symmetry plane can cause stability issues in flow residuals when used with RANS (Reynolds Averaged Navier Stokes) equations (Toet, 2019).

#### 2.5.2 Mesh (Pre – processing)

A mesh is a structured or unstructured build grid of 2D or 3D shapes (commonly tetrahedra's are used in CFD) to capture and represent the geometry within the fluid domain (Hughes, 2018), including fluid volume and object surfaces (*Figure 22*).

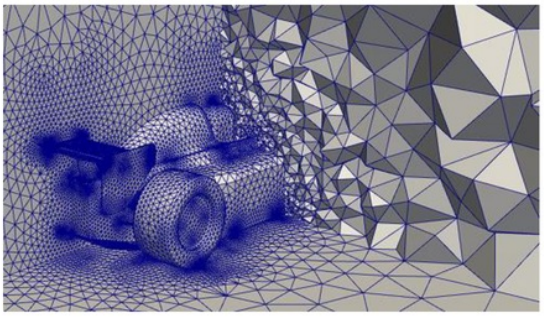


*Figure 22 - Surface & Volume Mesh (Using a Symmetry Plane) (symscape, 2013)*

It is essential that a mesh of a suitable density is used to accurately capture the geometry detail and thus complex flow forms can be obtained. However, the risk of using a mesh with a structure that is too dense may have a negative impact upon the computational time required. Therefore, only critical flow areas need mesh refinements to be considered (Ahmad, et al., 2010).

2.5.3 Solving (Processing)

Before any post processing can begin, the employment of turbulent solving needs to occur. The system is based on the use of the Navier Stokes Equations for Newtonian fluids.

$$Continuity: \frac{d\rho}{dt} + \frac{d(\rho u)}{dx} + \frac{d(\rho v)}{dy} + \frac{d(\rho w)}{dz} = 0$$

$$X - Momentum: \frac{d(\rho u)}{dt} + \frac{d(\rho u^2)}{dx} + \frac{d(\rho uv)}{dy} + \frac{d(\rho uw)}{dz} = -\frac{dp}{dx} + \frac{1}{Re_r}\left(\frac{d\tau_{xx}}{dx} + \frac{d\tau_{xy}}{dy} + \frac{d\tau_{xz}}{dz}\right)$$

$$Y - Momentum: \frac{d(\rho v)}{dt} + \frac{d(\rho uv)}{dx} + \frac{d(\rho v^2)}{dy} + \frac{d(\rho vw)}{dz} = -\frac{dp}{dy} + \frac{1}{Re_r}\left(\frac{d\tau_{xy}}{dx} + \frac{d\tau_{yy}}{dy} + \frac{d\tau_{yz}}{dz}\right)$$

$$Z - Momentum: \underbrace{\frac{d(\rho w)}{dt}}_{\text{Local Acceleration}} + \underbrace{\frac{d(\rho uw)}{dx} + \frac{d(\rho vw)}{dy} + \frac{d(\rho w^2)}{dz}}_{\text{Convection}} = \underbrace{-\frac{dp}{dz}}_{\text{Pressure Gradient}} + \underbrace{\frac{1}{Re_r}\left(\frac{d\tau_{xz}}{dx} + \frac{d\tau_{yz}}{dy} + \frac{d\tau_{zz}}{dz}\right)}_{\text{Viscous Terms}}$$

$$\begin{aligned} Energy: &\frac{d(E_t)}{dt} + \frac{d(uE_t)}{dx} + \frac{d(vE_t)}{dz} \\ &= -\frac{d(up)}{dx} - \frac{d(vp)}{dy} - \frac{d(wp)}{dz} - \frac{1}{Re_r Pr_r}\left(\frac{dq_x}{dx} + \frac{dq_y}{dy} + \frac{dq_z}{dz}\right) \\ &+ \frac{1}{Re_r}\left(\frac{d}{dx}\left(u\tau_{xx} + v\tau_{xy} + w\tau_{xz}\right) + \frac{d}{dy}\left(u\tau_{xy} + v\tau_{yy} + w\tau_{yz}\right)\right. \\ &\left. + \frac{d}{dz}\left(u\tau_{xz} + v\tau_{yz} + w\tau_{zz}\right)\right) \end{aligned}$$

*Equation 8 - Navier Stokes*

Using a Cartesian co-ordinate system, the above equation *(Equation 8),* calculates the conservation of momentum in the $x, y$ and $z$ directions, the conservation (continuity) of mass and conservation of energy using coupled partial differential equations which are all time dependent (Hall, 2015).

These equations are used to predict fluid velocity through its mass flow, this being the pressure around a given object (*Figure 23*). Therefore, using Newtons second law, the forces produced can be quantified (uk.comsol.com, 2017).

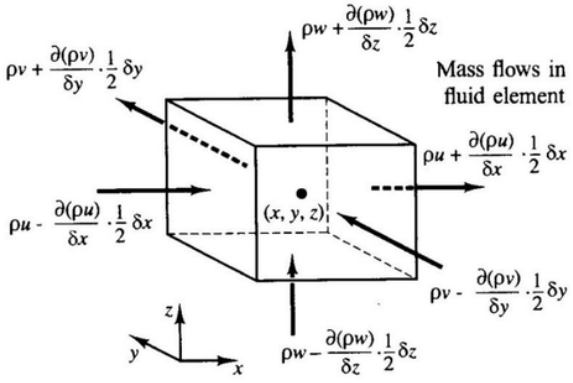



*Figure 23 - Mass Flows per Mesh Element (Sergio, 2017)*

With respect to the above Navier Stokes equations, most external fluid flow issues encounter high inertial forces and varying gradients of velocity with applied high viscous forces, therefore a RANS variation of the Navier Stokes equations is applied.

The purpose of the RANS model is to average the flow velocity and pressure per unit time. This, therefore, means that less computational time is required to solve the external flow regime (Sodja, 2007).

There are many forms of the RANS turbulence model, with constant developments being made. For the purpose of external bluff body flow simulation, the two most common models are the $k\varepsilon$ (K – Epsilon) and $k\omega$ (K – Omega), of which there are several subscripts, all of which are preferable for differing boundary conditions (Versteeg & Malalasekera, 1995). The $k\varepsilon$ model is the model favoured for far from wall conditions, with the $k\omega$ model being preferred for close to wall conditions.

It has been asserted that the $k\varepsilon$, Realizable, Non – equilibrium Wall Functions turbulence model is superior when predicting fluid flow around a car (Lanfrit, 2005). The term "*Realizable*" evaluates the Reynolds shear stresses and applies them, and the "*Non-Equilibrium Wall Functions*" model predicts areas of large pressure gradients and provides greater accuracy within the modelling process compared to that of the standard model (Frei, 2017). The standard model struggles to simulate the close to wall region (viscous and buffer layer), therefore incorrect prediction of separation and large pressure gradients are often inaccurate.

## 3.0.0 CFD Methodology Validation

CFD is a computational method that uses mathematical equations to predict fluid flow, therefore must follow strict laws, however, fluids can be unpredictable with many variables that may be ignored or neglected if improper use of the CFD software were to occur. Therefore, to gain confidence within the results that the CFD application is producing, four validation studies took place.

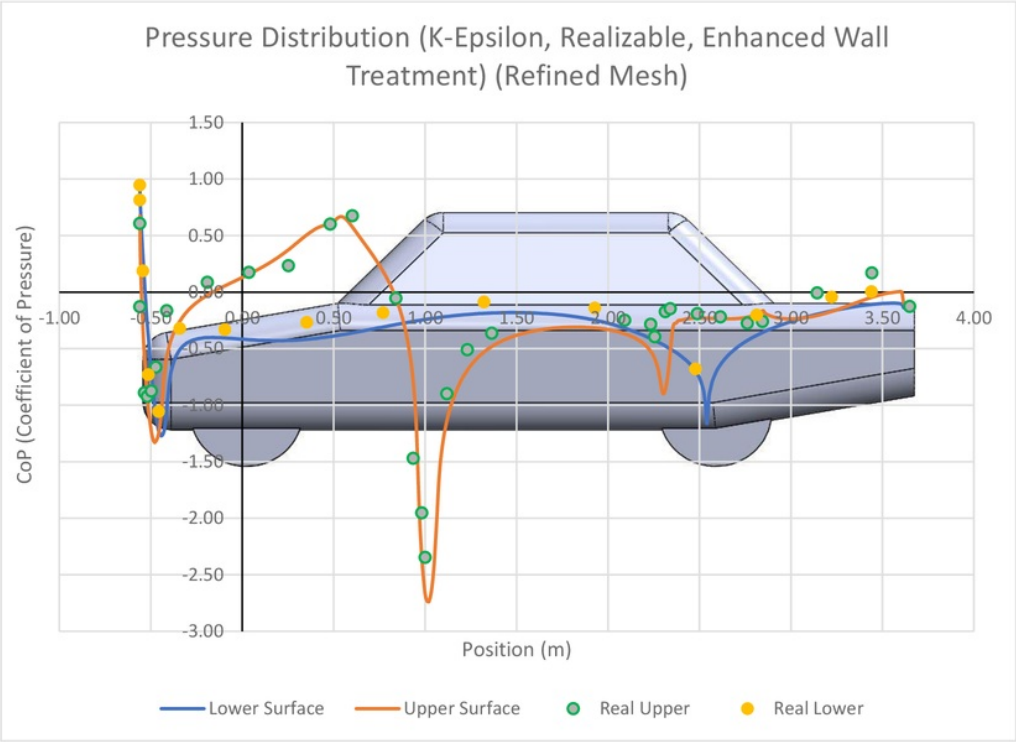
- Bluff Body CFD representation to wind tunnel data.
- Wing Profile CFD representation to wind tunnel data.
- Wing Profile Flow Vis representation to CFD data.
- Baseline MCR Sports 2000 CFD comparison to TotalSim CFD data.

The four methods involve a bluff body and a wing profile, both of which are the focus of this report and its subsequent studies.

### 3.1.0 MIRA Car Validation Study

This section contains a condensed account of the previously written report "*External Computational Fluid Dynamics Simulation Validation Experiment – MIRA Wind Tunnel*" (Hughes, 2018).

The MIRA car is a popular validity tool used worldwide, where engineers calibrate CFD settings to correlate with wind tunnel data produced at HORIBA MIRA. In this instance, Cl and Cd were both matched along with a close representation of the surface pressure distribution.




*Graph 1 - MIRA Car Pressure Distribution (CFD Validation) (Hughes, 2018)*

The above graph (*Graph 1*) indicates the pressure distribution in terms of CoP (*Equation 9*), of the upper and lower surfaces of both the virtual Mira car and the real Mira car. In order to achieve Cl and Cd results with a 6% difference to the wind tunnel data, domain size, mesh density and turbulence model were all investigated.

$$CoP = \frac{P - P_s}{\left(\frac{1}{2}\right)\rho V^2}$$

*Equation 9 - Coefficient of Pressure (CoP)*

*Table 2 - Maximum & Minimum CoP Comparison*

| | Lower CFD | Real Lower | Upper CFD | Real Upper |
|---|---|---|---|---|
| Max | 0.95 | 0.95 | 0.67 | 0.67 |
| Min | -1.27 | -1.06 | -2.74 | -2.35 |

*Table 2* indicates the maximum and minimum CoP figures for the CFD model and the wind tunnel model. It can be observed that some differences are apparent, however, it was discussed that the CFD model is able to apply an almost infinite amount of pressure taps along the longitudinal surface of the car, whereas the wind tunnel model has a total of 46 pressure taps along its longitudinal surface. Therefore, the CFD model is able to produce greater detail, although, it's overall accuracy is still unknown.

### 3.2.0 Naca 0012 Wind – Tunnel Validation Study

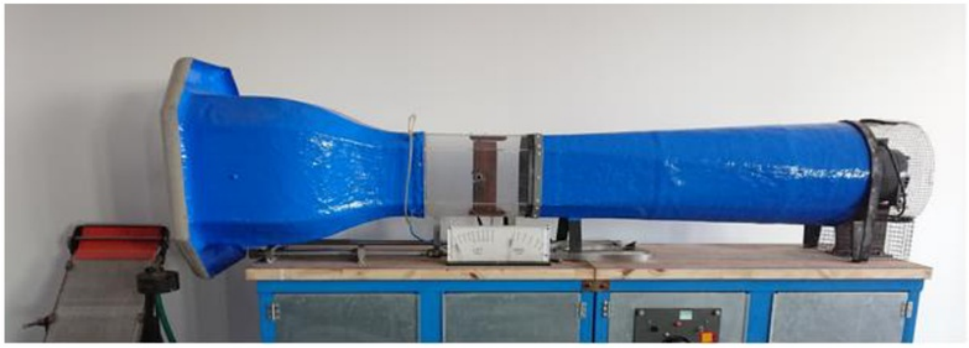


*Figure 24 - C2 Open Loop Wind Tunnel*

*Figure 24* illustrates a **1/12** scale open loop wind tunnel with a pressure tapped Naca 0012 (symmetrical) aerofoil within the working section. The aerofoil has the ability to be rotated about its $y$ axis, therefore pressure data could be taken for differing AoA.

Surface pressure data was taken for 0°, 5°, 10° and 15° AoA, with a velocity of 6.75m/s.

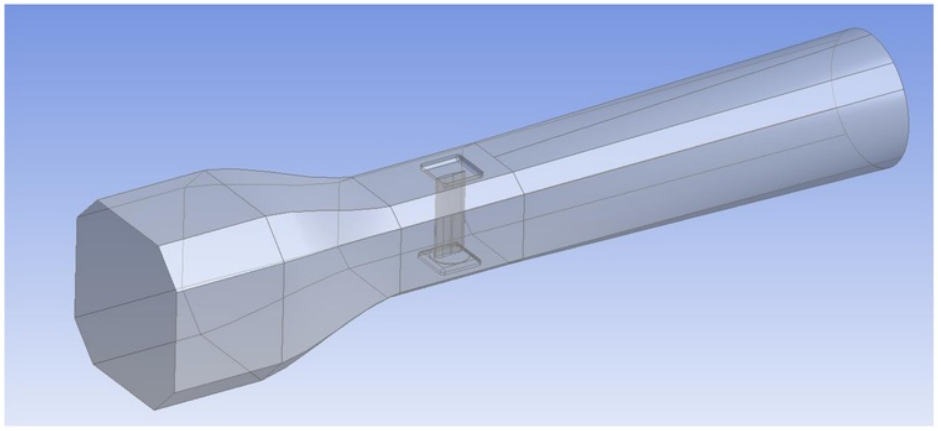
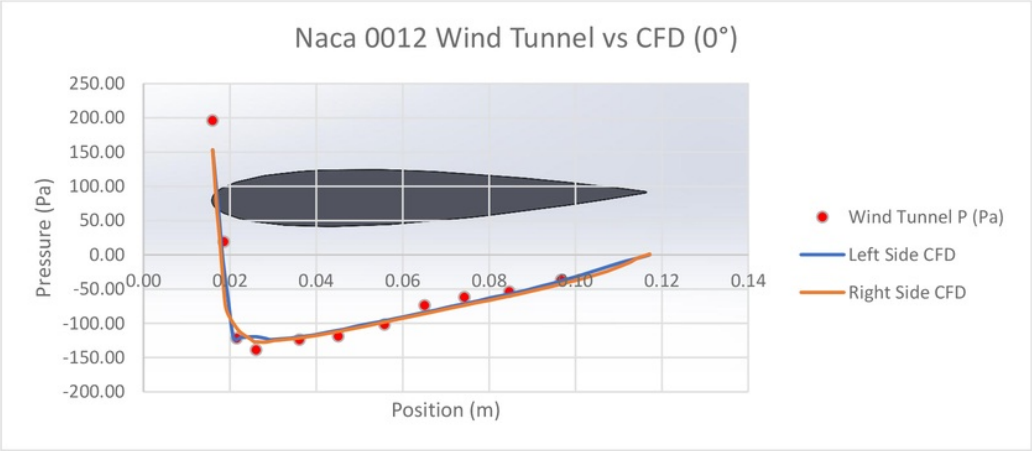


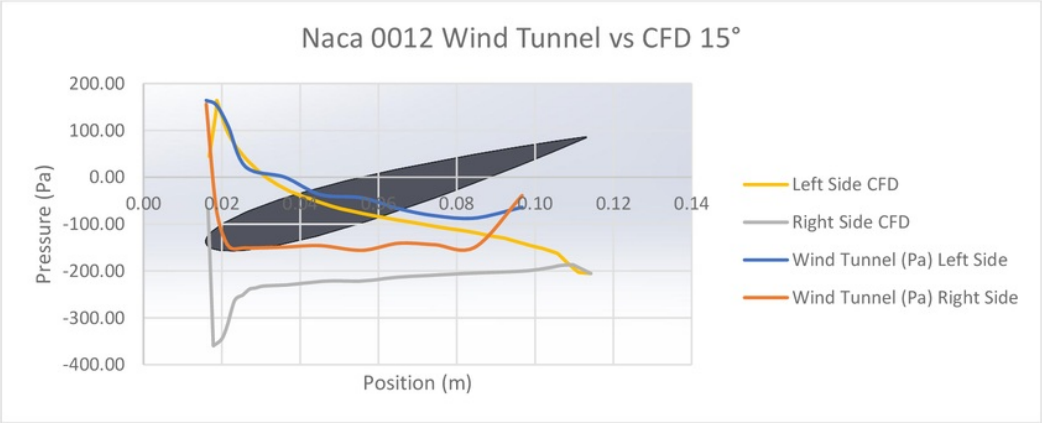
*Figure 25 - C2 Open Loop Virtual Wind Tunnel*

*Figure 25* illustrates a virtual model of the C2 wind tunnel with a Naca 0012 profile within the working section. The model was created by accurately measuring the wind tunnel dimensions and the aerofoil dimensions, allowing like for like comparisons can be made between the collected physical and virtual data.




*Graph 2 - Naca 0012 Wind Tunnel vs CFD (0°)*

*Graph 2* illustrates overlaid data from the physical test and the data produced by the CFD model. The CFD model was simulated using a $k\varepsilon$, Realizable, Non – Equilibrium Wall Functions RANS turbulence model. It can be observed that both sets of surface pressure data match when compared. The symmetrical nature of the aerofoil allows both sides to possess the same pressure distributions when at 0° AoA. It is also noted that no separation is occurring due to the gradual return to atmospheric pressure as the data indicates.




*Graph 3 - Naca 0012 Wind Tunnel vs CFD (15°)*

The above graph (*Graph 3*) illustrates the same aerofoil, as in *Graph 2,* but at 15° AoA. When initially conducted, the $k\varepsilon$ model inaccurately captured the surface pressures, predicting no separation, whereas the physical data clearly indicates a large pressure gradient, where separation was apparent. Therefore, a decision was made to change to a $k\omega$ model, due to its superiority when simulating strong pressure gradients. *Graph 3*

indicates the results using a $k\omega$ model. It is still noticeable that visual differences are apparent within the data, however, data trends are followed.

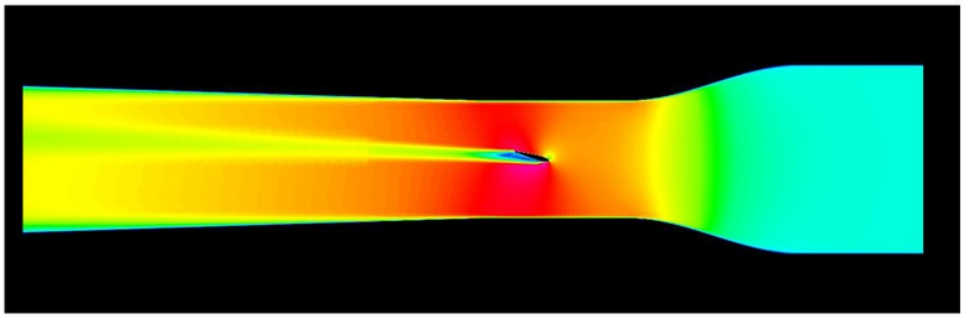


*Figure 26 - C2 Wind Tunnel CFD Velocity Contours (15°)*

*Figure 26* clearly illustrates the predicted separation that has been numerically captured in *Graph 3*. It was also observed visually in the physical wind tunnel using a length of wool. The use of the wool indicated an area of air recirculation in the region of separation (*Figure 27*).




*Figure 27 - Naca 0012 15° Recirculation*

The above flow characteristics that can be observed in *Figure* 27, were then compared to velocity streamlines produced in the CFD data displayed in *Figure 28*.

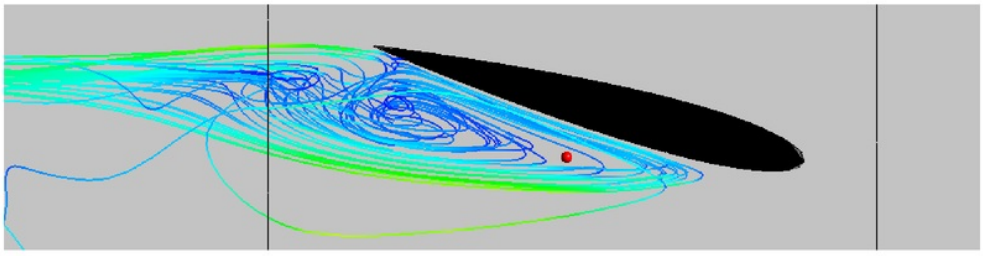


*Figure 28 - Velocity Streamlines Showing Recirculation Naca 0012 (15°)*

This therefore, suggests that flow characteristics are being modelled accordingly, however, variances exist within the numerical figures produced, though trends are followed.

### 3.3.0 Wing Profile Flow Visualisation Validation Study

A further conducted test involved the use of flow visualisation paint. Green powder paint was mixed in a ratio of 2 to 1 with isopropanol alcohol, which was replaced by paraffin in later tests.

A section of MSUK homologated rear wing was secured to a jig in front of a fan. The flow visualisation paint was then applied to both the upper and lower surfaces of the wings, and then the fan was engaged. This crude test revealed some interesting results.



*Figure 29 - Wing Lower Surface Flow Visualisation Paint Test*

*Figure 29* indicates an area of recirculation (circled red) adjacent to the end plate.

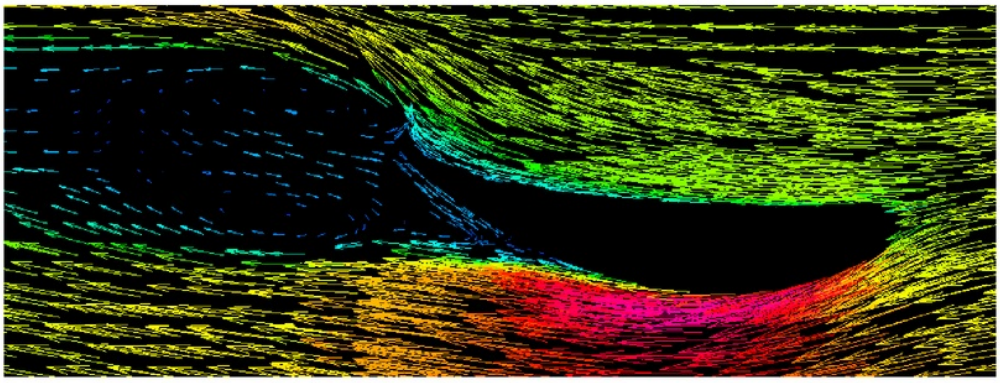


*Figure 30 - Wing Lower Surface Recirculation*

*Figure 30* illustrates the recirculation indicated in *Figure 29*, however, on a vertical plane using velocity vectors. Both physical and virtual tests were conducted using an average velocity of 18m/s. The reason for this was that the fan used, produced varying pulses in air

velocity due to its construction. The above CFD simulation *(Figure 30)* used the previously stated $k\varepsilon$ turbulence model.

Further to this, flow visualisation tests were conducted on the rear wing of an MCR Sports 2000 car during a circuit test at Castle Combe Race Circuit.

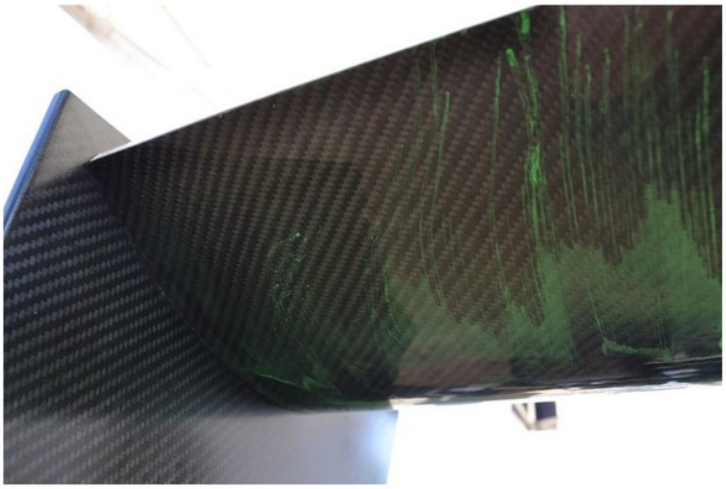


*Figure 31 - MCR Sports 2000 Rear Wing Circuit Flow Visualisation Test*

The rear wing was set to an angle of 5.1° (minimum AoA). As can be observed from *Figure 31*, clear beginnings of separation occur towards the trailing edge of the profile, with a distinct line in the flow visualisation paint.

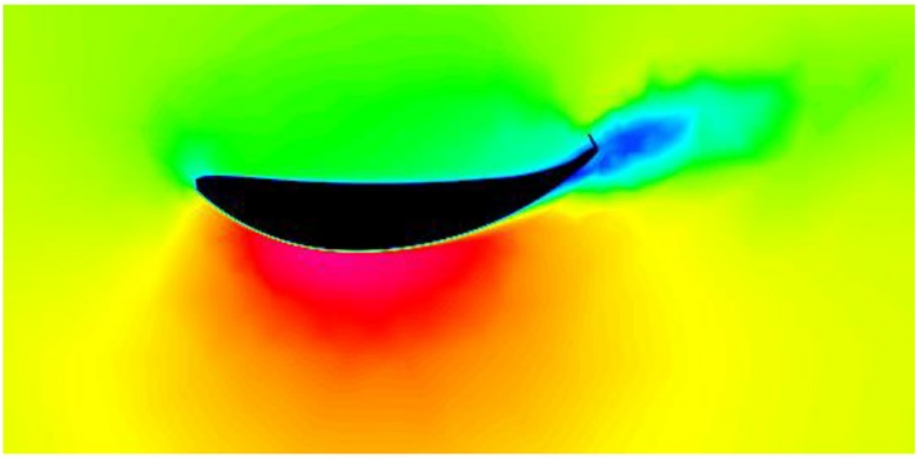


*Figure 32 - MCR Sports 2000 Rear Wing Velocity Contours (5.1°)*

The same characteristics of separation are also apparent in *Figure 32,* towards the trailing edge of the wing. As previous, the recommended $k\varepsilon$ turbulence model was used (Lanfrit, 2005), with an average air flow velocity of 35m/s.

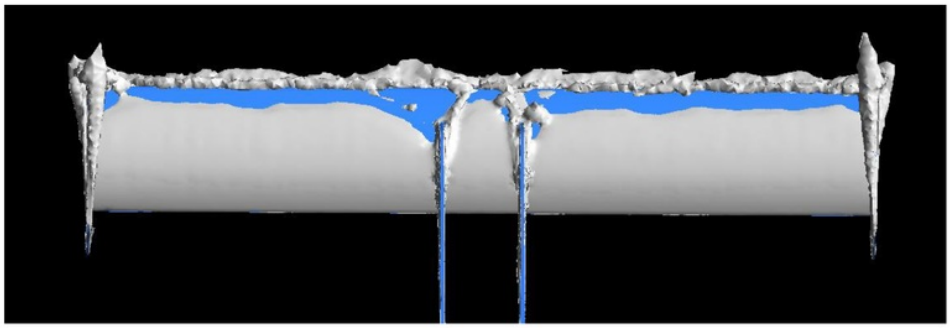


*Figure 33 - MCR Sports 2000 Rear Wing Mount Interaction*

Similarities between the interaction of the wing mount and the lower surface of the wing can also be observed. *Figures 33 & 34,* indicate similar results between flow form in the physical test and the virtual test, with the flow being pushed outboard from the wing mount, producing further disruption to the flow on the main plane of the rear wing.



*Figure 34 - MCR Sports 2000 Rear Wing Mount Interaction Flow Visualisation*

## 3.4.0 Baseline MCR Sports2000 CFD Comparison

*Table 3 - MCR Sports2000 Baseline CFD vs TotalSim MCR Sports2000 Baseline CFD*

| | Drag (N) | Downforce (N) | Downforce (Kg) | Efficiency | Cd | Cl |
|---|---|---|---|---|---|---|
| Baseline MCR | 500 | 382 | 39 | 0.76 | 0.506 | -0.386 |
| TotalSim MCR | 455 | 348 | 35 | 0.76 | 0.46 | -0.352 |
| | | | | Difference (%) | 9.9 | 9.7 |

While distinct comparisons between physical and virtual tests could be made, it was thought advisable to undertake a comparison of virtual testing with the known simulation company, TotalSim.

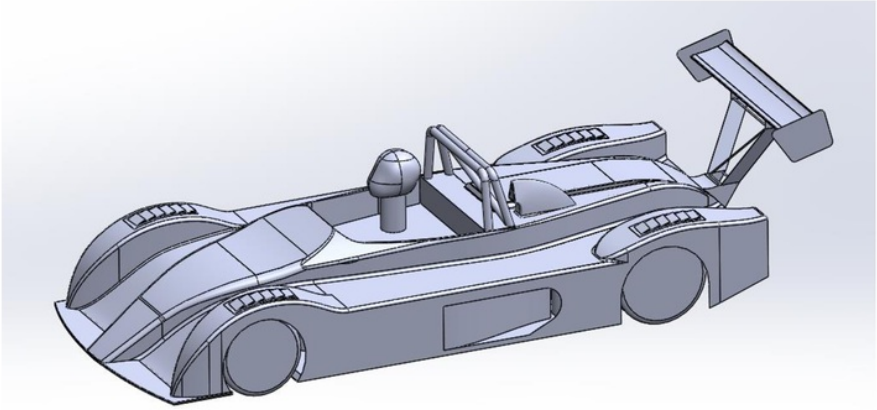


*Figure 35 - MCR Sports 2000 Baseline Geometry*

*Table 3* indicates the results taken from CFD simulations produced using a baseline MCR Sports 2000 geometry (*Figure 35*). A difference in Cd and Cl results is apparent, however, they fall within a 10% margin, therefore the CFD parameters used could now be deemed viable (Brooks, et al., 2003).

## 4.0.0 Initial Geometries

With confidence in the CFD input variables, initial testing of geometry designs could be conducted.

### 4.1.0 Baseline Geometry (JHTT02)

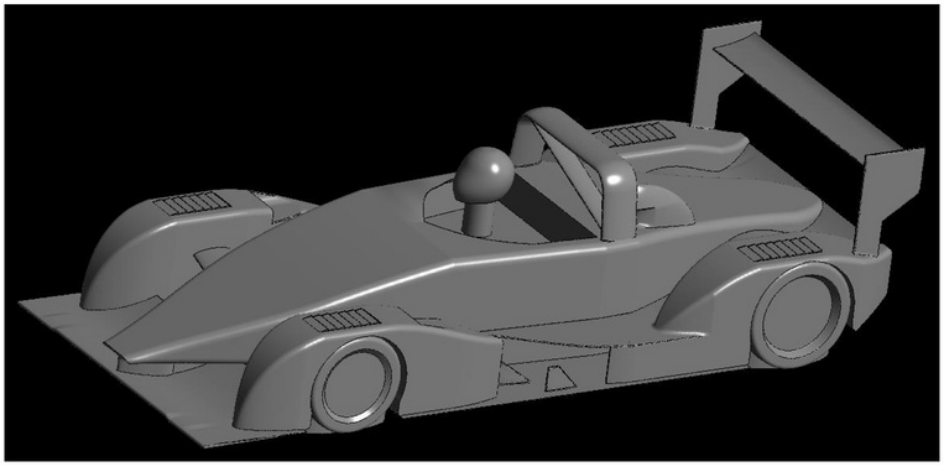


*Figure 36 - Baseline Geometry (JHTT02)*

The geometry illustrated in *Figure 36* shall be maintained as the basis for all future developments, with the focus being on the front wing concept.

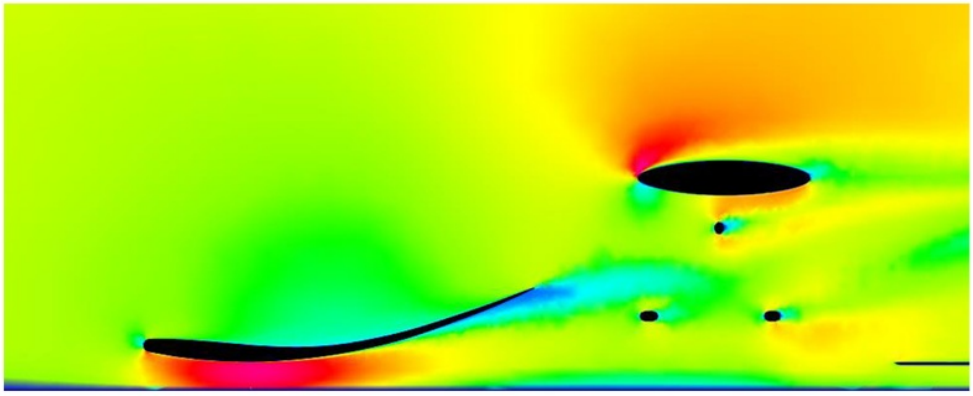


*Figure 37 - JHTT02 Splitter Velocity Contours*

The above figure *(Figure 37),* displays the velocity profile produced by the baseline splitter concept. In its current state, it is evident that flow separation is occurring towards the trailing edge of the splitter. The likelihood is that the developed boundary layer can no longer overcome the adverse pressure gradient that has developed at the rear of the splitter.

It is a possibility that the wishbone shroud is potentially hindering the full performance capabilities of the splitter, creating a large stagnation area of high pressure. However, the purpose of the shroud is beneficial, providing flow control towards the rear of the car.

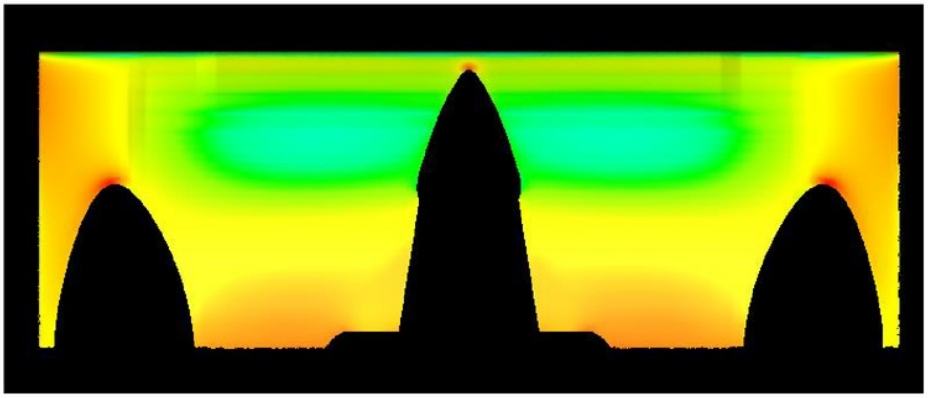


*Figure 38 - JHTT02 Splitter Pressure Contours (Lower Surface)*

*Figure 38* illustrates the working area of the splitter. The distribution of low pressure is confined to the areas between the front wheel pontoons, with high pressure bleeding through onto the edges, limiting the working width of the device. The adverse pressure gradient is also clearly visible towards the trailing edge of the expansion areas, resulting in the voiding of that surface area, and potentially creating an increase in drag.

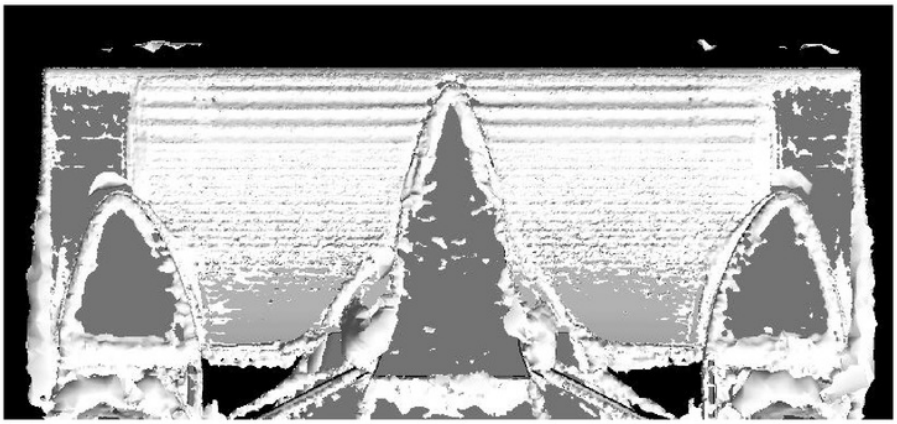
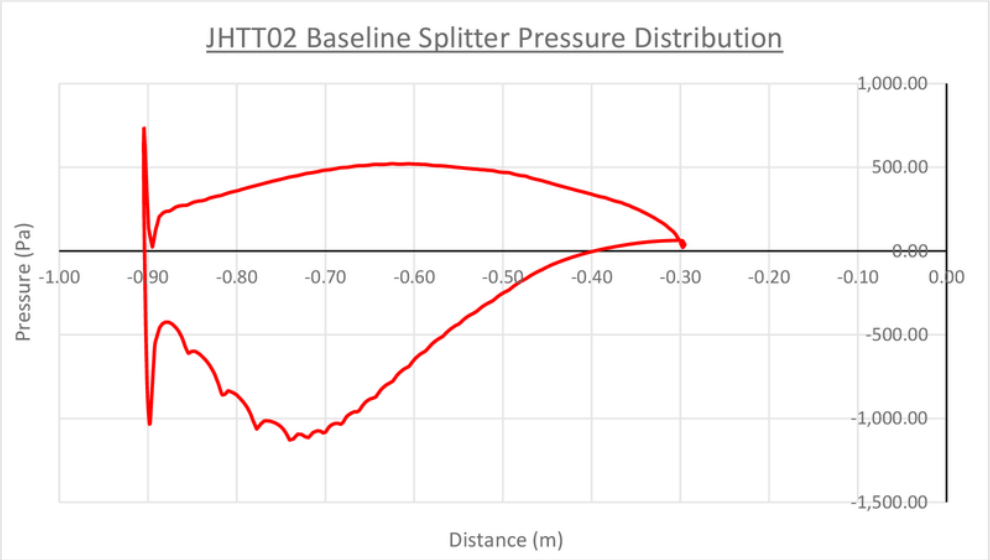


*Figure 39 - JHTT02 Splitter Vortex Generation (Lower Surface)*

*Figure 39* illustrates the generation of lateral vortices on the lower surface of the baseline splitter. The leading edge displays robust vortex generation, which then begins to dissipate towards the trailing edge. The edges remain bare of these rolling vortices, which coincides with the high pressure bleeding evident in *Figure 38*.

Rolling vortex generation is key in boundary layer control, known as the Kutta Condition (Anderson, 1991). With each degree of change in curvature, a vortex is generated as a higher pressure flow just above the boundary, which fills the low pressure void that is left due to the radius. The high energy vortex that is produced then maintains the boundary layer, thus greater angles of expansion can be produced, furthering downforce capabilities. However, adverse pressure gradients can still work against the initial flow vector if the return to atmospheric pressure is compromised or the radius of curvature is too great (Marekk, 2011).




*Graph 4 - JHTT02 Baseline Surface Pressure Distribution*

*Graph 4* indicates surface pressure distribution along the longitudinal axis of the splitter. It is evident that a peak negative pressure slightly in excess of -1000Pa is reached, however it is generated as a peak, rather than as a gradual gradient. It can also be observed that the expansion returns to a pressure above ambient (considered 0Pa), suggesting that a stagnation of high pressure build up behind the splitter is impeding its overall performance, and promoting the observed flow separation.

*Table 4 - JHTT02 Baseline Specification*

| | DRAG (N) | DOWNFORCE (N) | EFFICIENCY | BALANCE (% Front) | FRONT DOWNFORCE (N) | REAR DOWNFORCE (N) | Drag Cd | Lift Cl |
|---|---|---|---|---|---|---|---|---|
| JHTT02 (OSS BASELINE) | 529 | 1549 | 2.93 | 47.56 | 737 | 812 | 0.54 | -1.58 |

In *Table 4,* the figures represent the aerodynamic specification of the entire car. Examination of the figures demonstrates that a 47.56% total distribution of the total downforce exists at the front of the car, thus producing a Cp located 1.36m behind the front wheel centre.

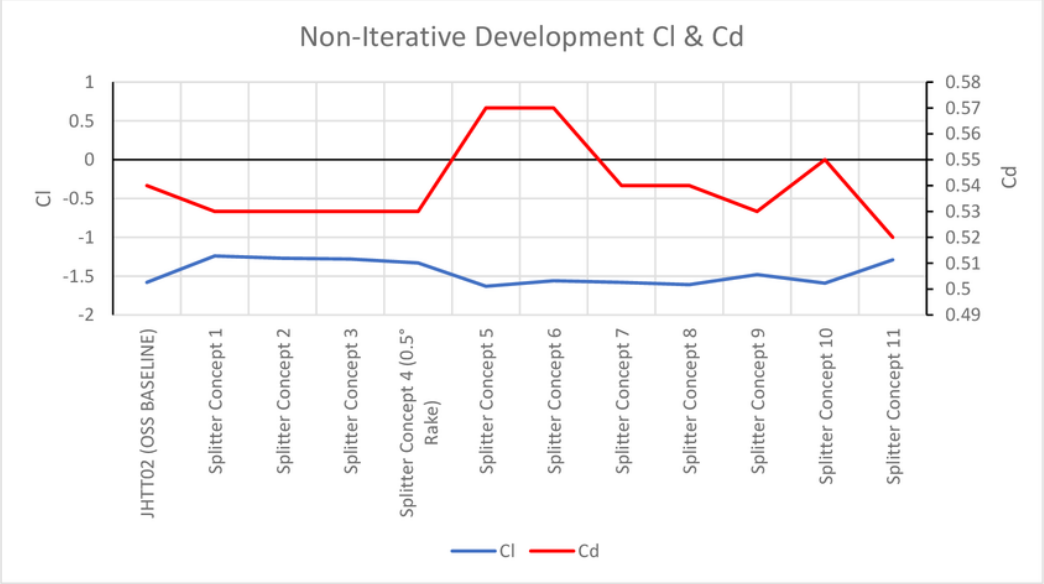
As previous, a mean velocity of 35m/s was applied during the simulation, which shall be maintained throughout the course of this report.

## 4.2.0 Non–iterative Geometry Development

*Table 5 - Non-Iterative Aerodynamic Development Results*

| | DRAG (N) | DOWNFORCE (N) | EFFICIENCY | BALANCE (% Front) | FRONT DOWNFORCE (N) | REAR DOWNFORCE (N) | CoP Distance Behind Coord (m) |
|---|---|---|---|---|---|---|---|
| Splitter Concept 1 | 520 | 1215 | 2.34 | 32.92 | 400 | 815 | 1.74 |
| Splitter Concept 2 | 520 | 1245 | 2.40 | 30.22 | 376 | 869 | 1.81 |
| Splitter Concept 3 | 520 | 1255 | 2.42 | 29.45 | 370 | 885 | 1.83 |
| Splitter Concept 4 (0.5° Rake) | 520 | 1304 | 2.51 | 41.01 | 535 | 769 | 1.53 |
| Splitter Concept 5 | 559 | 1598 | 2.86 | 44.48 | 711 | 887 | 1.44 |
| Splitter Concept 6 | 559 | 1529 | 2.74 | 46.03 | 704 | 825 | 1.4 |
| Splitter Concept 7 | 529 | 1549 | 2.93 | 46.80 | 725 | 824 | 1.38 |
| Splitter Concept 8 | 529 | 1578 | 2.98 | 44.48 | 702 | 876 | 1.44 |
| Splitter Concept 9 | 520 | 1451 | 2.79 | 46.80 | 679 | 772 | 1.38 |
| Splitter Concept 10 | 539 | 1559 | 2.89 | 46.80 | 729 | 829 | 1.38 |
| Splitter Concept 11 | 510 | 1264 | 2.48 | 41.40 | 523 | 741 | 1.52 |

The figures displayed in *Table 5* are the outcomes resulting from the initial development of ideas. This study was conducted in a non-iterative state, meaning that little to no background research or case studies were conducted. This process enabled a basic understanding of how geometrical changes would affect the fluid flow in, and around the entirety of the car. As the table suggests, the eighth concept provided the greatest efficiency, with each study thereafter producing a steady decline in Cl (*Graph 5*).




*Graph 5 - Non-Iterative Development Cl & Cd*

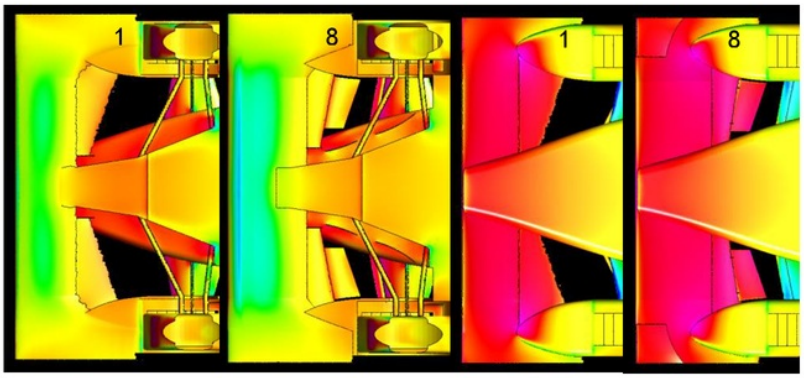



*Figure 40 - Concept 1 & 8 Pressure Contours*

The object of the study was to apply the Formula One concept of introducing multiple elements to improve the workability of the main plane, thus producing a greater pressure differential between upper and lower surfaces. Concept 1 utilises this assertion with the introduction of a secondary element. As demonstrated in *Figure 40*, the main plane chord length has been reduced, though the same profile geometry has been maintained, in order to accommodate the secondary element. Concept 8 is a further development, introducing a third element above the secondary.

Each further element to the main plane in both of the above concepts has an overhang of leading edge to trailing edge and AoA. However, the dimensions were not found through case studies, rather, an approximation of what was deemed to be appropriate.

It is noticeable that the majority of the main plane now has a greater distribution of low pressure across its lower surface in both concepts 1 and 8, compared to that of the baseline geometry in *Figure 38,* although concept 8 has the lowest peak pressure.

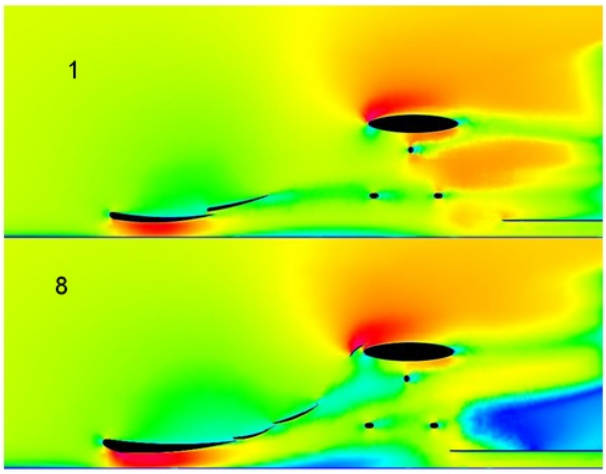
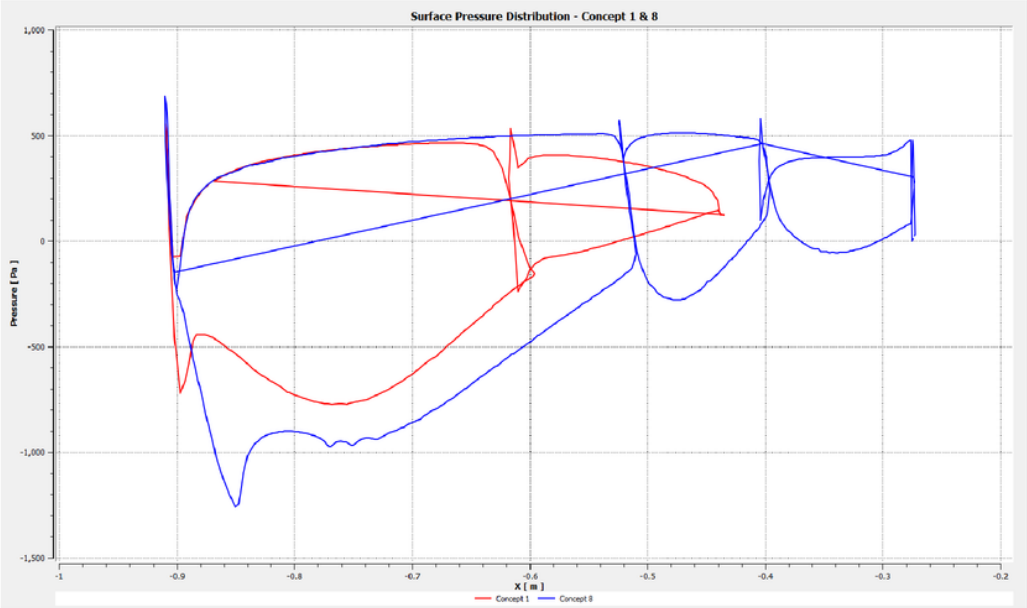



*Figure 41 - Concept 1 & 8 Velocity Contours*

The velocity contours illustrated above (*Figure 41*) are displayed on a plane of a 0.45m distance lateral from the centre of the car.

It is evident that the main plane used in concept 8 has a larger mean camber, with a greater height of the leading edge. This, along with the use of two subsequent elements has allowed the main plane to drive the flow field beneath it, achieving a greater velocity, thus producing a lower pressure, as a larger expansion volume now needs to be utilised.

The wake characteristics between concepts 1 and 8 differ greatly in appearance when compared. Concept 8 produces a greater flow upwash, which subsequently begins to interact with the wishbone shrouding, potentially impeding its overall performance as has been previously stated.




*Graph 6 - Concepts 1 & 8 Surface Pressure Distribution*

*Graph 6* illustrates the surface pressures produced by both concepts (concept 1, red and concept 8, blue). It is clear that concept 8 generates a much greater pressure differential, with a low pressure that returns back to an atmospheric state in a gradual gradient. However, a sharp peak is displayed in low pressure at the leading edge, though this is as a result of initial geometry inaccuracies when creating the CAD model.

# 5.0.0 Methodology, Results & Analysis

Creating a non-iterative development provided a general understanding of the affects a geometry change would have on the overall fluid flow. However, in order to gain a comprehensive understanding of the way in which multiple aerofoils interact with each other when modelled as a multi-element wing, it was considered prudent to conduct a full case study (Tudor, 2018), beginning with the main plain optimisation, to then introduce further aerofoil elements.

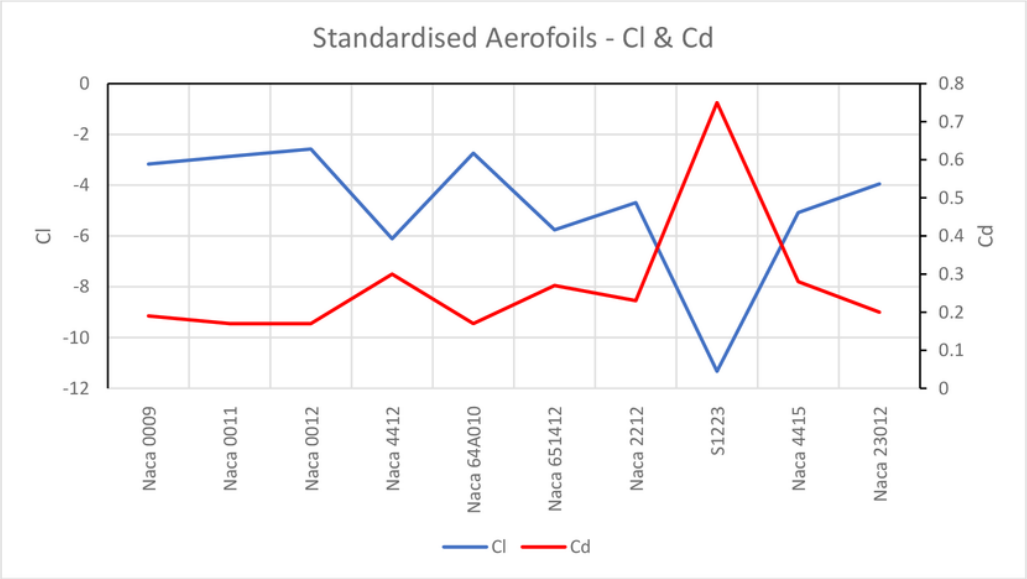
## 5.1.0 Aerofoil Selection

A decision to use standardised aerofoil profiles was made. This enables a greater understanding of aerofoil interaction, rather than the full development of a single custom aerofoil, thus saving time in the completion of the main objective.

*Table 6 - Standardised Aerofoils*

| | DRAG (N) | DOWNFORCE (N) | DOWNFORCE (KG) | EFFICIENCY |
|---|---|---|---|---|
| Naca 0009 | 50.18 | 837.23 | 85.3 | 16.68 |
| Naca 0011 | 44.90 | 758.00 | 77.3 | 16.88 |
| Naca 0012 | 44.90 | 681.40 | 69.5 | 15.18 |
| Naca 4412 | 79.23 | 1613.71 | 164.5 | 20.37 |
| Naca 64A010 | 44.90 | 723.66 | 73.8 | 16.12 |
| Naca 651412 | 71.31 | 1521.27 | 155.1 | 21.33 |
| Naca 2212 | 60.75 | 1238.68 | 126.3 | 20.39 |
| S1223 | 198.08 | 2992.37 | 305.0 | 15.11 |
| Naca 4415 | 73.95 | 1341.68 | 136.8 | 18.14 |
| Naca 23012 | 52.82 | 1043.23 | 106.3 | 19.75 |

*Table 6,* indicates the base aerodynamic characteristics of the aerofoils under consideration. Each aerofoil was scaled to achieve the same chord length, representative of the splitter chord length and span as indicated on the concepts illustrated in chapter 4.2.0. This enables relativity between each aerofoil, therefore comparisons can be made within analysis state.




*Graph 7 - Standardised Aerofoils - Cl & Cd*

Each aerofoil was simulated with a 40mm ground clearance and 1° AoA, thus inducing ground effect. The reason for this is due to the final position of the aerofoil on the car, where it would be assumed that the distance of the final profiles from the ground would enable a ground effect to occur.

Both the Naca 4412 and S1223 profiles produced the highest -Cl values (*Graph 7*), although the Naca 653412 produced the greatest aerodynamic efficiency, with the S1223 producing the lowest efficiency as a Cd value of 0.75 had been calculated, the highest of all the profiles.

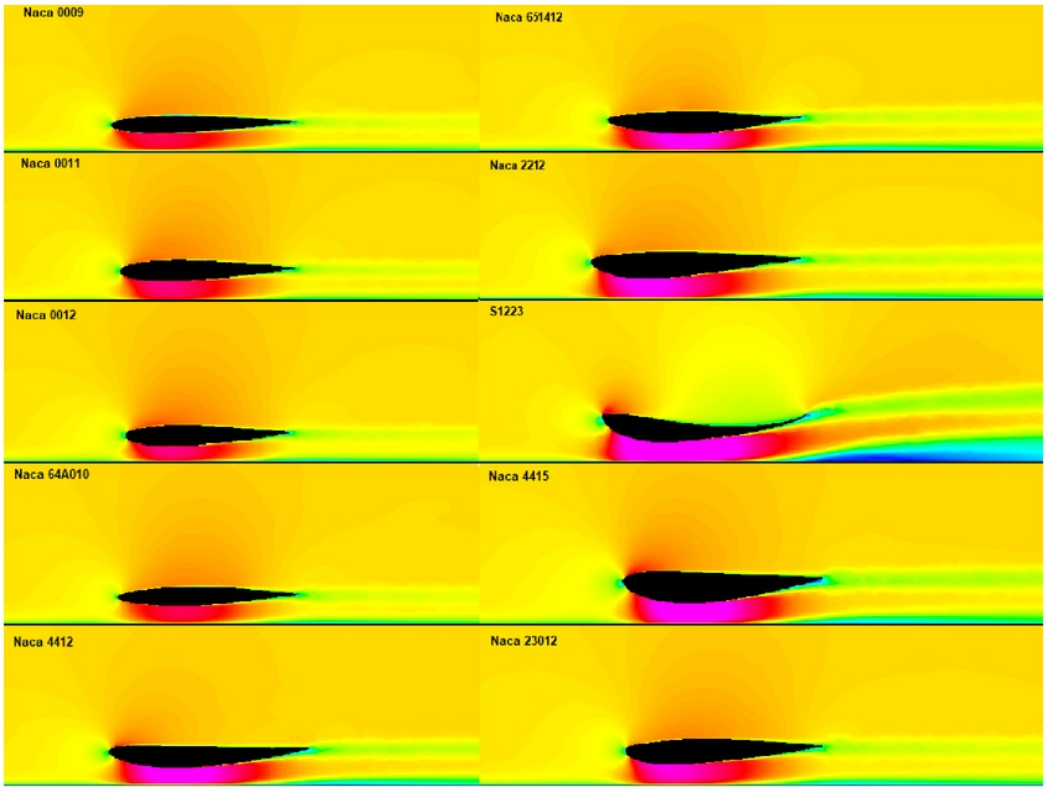



*Figure 42 - Standardised Aerofoils (Velocity Contours)*

The velocity contours above (*Figure* 42), represent the flow velocity for each of the profiles that were investigated. The majority of the investigations involved the use of symmetrical profiles, therefore, efficiency values are greater due to the low values of Cd, however, minimal Cl values are also generated.

Visually, the S1223 profile generates the greatest flow upwash, as it could be considered to have the greatest expansion volume, along with the most aggressive mean camber.

The Naca 4412 also generates larger values of -Cl, coming second to that of the S1223, but once again, also generates a considerable drag value, which is lower than that of the S1223.

It is also noticeable that both the Naca 4412 and S1223 utilise a greater surface area of velocity distribution on their lower surfaces compared to that of the other profiles tested, leading to a larger pressure differential. This geometry characteristic, alongside the greater expansion volumes provides confidence in the intended purpose, if they were installed on a car.

## 5.2.0 Naca 4412 & S1223 Profiles

The S1223 profile is considered to be a "*high lift*" aerofoil. It has been observed and discussed how the geometry creates a pressure recovery by concaving its trailing edge and utilising a rear loading situation due to the expansion volume within the profile's geometry (Selig, et al., 1995).

The Naca 4412 profile is often utilised as an aircraft aerofoil, where research strongly promotes its excellent capabilities when used in ground effect situations, which makes it superior for use on low flying aircraft (Abdullah, et al., 2017).

Observing the two profiles, their forms differ in several ways, however both present favourable characteristics when considered for utilisation in a front wing formation.

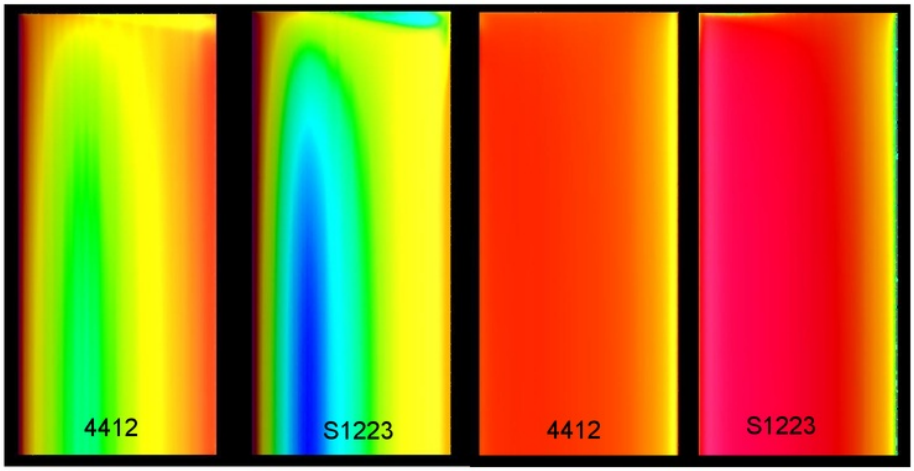
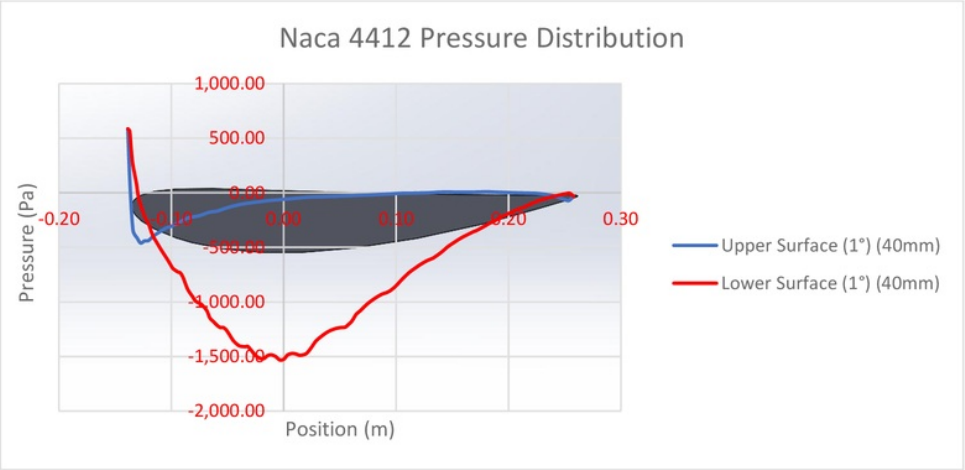



*Figure 43 - Naca 4412 & S1223 Surface Pressure Contours*

Surface pressure contours (*Figure 43*), display similar traits in pressure distribution when both the Naca 4412 and S1223 profiles are compared. It is, however, noticeable that the S1223 has a greater concentration of pressure distribution, with a peak in low pressure confined to a small area on its lower surface, whereas the Naca 4412 has a more even distribution, with less defined concentration. As end plates are not applied, a spill of pressure around the outer edge is evident in both cases.

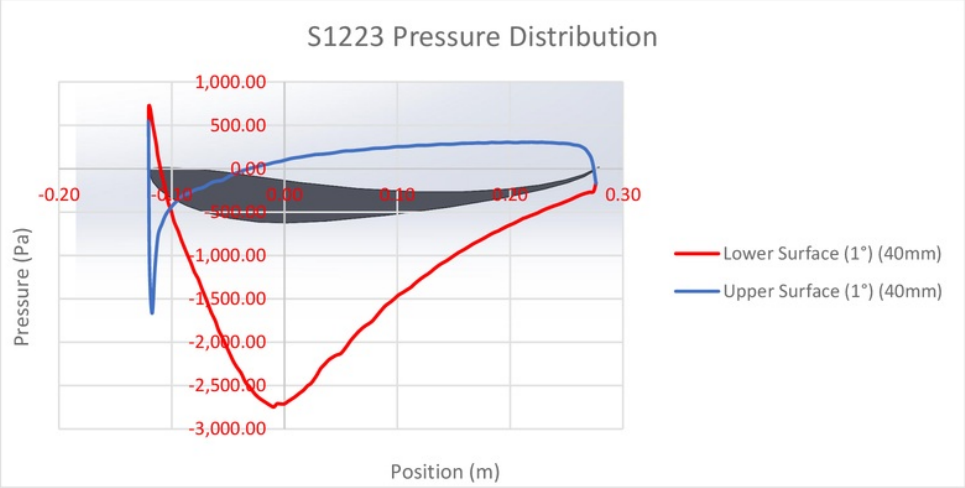
The strength of the positive pressure developed on the upper surfaces of both profiles also has a similar distribution, however, the concaved surface of the S1223 profile delivers a greater pressure gradient, leading to an increased pressure differential between upper and lower surfaces.




*Graph 8 - Naca 4412 Pressure Distribution*

*Graph 8,* indicates that the pressures developed on both the upper and lower surfaces differ. This allows the pressure differential to work in a downward vector, thus downforce is created.

The displayed graph illustrates pressure gradients relative to atmospheric pressure, therefore atmospheric pressure is considered as 0Pa. A maximum peak negative pressure of -1500Pa exists. The gradient achieved describes the intensity of the pressure, illustrating a gradual curve, this would then suggest a more predictable working wing. The upper surface pressure does not deviate above atmospheric pressure, with the leading edge producing a below atmospheric pressure condition as the air velocity is increased as it passes over the upper curve.




*Graph 9 – S1223 Pressure Distribution*

The S1223 profile pressures (*Graph 9*) differ considerably when compared to those indicated in *Graph 8*. A maximum low pressure of over -2500Pa is achieved. This is as a result of the highly cambered geometry observed in the profile. Rather than producing a gradual gradient in pressure, an intensity is achieved with 0.15m on its leading edge, suggesting that the wing could become unpredictable in a dynamic situation, if it were applied to a race vehicle, where ride heights constantly vary.

As discussed, the concaved upper surface encourages the development of an increased positive pressure, with a peak pressure of 260Pa being achieved. This characteristic creates a much larger pressure differential between the upper and lower surfaces, compared to that of the Naca 4412.

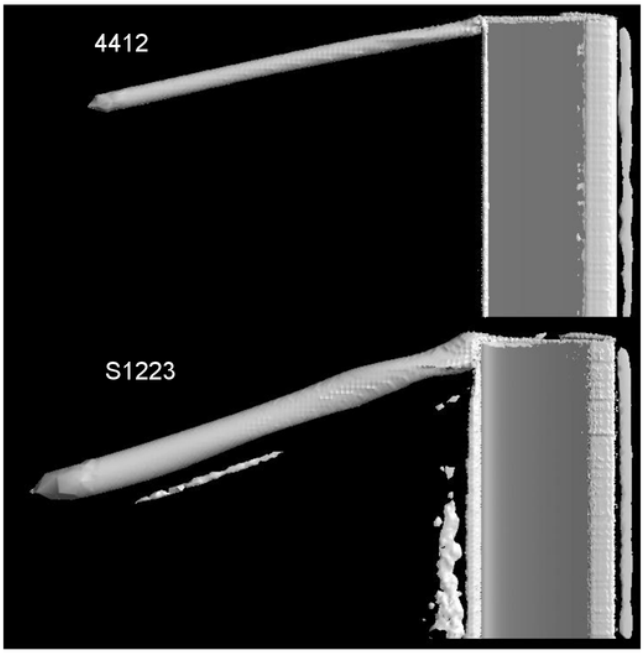



*Figure 44 - Naca 4412 & S1223 Upper Surface Vortices*

As a greater pressure differential exists, the positive pressure gradient that is generated, is generated with a greater intensity. As *Figure 44,* illustrates the stronger pressure gradient then develops into a much larger trailing vortex, as the positive pressure spills around onto the lower surface of the wing. This action produces a strong swirling circulation, which then absorbs energy from the free stream fluid flow, causing the wing to generate a higher drag force value, as more turbulent air is produced.

It can also be observed that the S1223 profile creates a much larger lateral trailing edge vortex. This larger vortex occurs is as a result of the higher pressure above the boundary

layer filling the small void that is left towards the trailing edge on the lower surface due to separation (*Figure 45*), creating a re-circulating characteristic (displayed with white arrow).

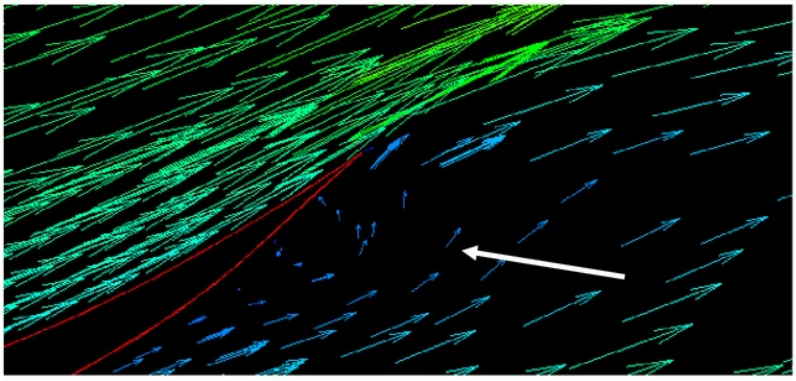


*Figure 45 - S1223 Trailing Edge Velocity Vectors (Vortex)*

As the pressure differential is much greater on the S1223 compared to that of the Naca 4412, the trailing edge vortex that is developed is much more disruptive to the laminar flow. Subsequently, the vortex lowers the pressure on the upper surface trailing edge and raises the pressure on the lower surface trailing edge, seen in *Figure 43*.

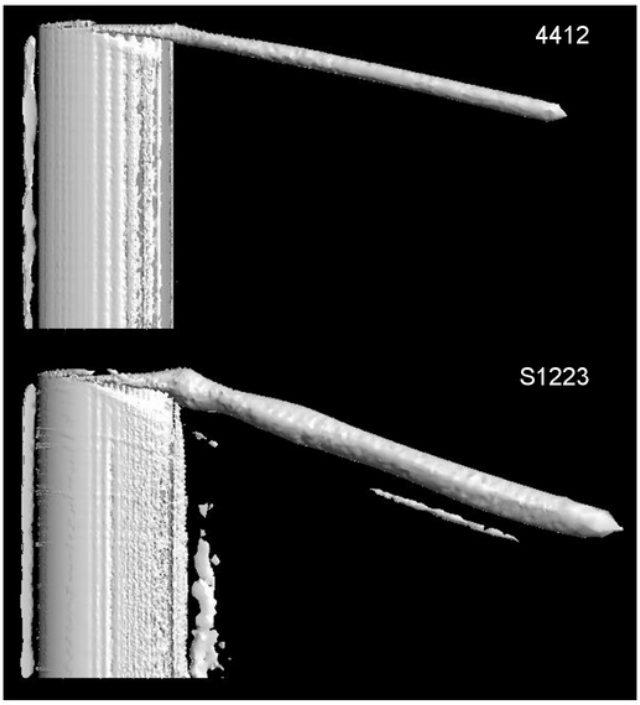



*Figure 46 - Naca 4412 & S1223 Lower Surface Vortices*

A lateral vortex is also generated on the ground, immediately forward of the leading edge. This is as a result of the mixing of pressures and the flow vectors working in opposing directions as illustrated in *Figure 47*.

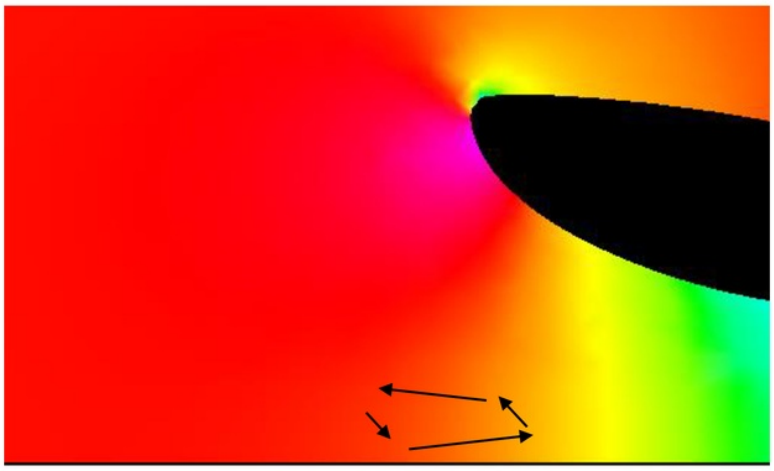


*Figure 47 - Leading Edge Vortex Generation*

This lateral vortex is generated at ground level and creates a small blockage for air to travel over, thus a greater venturi effect is observed.

5.2.1 Height Study (Naca 4412 & S1223)

An investigation into how the two profiles perform under different heights was undertaken in order to provide further insight into how both profiles would react in a dynamic condition, and also suggesting a potential static height for the implementation of the profiles on the vehicle. Traditionally, the distance from the ground is measured in a ratio.

$$Distance\ to\ Ground\ Ratio = \frac{Height}{Chord}$$

*Equation 10 - Distance to Ground Ratio*

It has been observed that the Naca 4412 profile works at its most efficient when at its chord length distance from the ground, therefore equating h/c as 1 (Abdullah, et al., 2017). The expression of the distance to ground as a ratio has also be expressed by others (Durrer, 2016). However, for the purpose of this study the distance to ground will be defined as a measurement of height in millimetres.

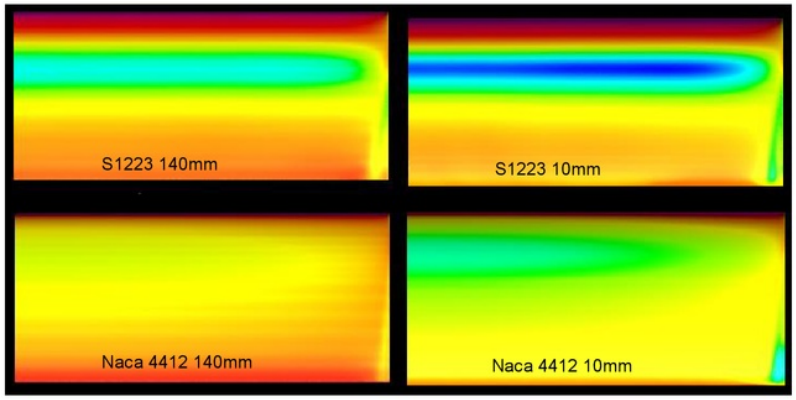



*Figure 48 - Naca 4412 & S1223 Maximum & Minimum Heights (Pressure Contours)*

*Figure 48,* illustrates the lower surface pressure contours on both of the aerofoils being considered. In both cases, as the aerofoils are lowered further toward the influence of ground effect, a greater concentration of low pressure is generated, with the S1223 producing a greater intensity. This is also evident at a height of 140mm, however, the Naca 4412 has a much smoother pressure gradient, with the pressure gradually returning back to atmospheric. It is also noticeable that the S1223 has a greater area of peak low pressure when at 140mm compared to the Naca 4412 at a height of 10mm.

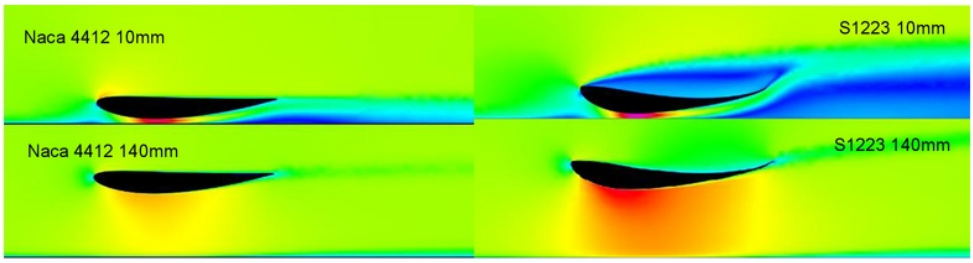



*Figure 49 - Naca 4412 & S1223 Maximum & Minimum Heights (Velocity Contours)*

*Figure 49,* also defines the working state of the profile in terms of velocity flow. As anticipated, the S1223 displays a much greater velocity of fluid flow on its lower surface, although, when at a height of 10mm, its upper surface has a large area of recirculating air.

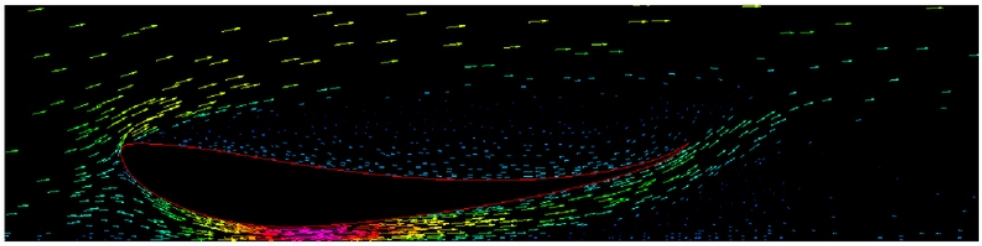
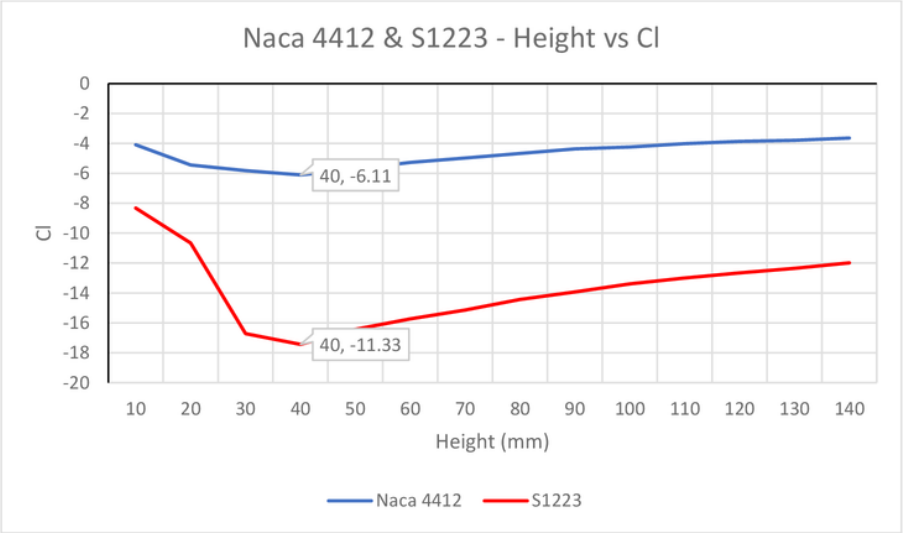


*Figure 50 - S1223 10mm (Velocity Vectors)*

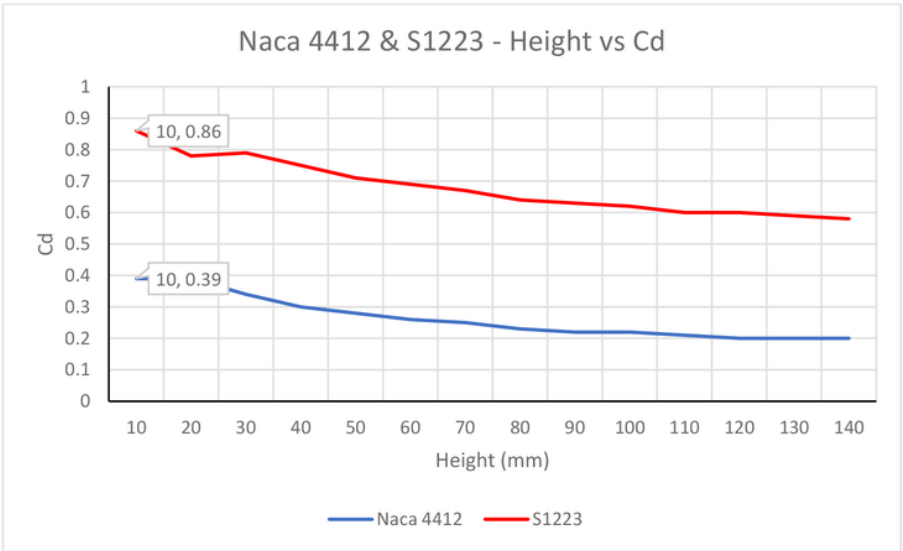
As the image *(Figure 50)* above illustrates, the boundary layer is not able to maintain its vector along the upper surface. Reducing the height has also increased the intensity of the lateral vortex produced immediately forward of the leading edge, which has resulted in the change of trajectory of the freestream flow into an increased gradient upward. Being unable to maintain such a severe change in direction around the leading edge, has caused separation, which has furthermore been exacerbated by the concaved geometry.

The same influence is also evident on the Naca 4412, however, the boundary flow is maintained along its upper surface as the trajectory change is not as dramatic.




*Graph 10 - Naca 4412 & S1223 - Height vs Cl*

Both profiles indicate a reduction in Cl as the height is reduced below 40mm. This is due to the blockage effect generated by the lateral ground vortex located in front of the profiles. However, the S1223 experiences a greater disruption in fluid flow, as indicated in *Graph 10.* As the height of the profiles is increased above 40mm, both profiles show a gradual reduction in Cl as ground effect has a lesser impact on the working nature of the profiles.




*Graph 11 - Naca 4412 & S1223 - Height vs Cd*

Wing drag values are assumed to reduce as the distance of the aerofoil from the ground is increased. This is a result of the decreasing interaction between the wing and the ground. As

has already been stated, as downforce is increased, a subsequent drag factor will become apparent.

This is the case indicated in *Graph 11*, with both the investigated profiles showing similar trends, however, the S1223 displays a constantly higher value of Cd.

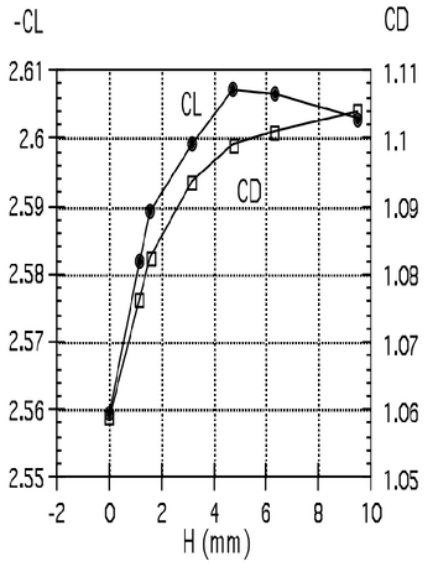
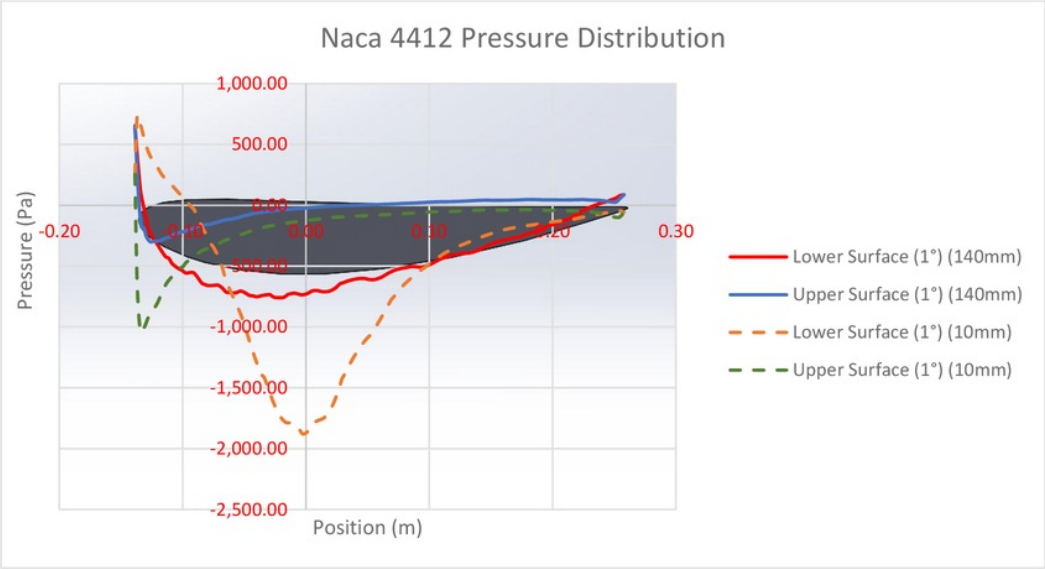


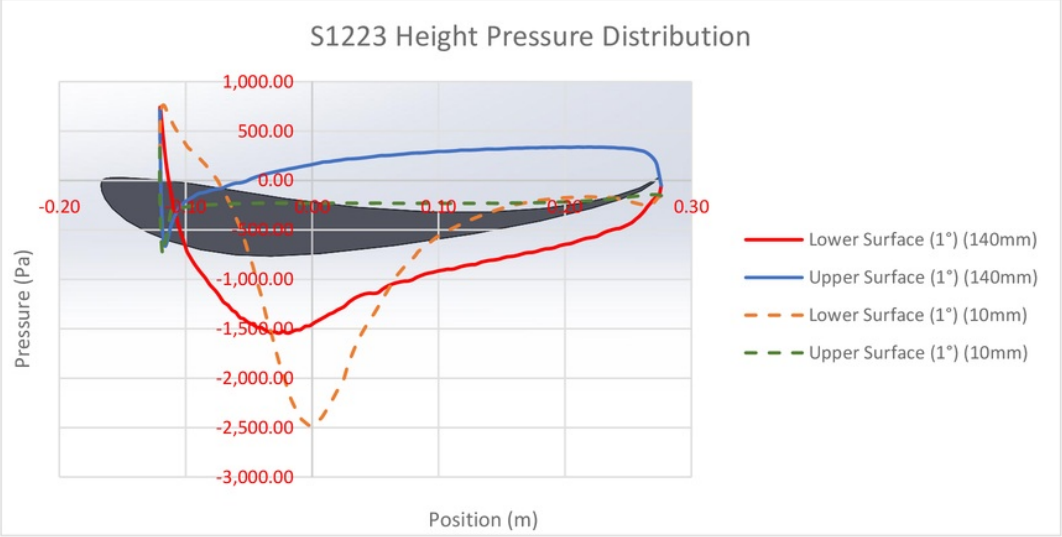

*Figure 51 - Height vs -Cl & Cd (Katz, 1995)*

Cl and Cd have been described in relation to height (Katz, 1995), illustrated in *Figure 51*. It is evident that both the Naca 4412 and S1223 profiles follow the same trends as indicated in *Figure 51*, although the S1223 is distinctly more sensitive to reduced height changes.




*Graph 12 - Naca 4412 Pressure Distribution (10mm & 140mm)*

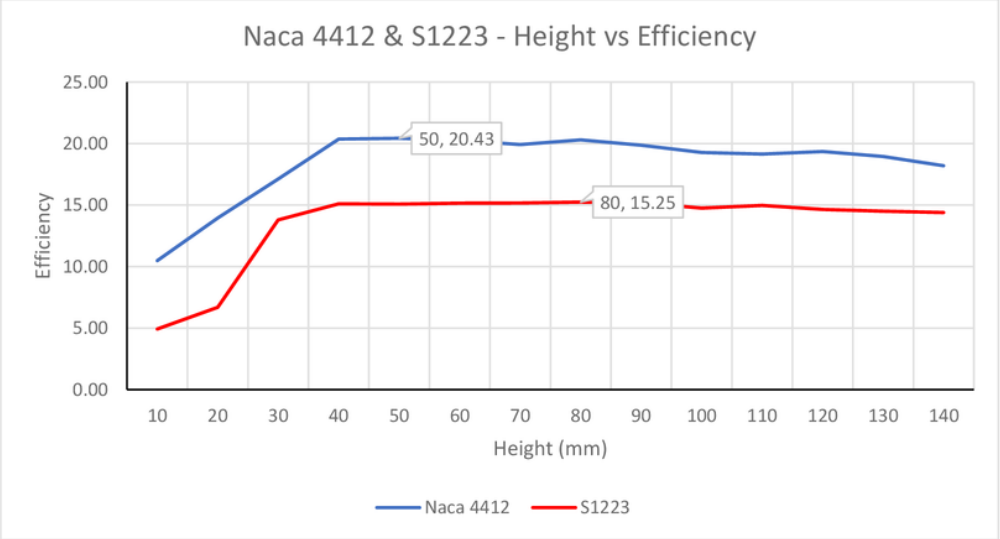
As the distance from the ground is reduced, the lower surface negative pressure is increased. Illustrated in *Graph 12* and *13*, the difference in pressure on the lower surface has a much greater peak at a lower height, however, the peak pressure is concentrated in a small area. This implies that the height of the aerofoil can have an impact on the predictability of the wing.




*Graph 13 - S1223 Pressure Distribution (10mm & 140mm)*

As the height of the aerofoil is increased, the gradient of curvature is greatly reduced, with an almost linear pressure increase back to atmospheric conditions. This then allows a greater area of negative pressure, which uses more of the available wing surface area.

*Graph 13,* also indicates the result of the upper surface air recirculation, observed when the S1223 profile is at a distance of 10mm from the ground. Noticeably, the surface pressure remains below atmospheric pressure throughout its entire chord length. This is in contrast to a ground distance of 140mm, where a maximum positive pressure of 400Pa is apparent.




*Graph 14 - Naca 4412 & S1223 - Height vs Efficiency*

*Graph 14,* describes the aerodynamic efficiency of both profiles in relation to their height. The efficiency of the profile is also related to its surface pressure distribution. It can be assumed, therefore, that the sharper pressure gradients have a negative effect on the profiles working efficiency.

As the Naca 4412 has a smaller pressure gradient, its maximum efficiency is achieved 30mm closer to the ground compared to that of the S1223. However, it is also noted that the peak negative pressure achieved at a height of 140mm on the S1223 is within 500Pa of the peak negative pressure achieved by the Naca 4412 at a height of 10mm.

This suggests that it may be possible to install the S1223 profile on the race car at a greater height, and retain the same performance as the Naca 4412 in terms of ground effect.

5.2.2 Angle of Attack Study (AoA) (Naca 4412 & S1223)

It is often suggested that to increase the production of Cl by a wing, its AoA can be increased, thus generating an increased Coanda effect. However, a limit is reached when the lower boundary layer can no longer overcome the strength of the adverse pressure gradients that have been created, with the gradient becoming larger as the AoA is increased (Panchal , 2015).

It is, therefore, essential that the working range of AoA is found for both of the profiles being investigated. This will then be of great value for further case studies.

The Naca 4412 and S1223 profiles were both retained at a height of 40mm, however, AoA increases were made in 1 degree increments up to 15 degrees, in order to try and induce a stalling situation, where the generated Cl begins to reduce sharply.

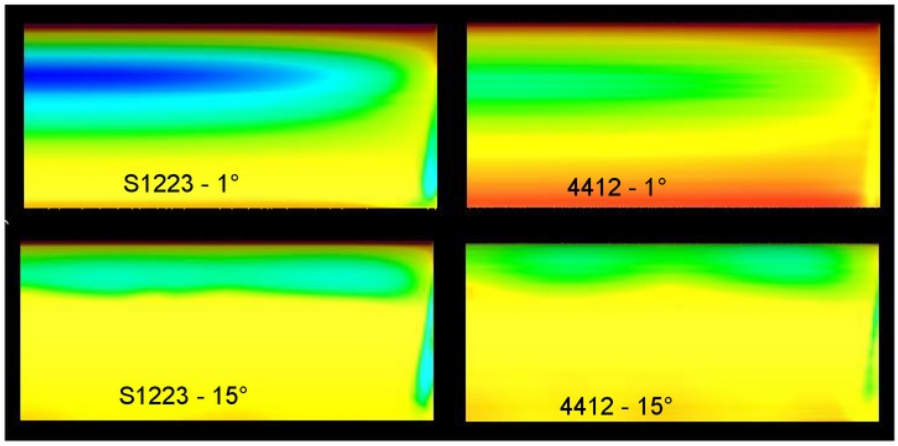



*Figure 52 - Naca 4412 & S1223 Lower Surface Pressure Contours (1° - 15°)*

As *Figure 52* illustrates, as the AoA is increased, the area of peak low pressure decreases in size. The gradient at which the pressure returns to atmospheric has also visibly increased.

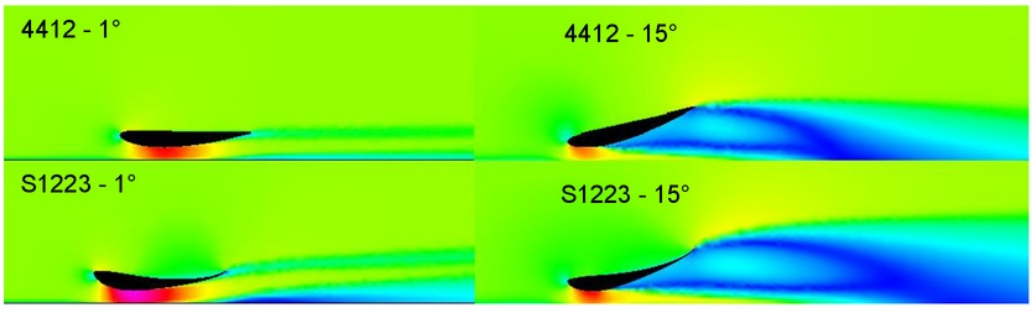



*Figure 53 - Naca 4412 & S1223 Velocity Contours (1° - 15°)*

As the AoA is increased, the location of the concentration of peak low pressure is repositioned closer to the leading edge of the profile. Both profiles produce large wake formations at the 15 degrees AoA. *Figure 53,* illustrates the changes in trailing edge disturbance that have occurred, with both aerofoils generating similar formations of wake structure. However, the S1223 aerofoil is producing the larger wake of the two, with a lower pressure, therefore maintaining a greater pressure differential between surfaces, although, the larger wake formation would suggest a significant amount of induced drag production.

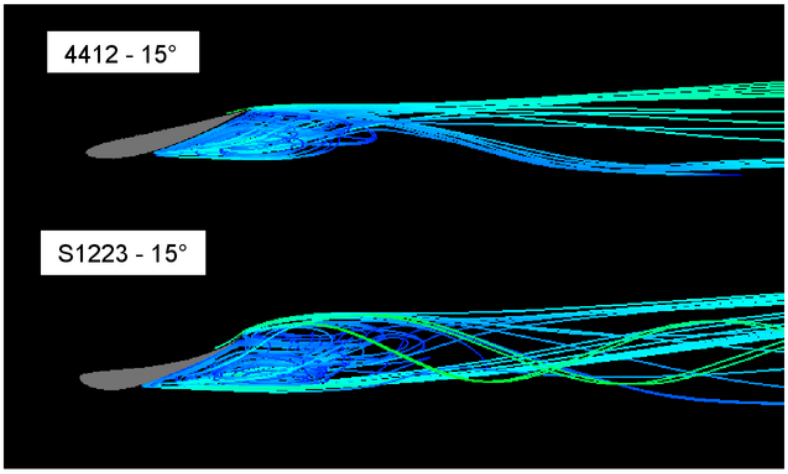
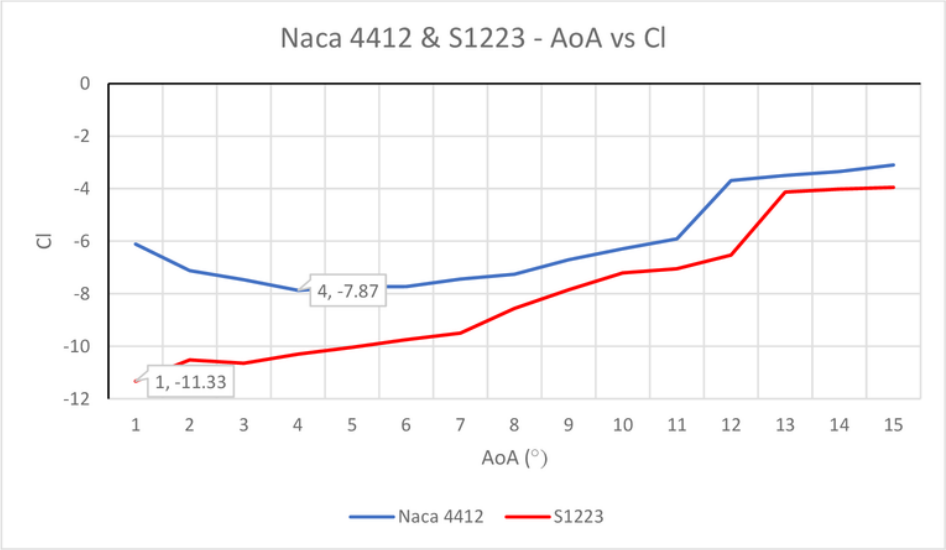


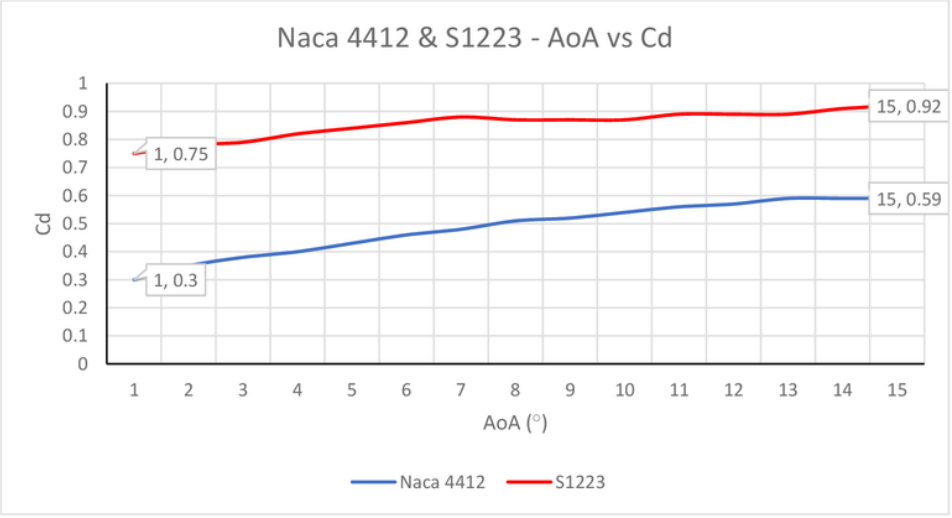

*Figure 54 - Naca 4412 & S1223Velocity Streamlines (15°)*

Large areas of recirculation are produced as a result of the increased AoA, as the above figure illustrates (*Figure 54*). When further AoA is added, the frontal area blocking the smooth transition of flow over the wing is also increased, therefore, producing a void of increasing size on the lower surface, which then needs to be filled. With a constant velocity flow, this creates a circling motion of air, thus the induced drag is increased as the low pressure void resists the forward motion of the wing.



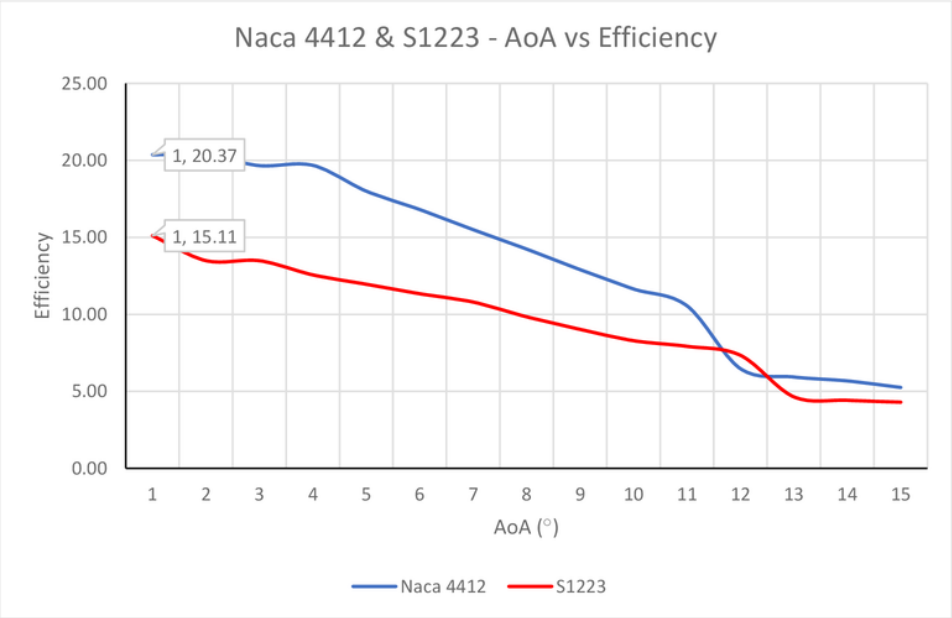

*Graph 15 – Naca 4412 & S1223 – AoA vs Cl*

As has already been observed, the geometries of both profiles differ greatly. The highly cambered nature of the S1223 means that an increase in AoA makes no further improvement to its generation of Cl. However, a 4 degrees AoA for the Naca 4412 profile produces its highest value of Cl, which therefore suggests that AoA creates a smaller difference in Cl compared to a height difference. It can also be observed that both wings suffer a stalling moment at 11 degrees and 12 degrees respectively, as indicated in *Graph 15*, where a sharp decrease in Cl is prominent.



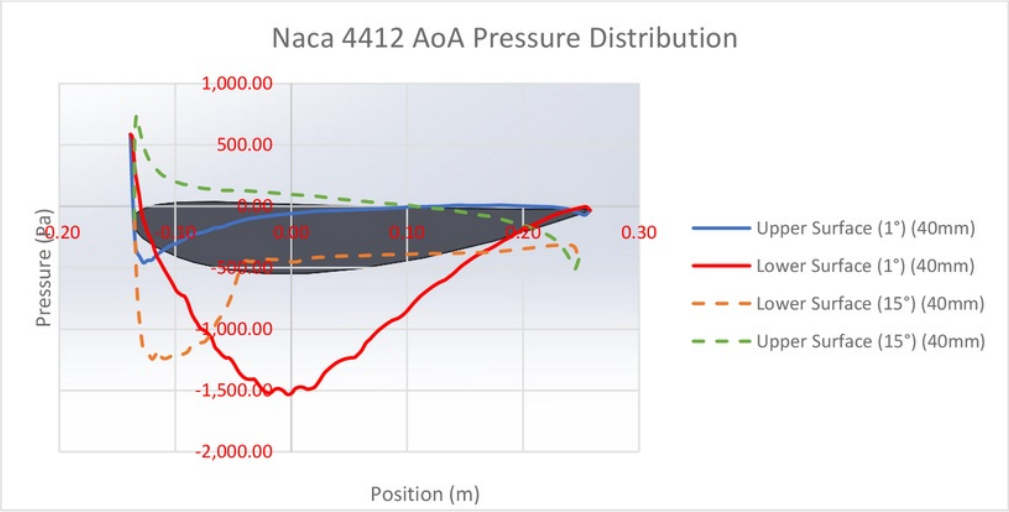

*Graph 16 - Naca 4412 & S1223 - AoA vs Cd*

*Graph 16,* illustrates the increase in Cd as the AoA is increased. As has already been stated, together with a greater gradient, a further induced value of Cd is produced. Unlike the Cl values illustrated in *Graph 15,* there is no sudden decrease or increase in Cd value. A shallow gradient increase in Cd is apparent, where it is evident that further AoA makes no further Cd increase.




*Graph 17 - Naca 4412 & S1223 - AoA vs Efficiency*

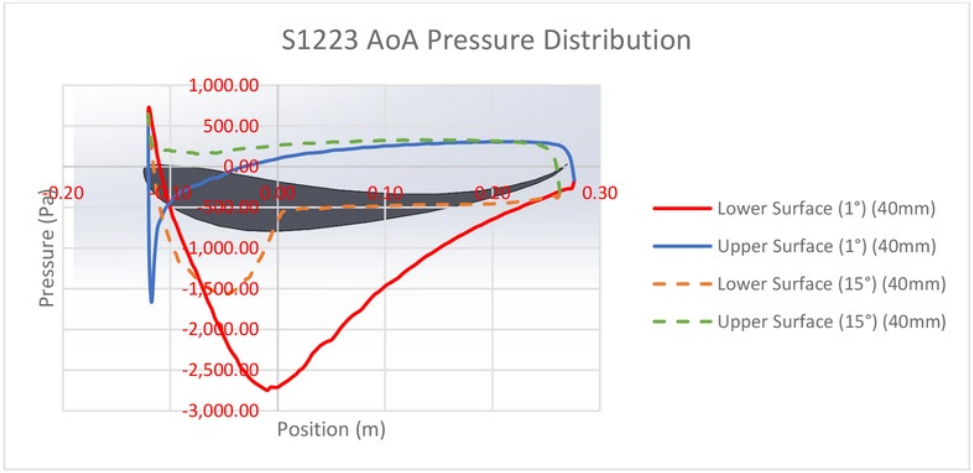
*Graph 17,* indicates that as AoA is increased, the aerodynamic efficiency of the aerofoils decreases. A representation of the sudden decrease in Cl is also apparent in the above graph *(Graph 17)*, which suggests that low AoA produces an improved efficiency and a potentially greater working surface area, thus, providing further predictability.




*Graph 18 - Naca 4412 Pressure Distribution (1° - 15°)*

The profile pressure distributions, indicated in *Graphs 18* and *19,* display the sharp gradient change in pressure on the lower surfaces. This is as a result of the flow separation phenomenon that has occurred at the 15 degrees angle of attack. It can also be observed that the peak negative pressures at the highest AoA are both lower when compared to a shallow AoA, therefore a lower pressure differential is created, which produces less downforce.

The change in location of the peak negative pressure is also apparent, which is more extreme in the case of the Naca 4412, thus, shifting the Cp forward consequently produces a lesser balanced wing.




*Graph 19 - S1223 Pressure Distribution (1° - 15°)*

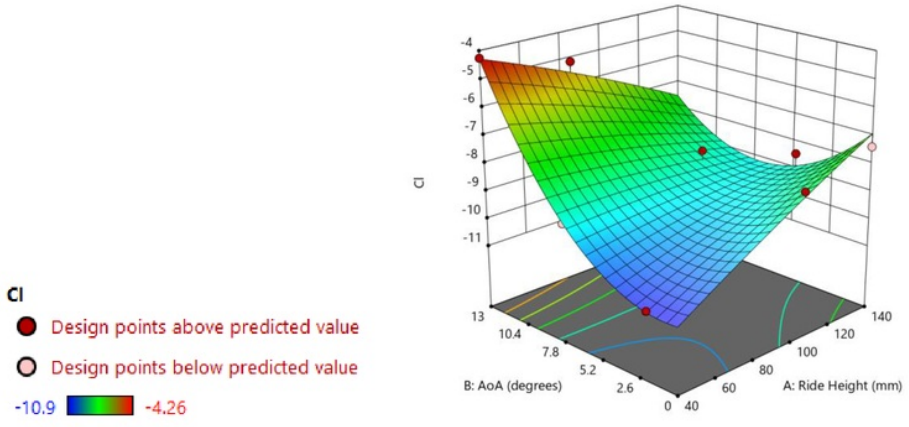
## 5.3.0 Design of Experiments

The purpose of DOE is to minimise the amount of testing and simulation undertaken, but achieving the same outcome. A number of input variables can be initialised with the number of desired responses (Proust, 2009).

By minimising the test numbers, management of time can be appropriately maintained. The software syntax builds a response curve based on the input variables and the given responses defined by the user. The curve fit can be adjusted, based on the defined experiment, allowing different curve equations to be used, providing further reliability within the predictions that have been made. Once the curve is constructed, an optimisation of the design can commence, with the software being able to produce a confidence percentage and a desirability factor for the design provided (Condra, 1991).

### 5.3.1 Main Plane - S1223: Height vs AoA

Following the previous studies conducted, the S1223 profile was selected to be used as the main plane. The judgement made was based on the powerful nature of the profile, and considerations were made regarding the ability of the Naca 4412 when installed on the race car, and whether interactions between the car and the Naca 4412 would compromise its effective working area.




*Graph 20 - S1223 Main Plane DOE Study (Cl)*

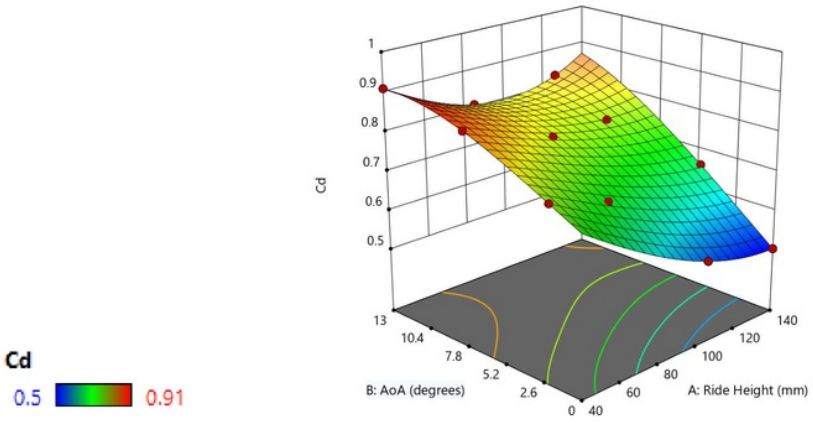
*Graph 20,* illustrates the interactions between AoA and height with the resultant Cl. Due to the negative description of Cl, the displayed graph is reversed, therefore the blue colouration indicates the highest Cl and red colouration indicates the lowest Cl.

The maximum and minimum inputs were based on the stand alone investigations detailed in chapters 5.2.1 and 5.2.2, and displayed in *Table 7*.

*Table 7 - S1223 Main Plane DOE Maximum & Minimum Input Variables*

| Input Variable | Minimum | Maximum |
|---|---|---|
| AoA (°) | 0 | 13 |
| h (mm) | 40 | 140 |

*Graph 20* suggests that a minimum AoA, together with the lowest height achieves the highest -Cl, with AoA creating a greater gradient loss of -Cl compared to height.




*Graph 21 - S1223 Main Plane DOE Study (Cd)*

*Graph 21,* further describes the interaction between AoA and height, in terms of Cd. Again, it can be seen that that a minimum AoA and the maximum height results in the lowest Cd.

Based on these results, it can be advised that a minimum AoA used, however, ride height is yet to be confirmed.

### 5.3.2 Main Plane Discussion

*Table 8 - S1223 Main Plane DOE Study Results*

| Height (mm)/AoA (°) | DRAG (N) | DOWNFORCE (N) | DOWNFORCE (KG) | EFFICIENCY | Cd | Cl |
|---|---|---|---|---|---|---|
| 40/1.95 | 203.36 | 2878.80 | 293.5 | 14.16 | 0.77 | -10.9 |
| 40/7.41 | 229.78 | 2392.84 | 243.9 | 10.41 | 0.87 | -9.06 |
| 40/13 | 240.34 | 1125.11 | 114.7 | 4.68 | 0.91 | -4.26 |
| 75/2.86 | 184.88 | 2627.89 | 267.9 | 14.21 | 0.7 | -9.95 |
| 82.5/13 | 213.93 | 1357.53 | 138.4 | 6.35 | 0.81 | -5.14 |
| 82.5222/7.42384 | 208.65 | 2424.53 | 247.1 | 11.62 | 0.79 | -9.18 |
| 103/0 | 142.62 | 2139.29 | 218.1 | 15.00 | 0.54 | -8.1 |
| 118./8.385 | 203.36 | 2234.37 | 227.8 | 10.99 | 0.77 | -8.46 |
| 125/13 | 219.21 | 1891.03 | 192.8 | 8.63 | 0.83 | -7.16 |
| 140/0 | 132.06 | 1946.49 | 198.4 | 14.74 | 0.5 | -7.37 |
| 140/4.68 | 174.31 | 2226.45 | 227.0 | 12.77 | 0.66 | -8.43 |

*Table 8,* indicates the numerical input factors that the DOE software requested, together with the resultant outcomes. Not only are the individual factors of Cl and Cd considered, further assessments must be made regarding efficiency, therefore, maximum -Cl may not be achievable with the optimum aerodynamic efficiency.

As the results in *Table 8* show, the greatest efficiency outcomes often result from minimum AoA.

Lower heights may achieve a greater -Cl with a minimum impact upon efficiency, however, thought must be given to its application to the car in a dynamic situation, where constant changes in ride height must be considered. Therefore, it may be advisable to consider a greater ride height with a minor sacrifice in frontal downforce.

### 5.3.3 S1223 Main Plane Optimisation

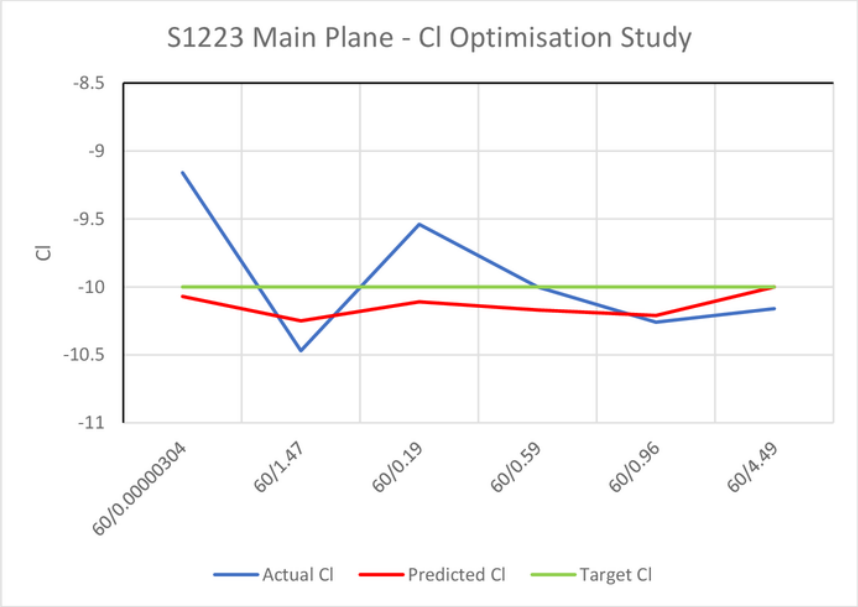
During optimisation, further restrictions can be applied to the input variables in order to achieve the desired outcomes. For this optimisation study, a maximum target Cl of -10 was selected with a maximum Cd of 0.7, which provides a target efficiency of 14.29.

A height range of 40mm to 60mm and an AoA range of 0° to 13° were selected as working variables. Therefore, the target Cl and Cd had to be achieved within the given h and AoA factors.

*Table 9 - S1223 Main Plane Optimisation Desirability Factors*

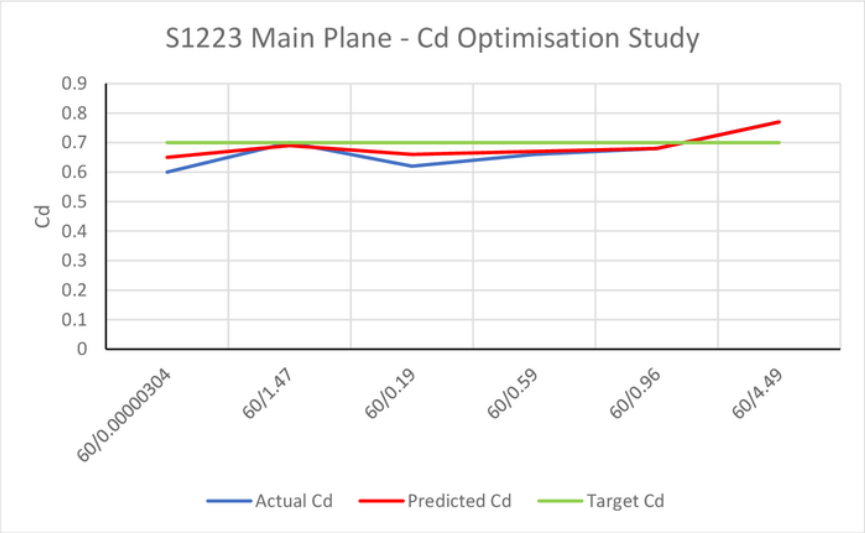
| Height (mm)/AoA (°) | Desirability |
|---|---|
| 60/0.00000304 | 0.85 |
| 60/1.47 | 0.848 |
| 60/0.19 | 0.847 |
| 60/0.59 | 0.842 |
| 60/0.96 | 0.841 |
| 60/4.49 | 0.799 |

*Table 9,* indicates the predicted heights and AoA that the DOE suggests, in order to achieve the target Cl and Cd, together with the calculated desirability factors, which are considered as a percentage of confidence within the predicted input variables. As can be observed, six formations are given which have a high desirability factor.



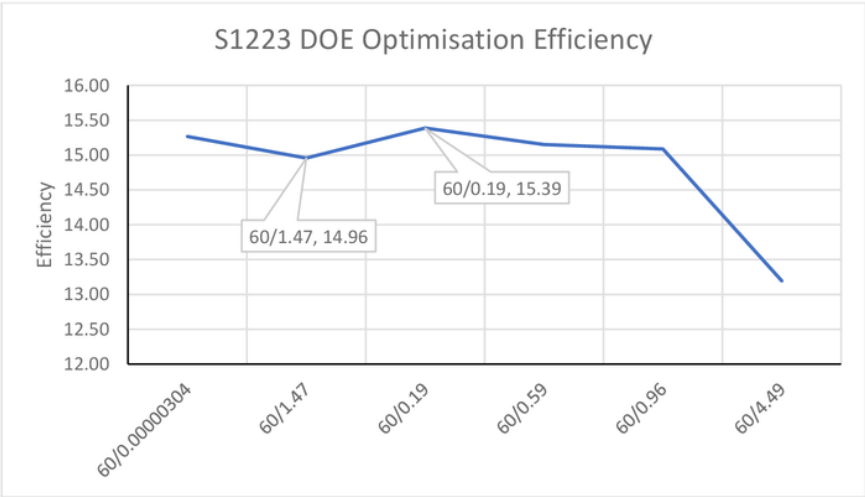

*Graph 22 - S1223 Main Plane - Cl Optimisation Study*

*Graph 22,* illustrates the resultant Cl produced as a result of the given profile arrangements. As can be observed, the actual Cl can be considered to be unstable when compared to the predicted Cl and target that were produced. This phenomenon could be as a result of the given heights. It could be considered that the target Cl may not have been achievable using a 60mm height, to then also achieve the target Cd value. This is as a result of possible inappropriate use and a lack of understanding of the software, however, this was not diagnosed until detailed analysis was conducted, suggesting that the height range had been over restricted and AoA left under restricted, whereas previous analysis suggests the restrictions should be reversed.




*Graph 23 - S1223 Main Plane - Cd Optimisation Study*

However, *Graph 23* displays that the actual Cd figures produced follow closely, the trends of the predicted and target Cd values. This suggests that within the working ranges provided, the Cd values are readily achievable compared to those of the Cl values, therefore, efficiency may still be achievable.




*Graph 24 – S1223 Main Plane – DOE Optimisation Efficiency*

As has been previously stated, efficiency must be considered in order to afford a greater workability when the wing is installed on the car, however, consideration must still be given to the achievable downforce so that frontal grip can be maintained.

*Graph 24,* illustrates the efficiencies achieved for each of the given profile arrangements. As can be observed, the arrangement of 60mm/0.19° provided the best efficiency, however, the arrangement also produced the second lowest Cl value, thus the 60mm/1.47° arrangement has been selected for implementation on the vehicle, due to its high -Cl and Cd being the same as the target Cd. This produces an efficiency of 14.96, which is 0.43 lower than the maximum, therefore, it is felt that a minor sacrifice in efficiency is worth the gain in overall downforce.

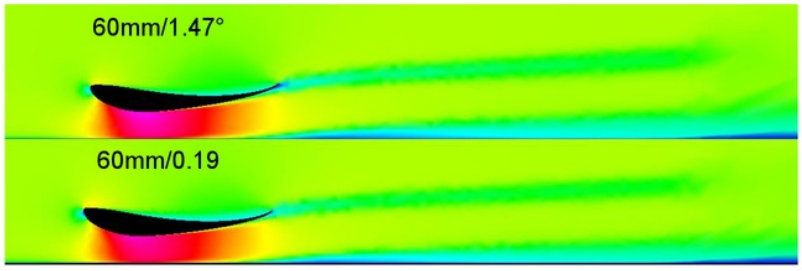



*Figure 55 - S1223 Main Plane DOE Optimisation Velocity Contours*

*Figure 55,* illustrates the velocity contours of both the 60mm/1.47° and 60mm/0.19° arrangements. As can be observed, there is very little distinguishable difference between the arrangements, however, there is a considerable difference in Cl produced by these arrangements.

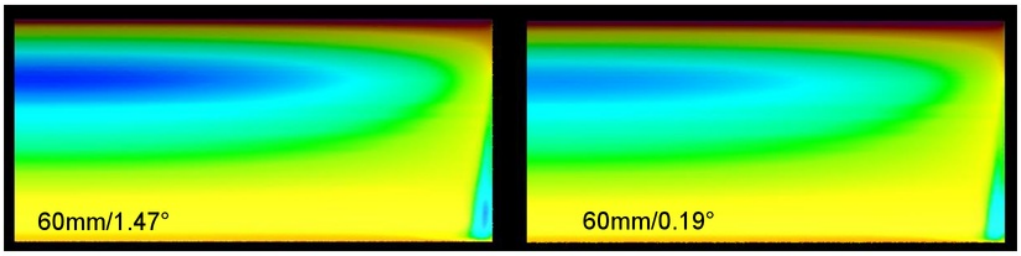
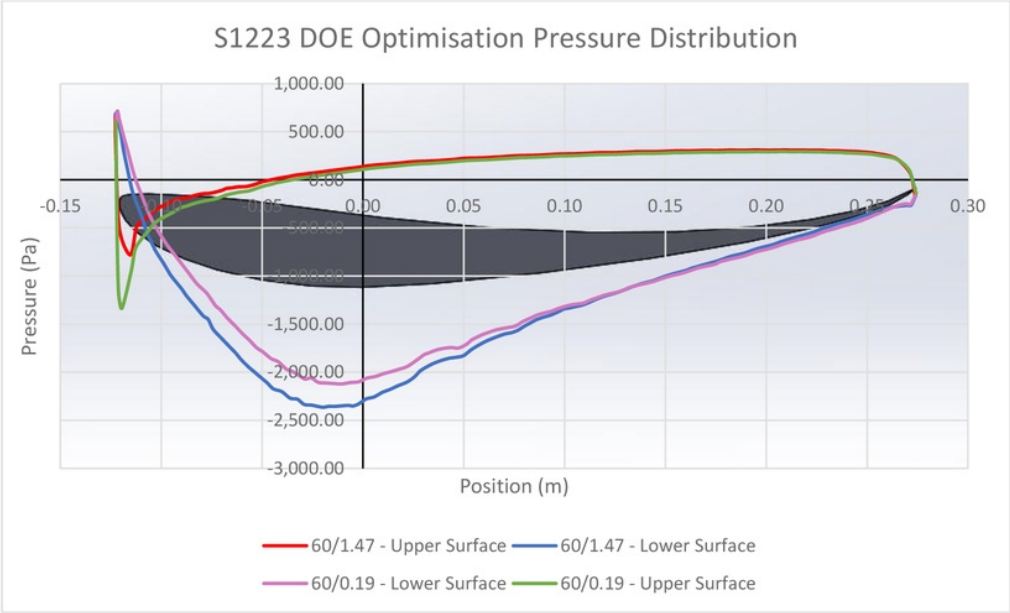



*Figure 56 - S1223 Main Plane DOE Optimisation Lower Surface Pressure Contours*

The pressure contours displayed in *Figure 56*, further illustrate how the increased AoA has altered the way in which the profile works, with a greater area having a lower negative pressure defined on the 60mm/1.47° arrangement. This is also evident in *Graph 25*, however, very little change is present on the upper surface with regard to positive pressure.




*Graph 25 - S1223 DOE Optimisation Pressure Distribution*

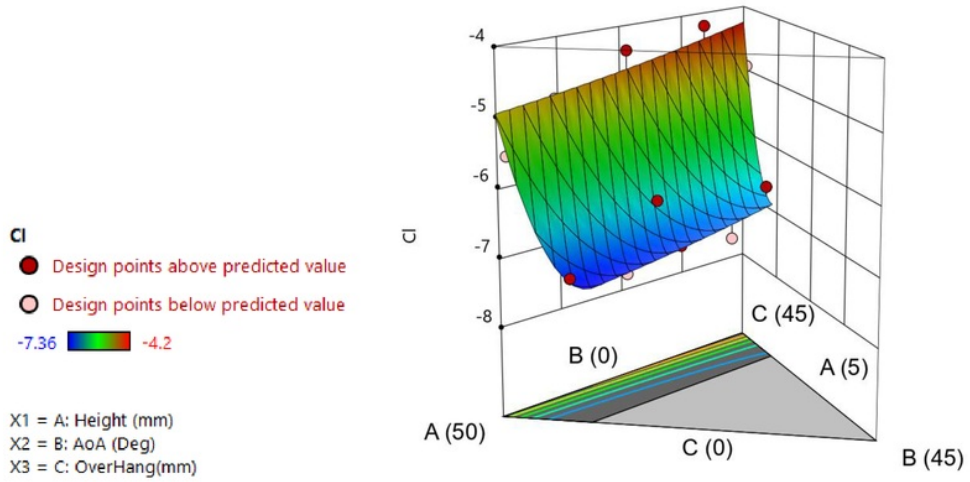
## 5.4.0 Secondary Element – Naca 4412: Height vs AoA vs Positive Overhang

The implementation of a secondary element carries with it the need to investigate a third variable of overhang. In this study, a positive overhang was examined (a secondary element leading edge protrusion over the trailing edge of the main plane). To validate a three input variable and two response study, a Box Behnken DOE study was employed. The Box Behnken is considered superior in terms of analysis and optimisation (Ferreira, et al., 2007).

Both the Naca 4412 and S1223 profiles were considered for the secondary element, subsequently, both profiles were subjected to further DOE analysis. It is important to note that the secondary element possesses the same dimensions as those used on the S1223 main plane.

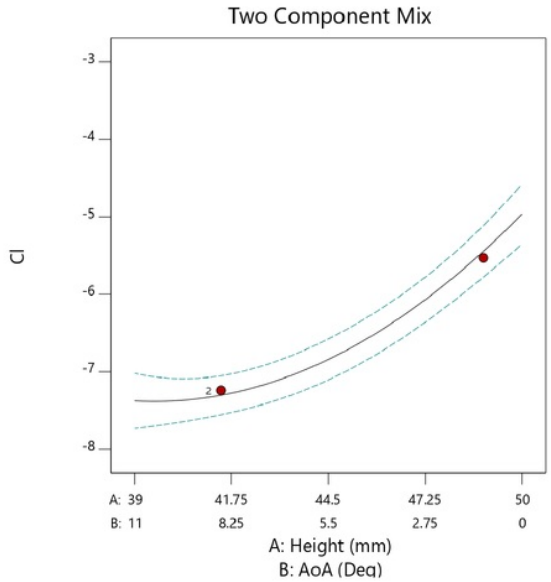
*Table 10 - Naca 4412 & S1223 Secondary Element Input Variables*

| Variable | Minimum | Maximum |
|---|---|---|
| Height (mm) | 5 | 50 |
| AoA (°) | 0 | 11 |
| Overhang (mm) | 0 | 45 |




*Graph 26 - Naca 4412 Secondary Element DOE Study (Cl)*

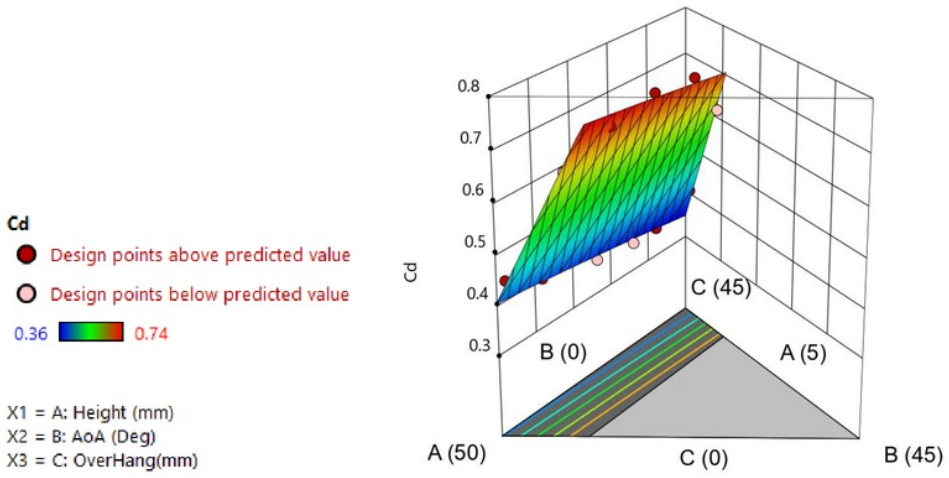
*Graph 26,* illustrates the interactions between the three considered variables in *Table 10,* regarding Cl. As the graph indicates, the positive overhang has a significant negative impact.




*Graph 27 - Naca 4412 Overhang Influence (Cl) (0mm Overhang)*

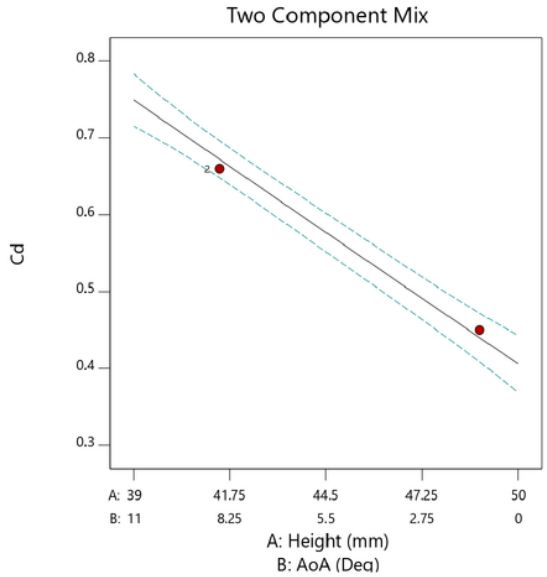
The above graph (*Graph* 27) illustrates the influence of overhang in a 2D format. The graph clearly indicates that if 0mm of overhang is present, decreasing the AoA has a negative influence on Cl, as does increasing the height above a 40mm threshold. However, if 45mm of overhang exists, altering the AoA and height has no bearing on the influence of Cl.

Further investigation reveals that regardless of height or overhang, an increase in AoA produces an increase in downforce. This results from the effective change in expansion area, which forces the main element to generate a greater pressure differential.




*Graph 28 - Naca 4412 Secondary Element DOE Study (Cd)*

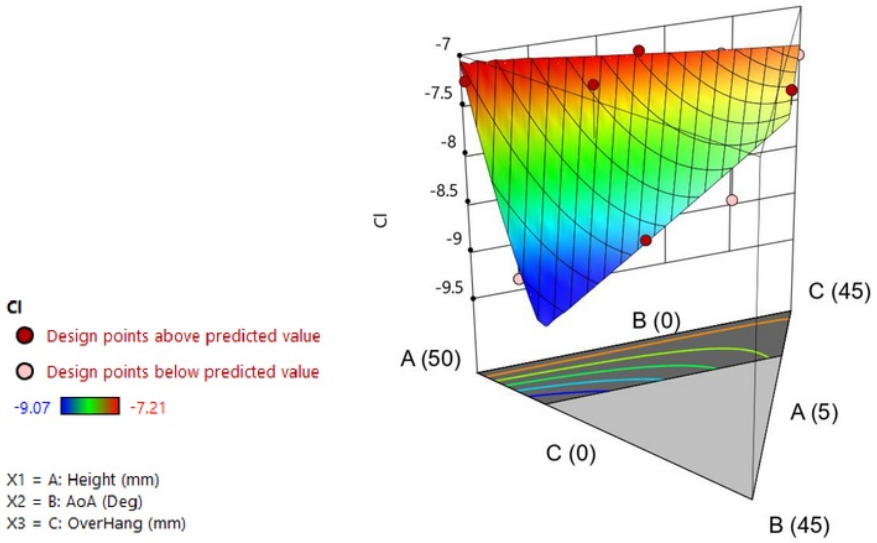
Positive overhang does, however, reduce the drag coefficient (*Graph 28*). This is because the effective planar area of the profile is reduced as the overhang is increased, therefore, a reduction in drag is to be expected.




*Graph 29 – Naca 4412 Overhang Influence (Cd) (0mm Overhang)*

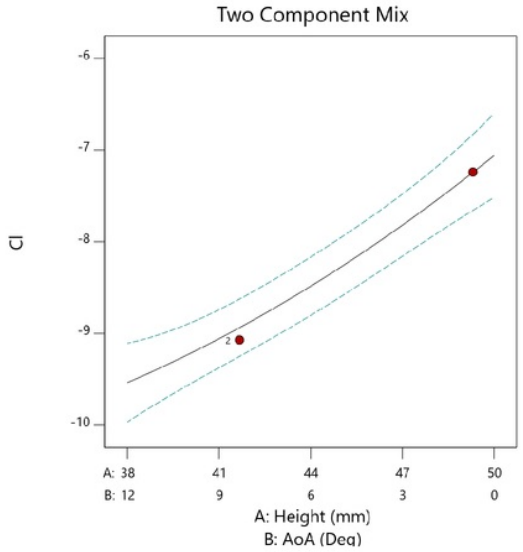
As the overhang is decreased, a reduction in Cd can be achieved by reducing the AoA, or by increasing the height above the main plane (*Graph 29*). It is inevitable, however, that as the secondary element drives the main plane to generate additional downforce, an additional amount of drag will also be produced. If the overhang is increased to the maximum distance of 45mm, however, altering the height or AoA has no impact, but does consistently produce low values of Cd.

## 5.5.0 Secondary Element – S1223: Height vs AoA vs Positive Overhang




*Graph 30 - S1223 Secondary Element DOE Study (CI)*

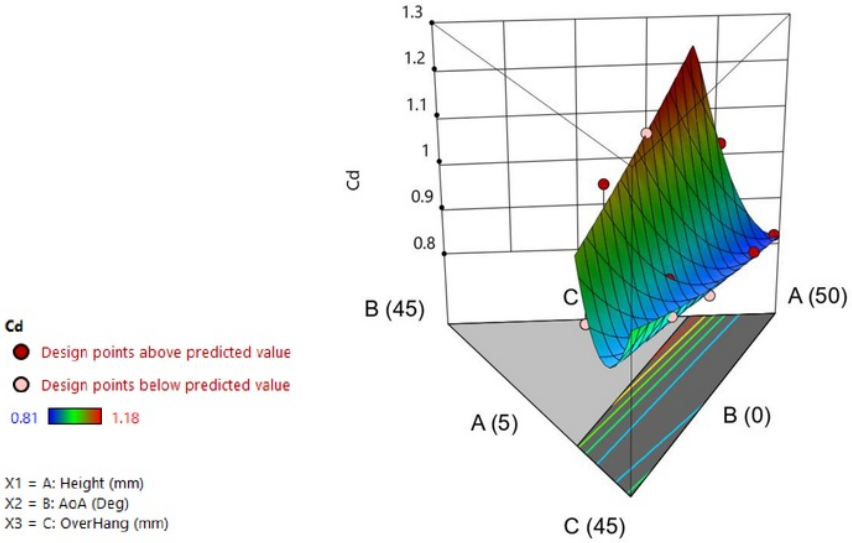
The same influences can be observed when employing an S1223 profile as the secondary element. As the positive overhang is decreased, the production of downforce is increased as a result of the increase in working area and created expansion.




*Graph 31 - S1223 Overhang Influence (CI) (0mm Overhang)*

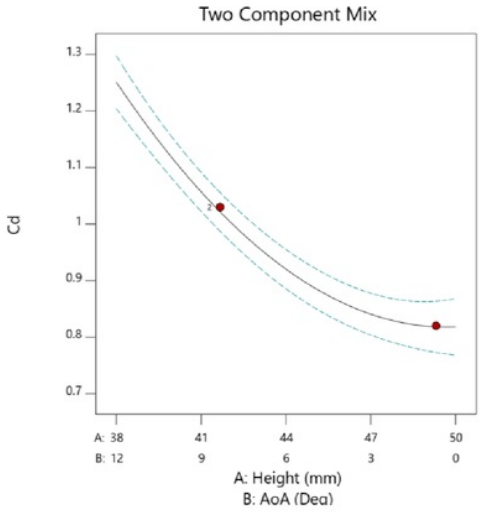
The generation of downforce has greater linearity using an S1223 secondary element when compared to that of a Naca 4412, however, when 0mm of overhang is present, the trends

between the two profiles remain consistent, but the overall downforce generated using the S1223 as the secondary element is higher, regardless of arrangement, although it is apparent that the overhang between the main plane and secondary element generates the greatest influence on Cl production.




*Graph 32 - S1223 Secondary Element DOE Study (Cd)*

A threshold of overhang is present where Cd remains relatively consistent, after which a dramatic increase occurs, however, low heights also play a contributory factor in this, as *Graph 32* illustrates.




*Graph 33 - S1223 Overhang Influence (Cd) (0mm Overhang)*

As has already been stated, together with an increase in downforce, the drag component will consequently increase. It remains, that if 0mm of overhang is used to generate the maximum downforce, increasing the height or reducing the AoA of the secondary element will not reduce the induced drag. However, this relationship does not have the same linearity as the Naca 4412 (*Graph 29*), although overall drag production is higher compared to that of the Naca 4412 secondary element.

5.5.1 Secondary Element Discussion

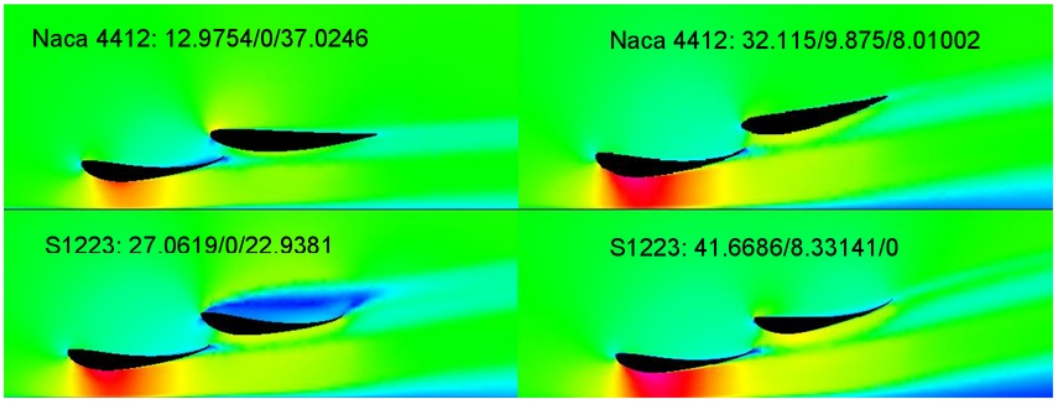
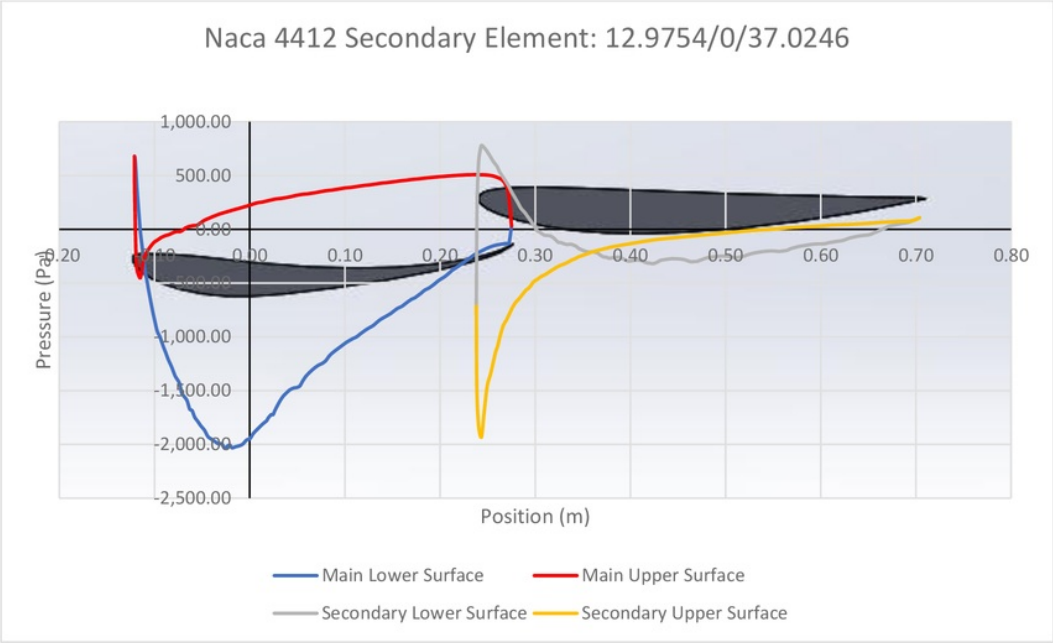


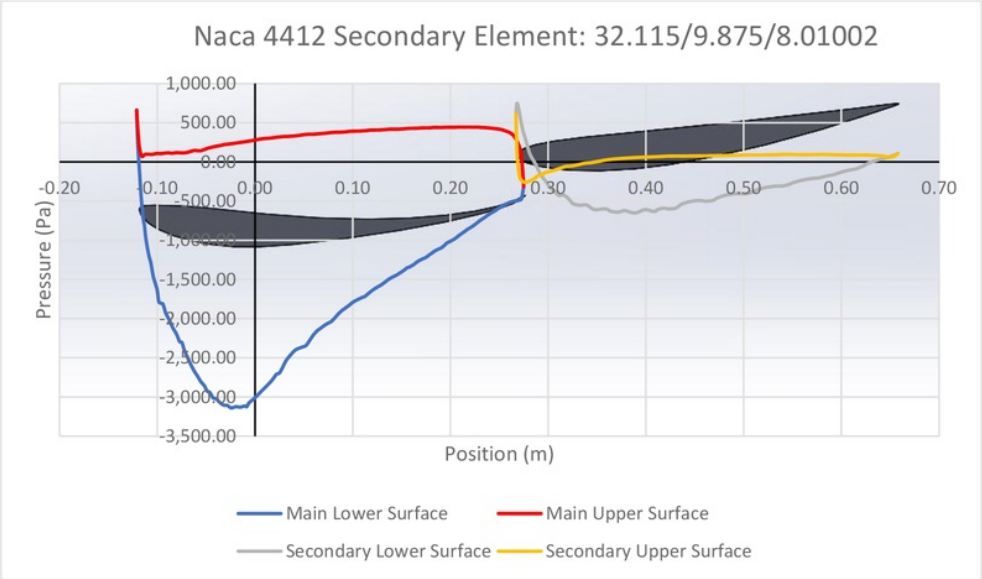

*Figure 57 - Naca 4412 & S1223 Minimum & Maximum Cl Velocity Contours*

The above figure (*Figure 57*) illustrates the velocity contours of four compound element arrangements derived from the DOE study discussed in chapters 5.4.0 and 5.5.0. Evidentially, both cases indicated on the right of *Figure 57* show an increase in Vmax on the lower surface of the main plane, thus increasing the Cl element in the arrangements.



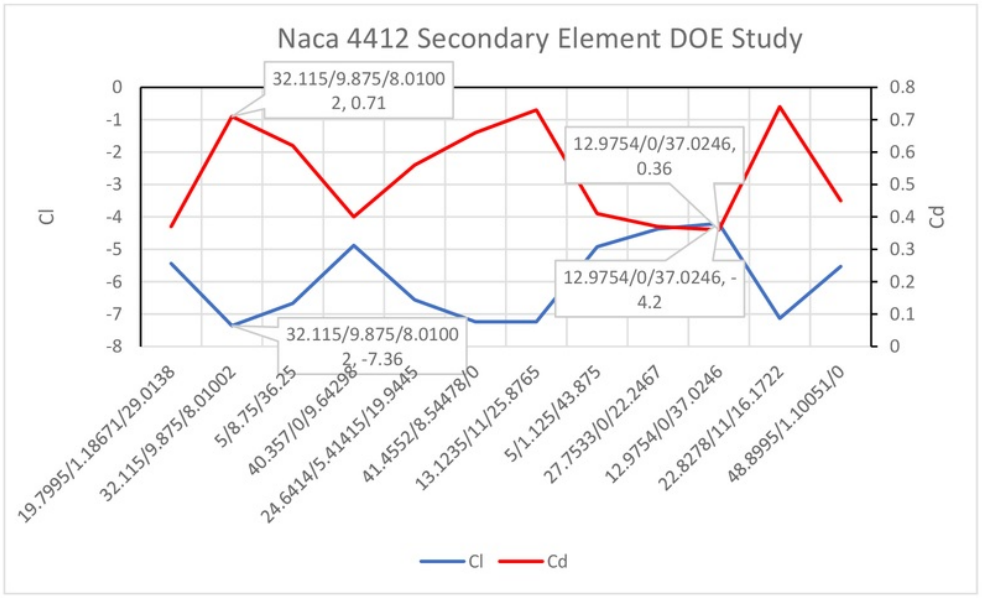

*Graph 34 - Naca 4412 Secondary Element Pressure Distribution (12.9754mm/0°/37.0246mm)*

The above arrangement illustrated in *Graph 34,* proves to be a hindrance rather than a gain. The secondary element appears to be creating a blockage to the upwash generated by the main plane. This is affecting the mass flow beneath the main plane, establishing a drop in the maximum negative pressure compared to that indicated in *Graph 25*. However, the maximum positive pressure has gain, although the offset has generated a lower pressure differential.




*Graph 35 - Naca 4412 Secondary Element Pressure Distribution (32.115mm/9.875°/8.01002mm)*

Increasing the AoA and decreasing the overhang has clearly had a positive effect on the pressure distributions, producing less of a blockage, resulting in greater pressure differentials being achieved on both the main plane and secondary element, allowing the boundary layer to remain on a constant vector and producing a greater expansion area.



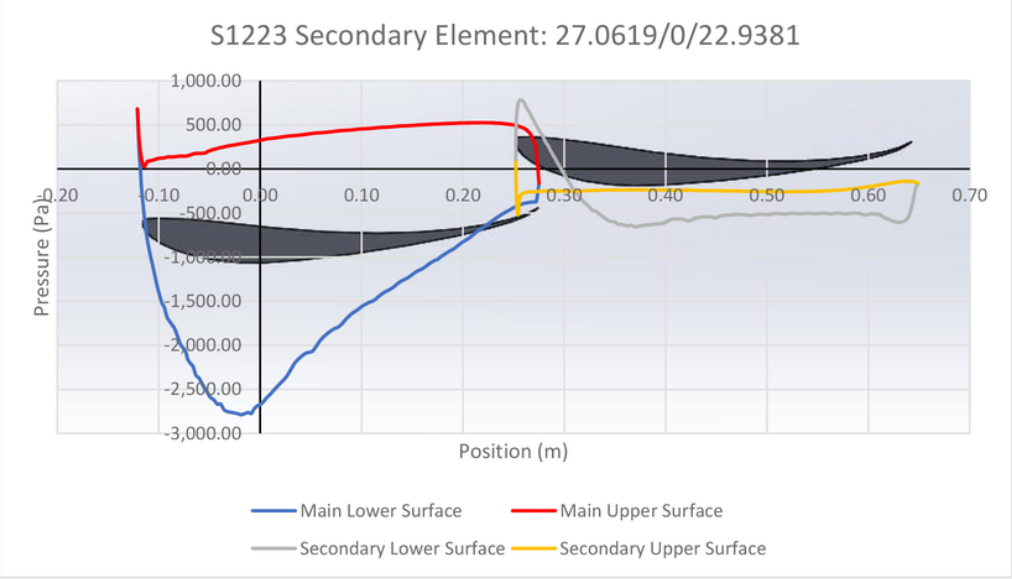

*Graph 36 - Naca 4412 Secondary Element DOE Study (Cl & Cd)*

As has been previously discussed, a component of increasing downforce is an increase in drag force. This trait can be observed in *Graph 36*, which outlines the Naca 4412 secondary element arrangements produced in the previous DOE study. Both arrangements producing the maximum and minimum Cl are highlighted, along with the subsequent Cd values.

*Table 11 - Naca 4412 Secondary Element Arrangements & Efficiencies*

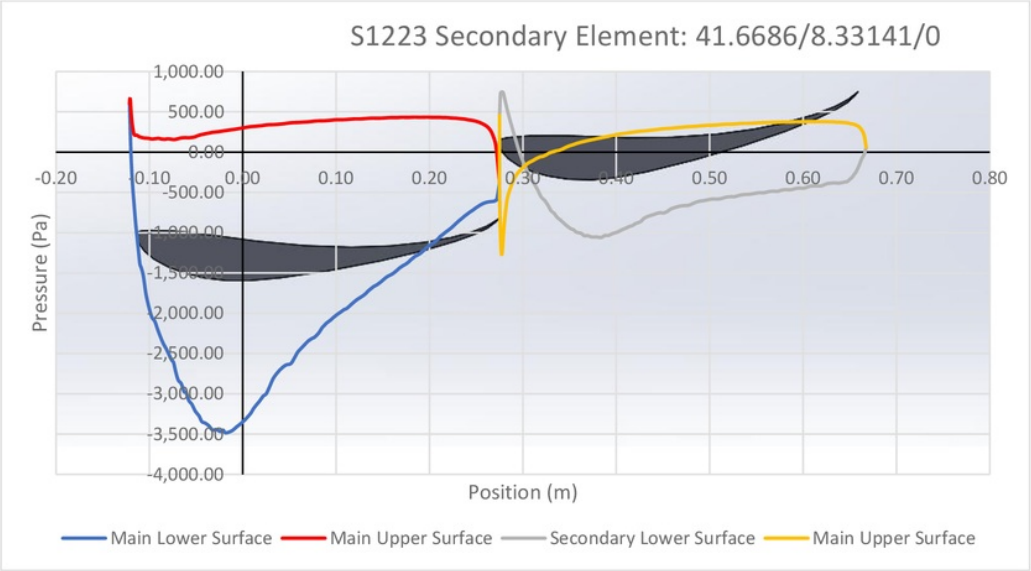
| Arrangement | Efficiency |
|---|---|
| 32.115/9.875/8.01002 | 10.37 |
| 12.9754/0/37.0246 | 11.67 |

Although downforce generation is a major factor, efficiency of the arrangement needs to be considered. However, as *Table 11* suggests, to maintain a large gain in downforce, only a 1.3 comprise in efficiency is made.



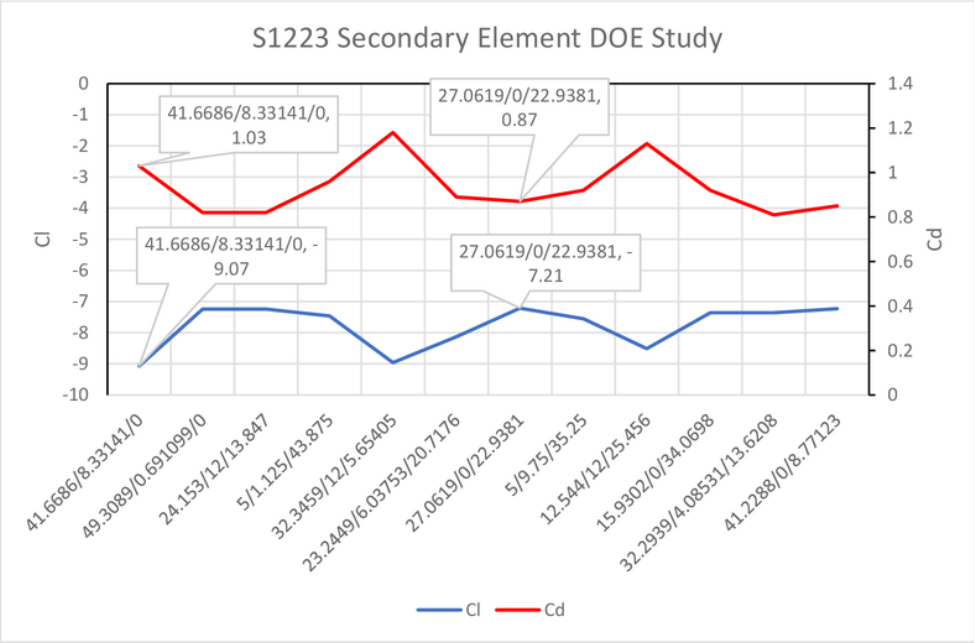

*Graph 37 – S1223 Secondary Element Pressure Distribution (27.0619mm/0°/22.9381mm)*

Using the S1223 profile as the secondary element has a greater impact on the production of downforce, as the main element now has a maximum negative pressure of in excess of -2500Pa (*Graph 37*). This is an increase in over 500Pa from the arrangement illustrated in *Graph 34.* However, the secondary element has been compromised due to the concave upper surface and the raised leading edge. This is creating an area of sudden separation, as indicated in *Figure 57*, which is restricting the surface pressure, so that it remains below atmospheric pressure.




*Graph 38 – S1223 Secondary Element Pressure Distribution (41.6686mm/8.33141°/0mm)*

Once more, increasing the AoA and decreasing the overhang has had a positive influence on the main plane, which is now generating a maximum negative pressure of -3500Pa, and allowing the secondary element pressure differential to increase *(Graph 38)*. The increase in AoA also allows a smoother return to atmospheric pressure to be achieved on the lower surface, which provides greater downforce. However, the arrangement displays a sharper gradient in negative pressure along the main plane lower surface, compared to that of the previous profile arrangements.




*Graph 39 – S1223 Secondary Element DOE Study (Cl & Cd)*

*Graph 39,* illustrates the same following trends as can be observed in *Graph 36*, and displays a consistent increase in both Cl and Cd production. Again, both arrangements producing the maximum and minimum Cl are highlighted, and unlike the efficiencies indicated in *Table 11*, the S1223 secondary element produces a greater efficiency with the greater Cl arrangement (*Table 12*), though are still considerably lower than that produced using a Naca 4412 secondary element.

*Table 12 - S1223 Secondary Element Arrangements & Efficiencies*

| Arrangement | Efficiency |
|---|---|
| 41.6686/8.33141/0 | 8.81 |
| 27.0619/0/22.9381 | 8.29 |

5.5.2 S1223 Secondary Element DOE (Height vs Chord Length vs Increased AoA)

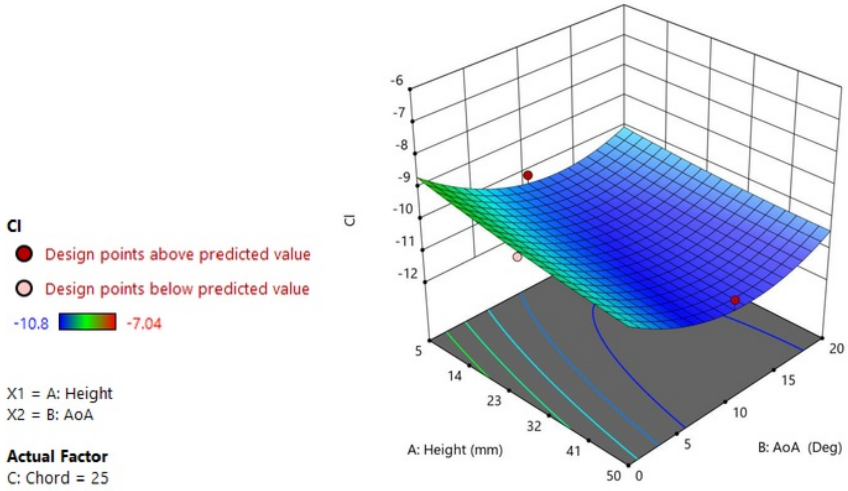
Previous studies investigated two different profiles at differing heights, AoA and positive overhangs, therefore a further DOE study of secondary element chord length can now be carried out. This will include combining a greater increase in AoA, but without any overhang, as the previous studies show that positive overhang creates a greater hindrance to profile performance than to any perceived gain.

From the previous investigation, the S1223 was chosen for inclusion as the secondary element, based on its powerful production of pressure differentials. However, this decision was made without regard to efficiency, or the consequences of its implementation on the car.

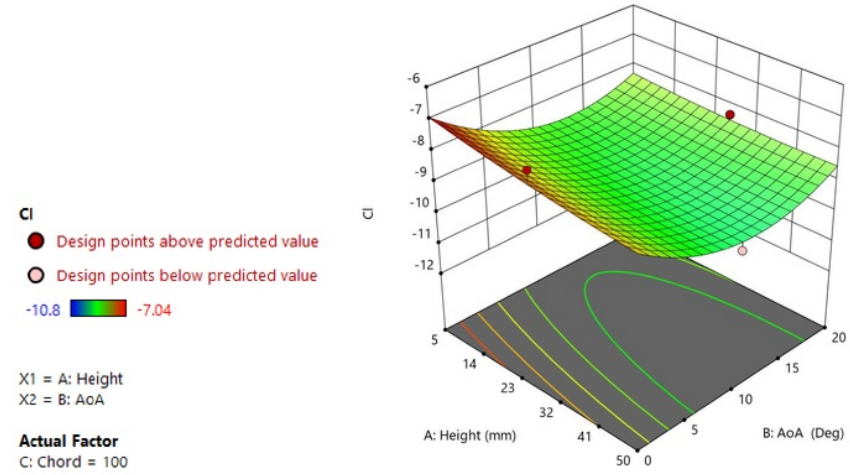
*Table 13 - S1223 Secondary Element Input Variables*

| Variable | Minimum | Maximum |
|---|---|---|
| Height (mm) | 5 | 50 |
| AoA (°) | 0 | 20 |
| Chord (%) | 25 | 100 |

In *Table 13*, the secondary element chord length is measured as a percentage scale of the main plane chord, and AoA is increased from 11° to 20°.

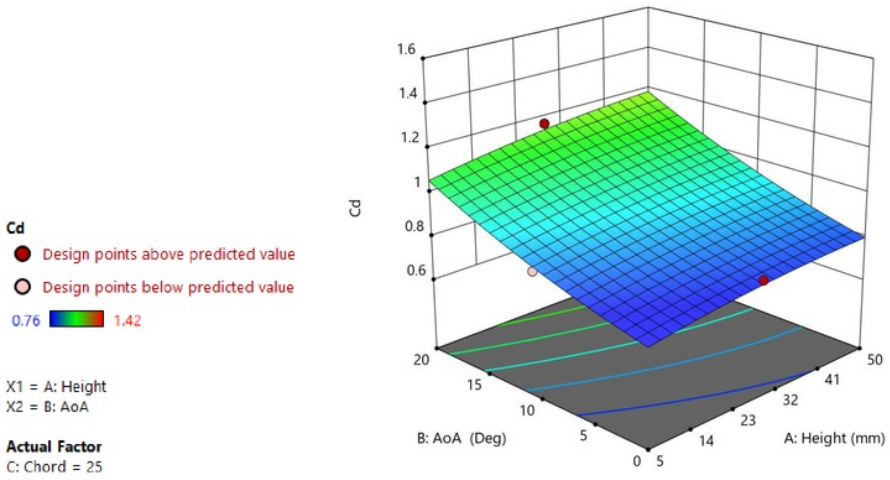



*Graph 40 - S1223 Secondary Element DOE Study 2 (Cl) (25% Chord)*



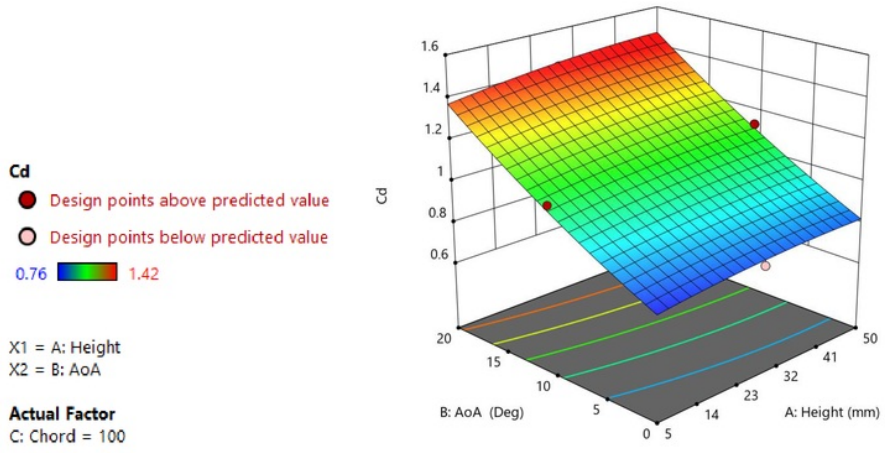

*Graph 41 - S1223 Secondary Element DOE Study 2 (Cl) (100% Chord)*

Comparing *Graphs 40* and *41,* a linear decrease in Cl from 25% to 100% chord length is indicated, this, therefore suggests that a lesser chord length is optimum for downforce production on the secondary element, which is unexpected, as the total planar area is reduced.




*Graph 42 - S1223 Secondary Element DOE Study 2 (Cd) (25% Chord)*

As was anticipated, a reduction in chord length produces a reduction in Cd, although no difference in Cd became apparent at 0° AoA, which therefore suggests that chord length has a significant impact upon the drag coefficient at any AoA above 0°.




*Graph 43 - S1223 Secondary Element DOE Study 2 (Cl) (100% Chord)*

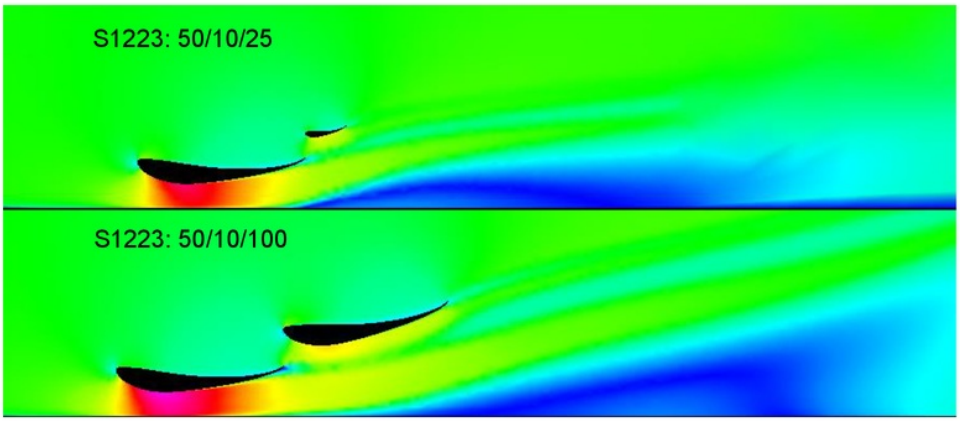
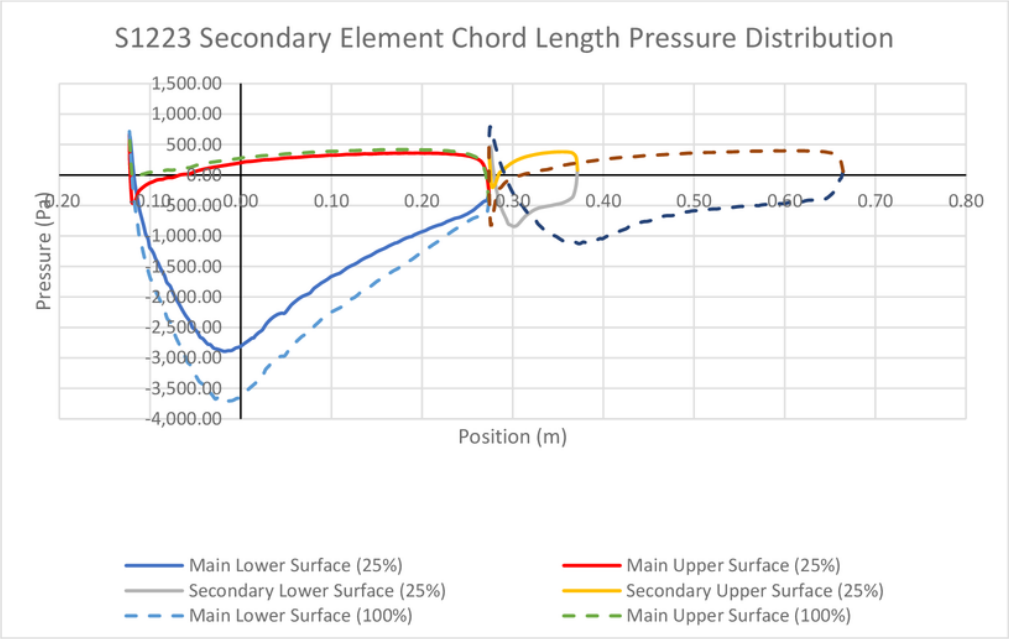



*Figure 58 - S1223 Secondary Element Chord DOE Study Velocity Contours*

As a reference, *Figure 58* illustrates the same profiles, with the only difference being the chord length percentage of the secondary element.

The velocity contours display an increase in velocity when using a secondary element of the same dimensions as the main plane, which therefore suggests a further negative pressure increase.




*Graph 44 - S1223 Secondary Element Chord Length Pressure Distribution*

This phenomenon is represented in *Graph 44*, which suggests that using a larger chord length on the secondary element produces a greater pressure differential on the main plane, however, the Cl produced is reduced compared to that produced by a smaller chord length.

*Table 14 - Chord Length Comparison*

| Height (mm)/AoA (°)/Chord (%) | DRAG (N) | DOWNFORCE (N) | DOWNFORCE (KG) | EFFICIENCY | Drag Cd | Lift Cl |
|---|---|---|---|---|---|---|
| 50/10/25 | 300.89 | 3494.18 | 356.2 | 11.61 | 0.93 | -10.8 |
| 50/10/100 | 589.43 | 4971.01 | 506.7 | 8.43 | 1.13 | -9.53 |

*Table 14,* indicates the downforce produced and the drag values from both of the discussed arrangements. As downforce and drag are relative to the planar area of the object concerned, it is expected that by using a larger secondary element, it should produce additional downforce and drag force. It is also noticeable, however, that despite producing more force, the efficiency of the element is also reduced when compared to that of a smaller secondary element, which results from the large increase in drag force.

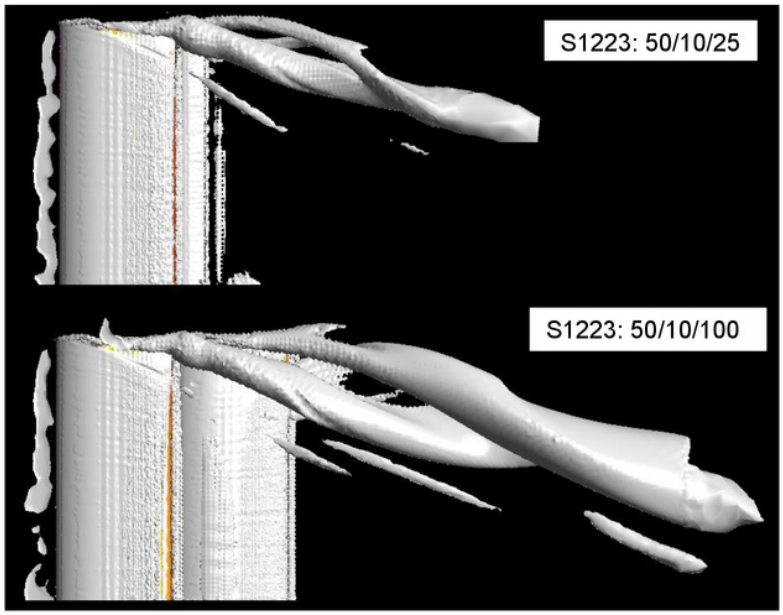



*Figure 59 - Chord Length Study Vortex Generation*

As the profile arrangements are simulated in isolation without the presence of end plates, a much larger vortex generation is apparent when using a larger secondary element (*Figure 59*), as a result of the increase in the pressure gradient between the upper and lower surfaces (*Graph 44*), producing much more induced drag, which could be resolved by the introduction of end plates.

### 5.5.3 S1223 Secondary Element Optimisation Study

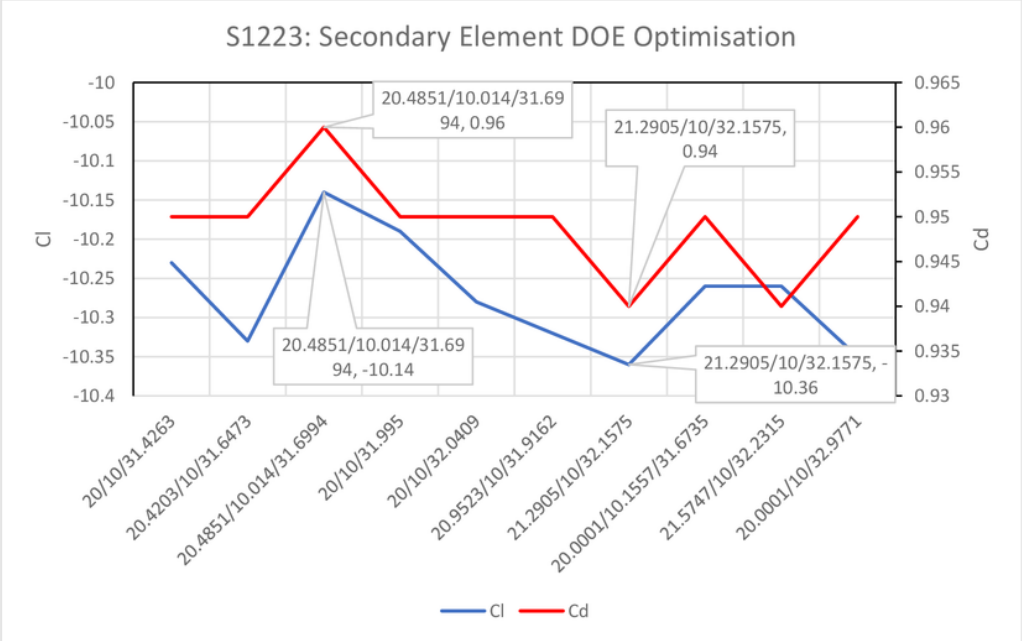
As positive overhang had been found to produce a negative impact upon the results, it was decided that for the purposes of this optimisation, it would remain set at 0mm (neutral).

A Cl target of -10.5 and Cd target of 0.9 was set, with the purpose of aiming for an efficiency of 11.67.

*Table 15 - S1223 Secondary Element DOE Optimisation Desirability*

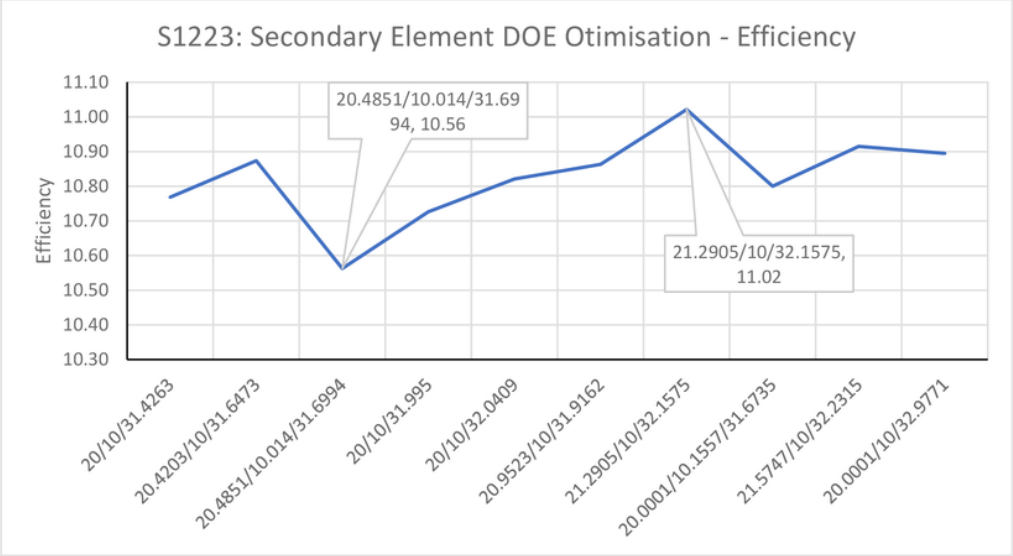
| Height (mm)/AoA (°)/ Chord (%) | Desirability |
|---|---|
| 20/10/31.4263 | 0.957 |
| 20.4203/10/31.6473 | 0.953 |
| 20.4851/10.014/31.6994 | 0.952 |
| 20/10/31.995 | 0.952 |
| 20/10/32.0409 | 0.951 |
| 20.9523/10/31.9162 | 0.949 |
| 21.2905/10/32.1575 | 0.946 |
| 20.0001/10.1557/31.6735 | 0.945 |
| 21.5747/10/32.2315 | 0.944 |
| 20.0001/10/32.9771 | 0.943 |

*Table 15,* indicates the confidence in which the DOE software has in being able to reach the stated coefficient targets with its predicted profile arrangements. It could be assumed, however, that each arrangement would only produce very minor differences due to the considerable similarities the software has produced within each recommended arrangement.



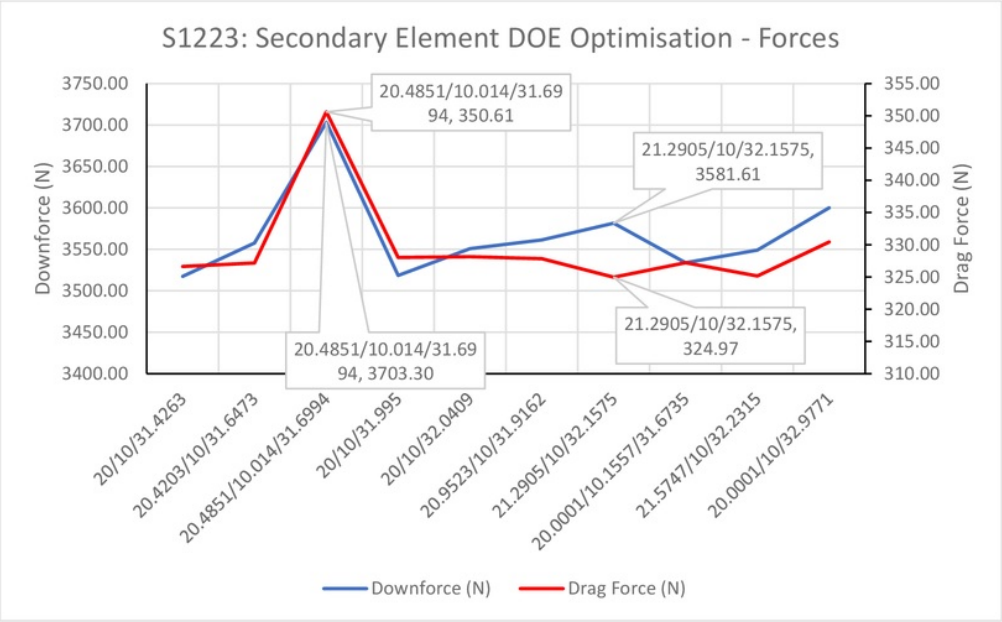

*Graph 45 - S1223: Secondary Element DOE Optimisation (Cl & Cd)*

*Graph 45,* indicates the coefficient figures, with only small differences becoming apparent within the Cl and Cd results.




*Graph 46 – S1223: Secondary Element DOE Optimisation (Efficiency)*

Observing *Graphs 45, 46* and *47*, a number of interesting trends can be observed. Despite generating the greatest downforce, the arrangement of 20.4851mm height, 10.014° AoA and 31.6994% chord length, also produces the lowest coefficients of any of the current profile layouts, although all other variables remain identical. The aerodynamic efficiency produced is the lowest of all ten optimisation designs, however, the downforce and drag force are the highest of any.




*Graph 47 - S1223: Secondary Element DOE Optimisation (Forces)*

However, the profile arrangement producing the highest coefficient of lift and the second lowest coefficient of drag generates the optimal aerodynamic efficiency of 11.02, with the third highest production of downforce and the lowest drag force, as highlighted in *Graphs 45, 46* and *47*.

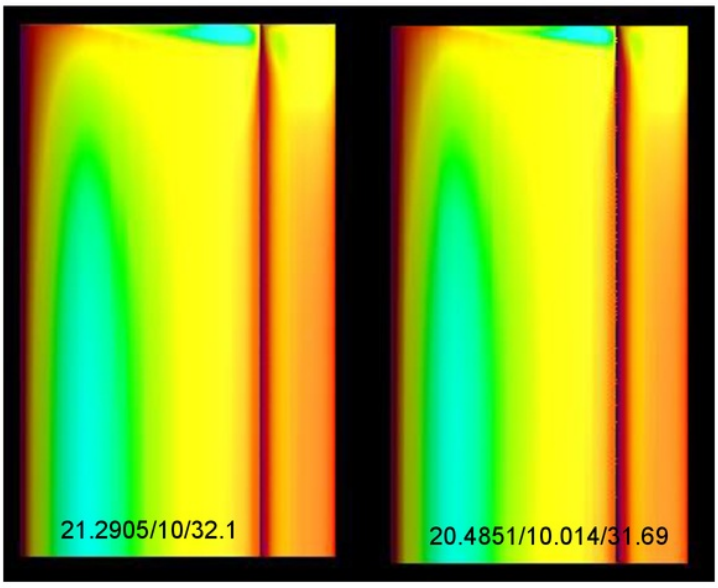



*Figure 60 - S1223: Secondary Element DOE Optimisation (Lower Surface Pressure Contours)*

Observing the surface pressure contours (*Figure 60*) leaves little to be distinguished between both profile arrangements, however, a minor increase in area of the negative pressure region on the main plane is apparent.

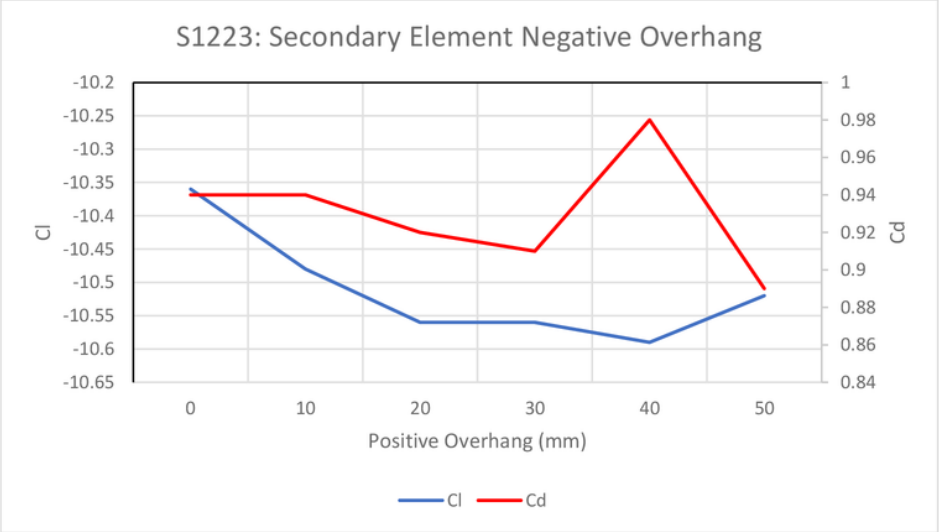
The results obtained are unusual. As has been previously stated, it can be expected that an object can produce low coefficients of both lift and drag. The area of the object denotes the total lift and drag force produced if all other variables remain consistent. In this case, however, the arrangement producing the highest downforce and drag force has a smaller planar area than that of the profile arrangement producing the greatest efficiency with lower downforce and drag force. It may, therefore, be that inconsistencies are present within the testing formulation, even though, each simulation is considered complete when full convergence of coefficients and flow residuals has occurred. However, this issue was only identified once further analysis had been conducted, and was therefore neglected during the investigation.

From the results obtained, the profile layout producing the greatest efficiency was chosen to be carried forward into the remaining investigations.

### 5.5.4 S1223 Secondary Element Negative Overhang Study

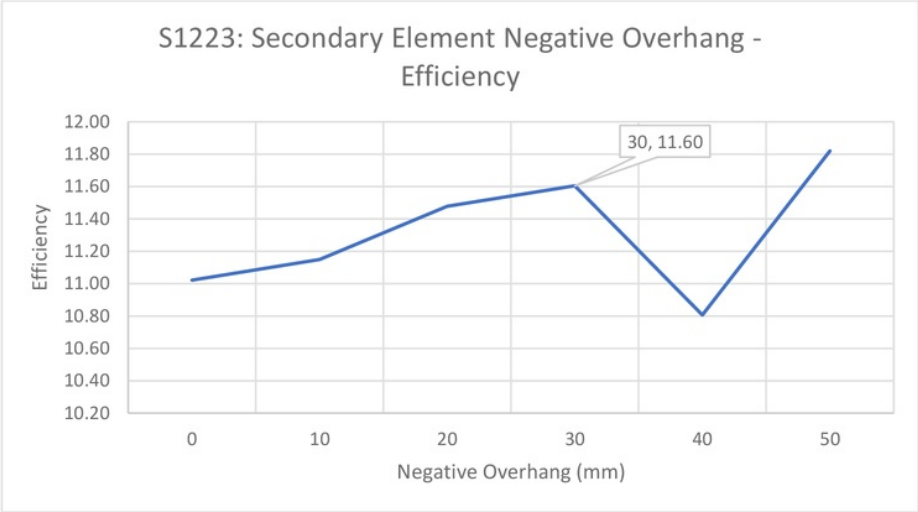
After further consideration of the issue it became apparent that a negative overhang study should be conducted using the profile layout outlined in chapter 5.5.3, that included an overhang of 0mm.

All other parameters were maintained, however, the secondary profile was moved rearward ($x$ direction) in increments of 10mm.




*Graph 48 - S1223: Secondary Element Negative Overhang (Cl & Cd)*

As the secondary element is moved rearward, each increment yields a compound rise in Cl, until a threshold of 40mm is reached. An anomaly is observed, whereby a sudden decrease (of 0.2) in Cd value is produced at the 40mm threshold, which then returns to a consistent value at 50mm. This is then represented within the aerodynamic efficiency, displayed in *Graph 49*. To produce such a sharp gradient change would suggest an issue within the CFD solving case, however, this detail was missed in the initial stages of the study. It is recommended that this study is simulated again and checked for result consistency.




*Graph 49 - S1223: Secondary Element Negative Overhang (Efficiency)*

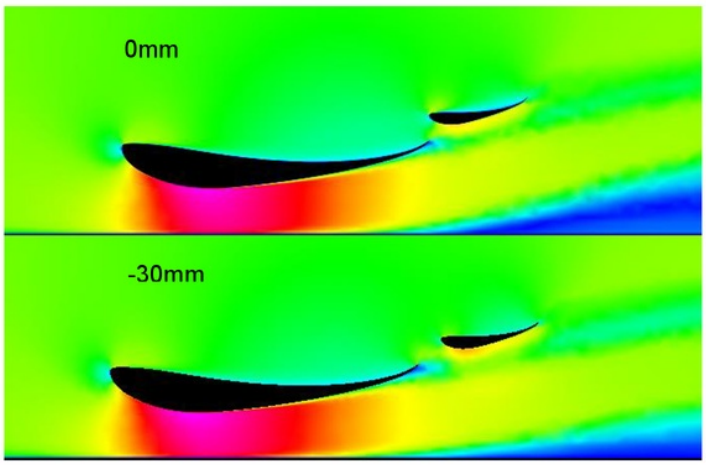



*Figure 61 - Secondary Element Negative Overhang (0mm & 30mm) (Velocity Contours)*

A 30mm negative overhang produces a suitable balance between Cl, Cd and efficiency, however, this result is questionable due the abnormal results observed in *Graph 48*.

The constant increase in downforce as the distance between the main plane and secondary element is enlarged could be pin-pointed to a blockage effect. As the S1223 has an aggressive camber, the frontal area would begin to restrict the fluid flow between the main plane upper surface and secondary element lower surface. An increase in air velocity can be observed on the lower surface of the secondary element when at a distance of 30mm compared to that at 0mm, as a result of less blockage. This then increases the air velocity under the main plane, therefore producing a larger differential in surface pressures.

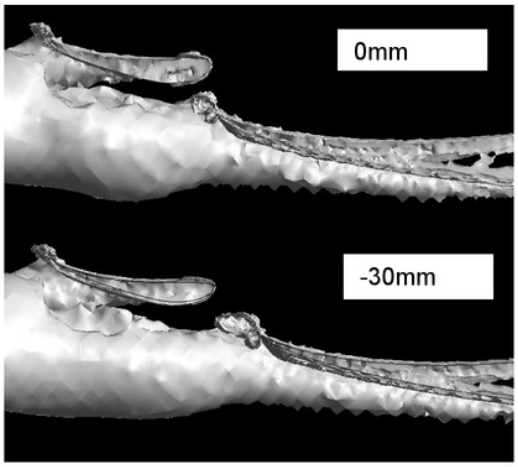



*Figure 62 - Trailing Edge Vortex*

As has been previously discussed, when a lateral vortex is developed on the trailing edge of the main plane, this helps re-energise the boundary layer, and increase air velocity. It can, however, become a flow restriction, resulting in a reduction in negative pressure and compounding into a lower Cl value.

*Figure 62,* illustrates the potential restriction caused by the trailing edge vortex. The smaller the mass volume of air that can travel results in a lesser energy value that can be transported, therefore, the compound wing does not work at its potential optimum.

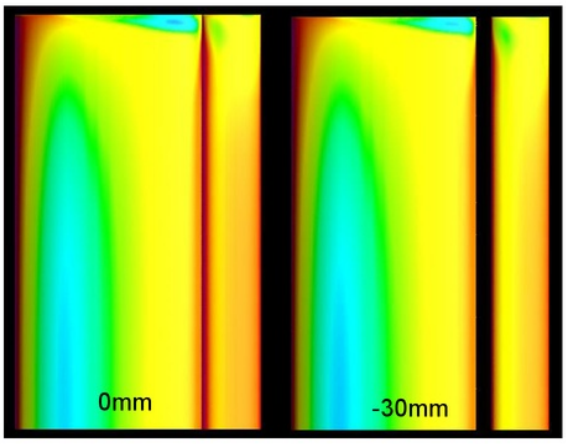
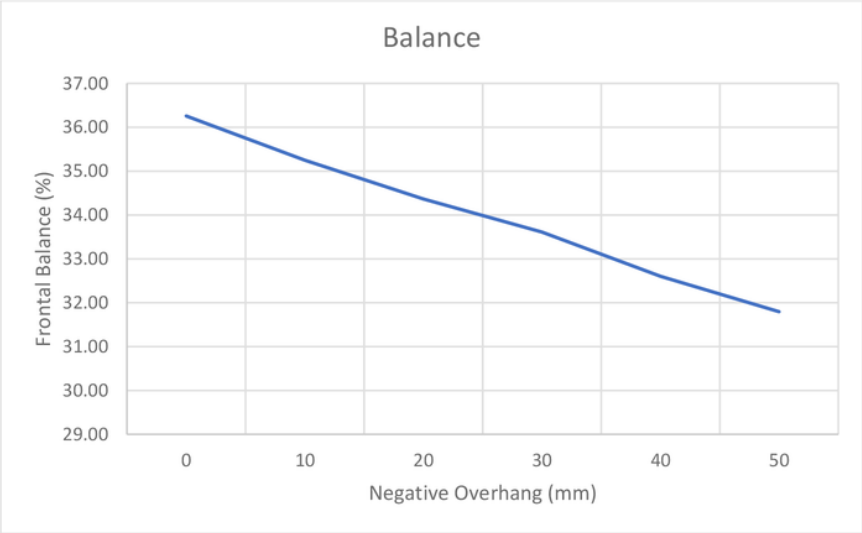



*Figure 63 - Secondary Element Overhang (0mm - 30mm) (Lower Surface Pressure Contours)*

Increasing the distance between main plane and secondary element, however, allows a greater fluid flow in the slot gap, resulting in the secondary element to having to work harder, which then influences the main element into working harder. This then results in an increase in negative pressure on the lower surfaces of both the main plane and secondary elements

(which can be observed in *Figure 63*), with a larger distribution of peak negative pressure on the main plane. It is also evident that together with an increase in overhang distance, the negative pressure observed on the main plane edge experiences a decrease in peak pressure resulting from the edge vortex that builds becoming restricted and unable to keep building in intensity due to the gap between the elements.




*Graph 50 - Frontal Balance (%)*

Increasing the negative overhang distance also results in the relocation of the Cp being moved rearwards. *Graph 50,* illustrates how the balance of the wing becomes increasingly rearward biased as the overhang is increased. This could then affect the overall Cp balance of the car when the compound wing is implemented.

## 5.6.0 Isolation Comparison (New Wing vs Baseline Splitter)

*Table 16 - Baseline Splitter & New Concept Aerodynamic Specification*

| | DRAG (N) | DOWNFORCE (N) | DOWNFORCE (KG) | EFFICIENCY | Cd | Cl |
|---|---|---|---|---|---|---|
| JHTT02 BASELINE SPLITTER (40mm HEIGHT) | 310.78 | 3999.76 | 407.7 | 12.87 | 0.77 | -9.91 |
| New Concept | 315.20 | 3657.66 | 372.9 | 11.60 | 0.91 | -10.56 |

A comparison study between the baseline splitter and concept wing was conducted in order to measure any gain in performance. Completing this study in isolation (without the car) saved time and would still provide a general understanding of the measure of performance of the concept, when compared to that of the baseline. Though it must also be highlighted that the new concept was simulated at a height of 60mm, whereas the baseline splitter was tested using its original height of 40mm.

*Table 16,* indicates that a significant gain in Cl has been achieved, however, it has be achieved to the detriment of efficiency, as the gain in lift is smaller than the gain in Cd.

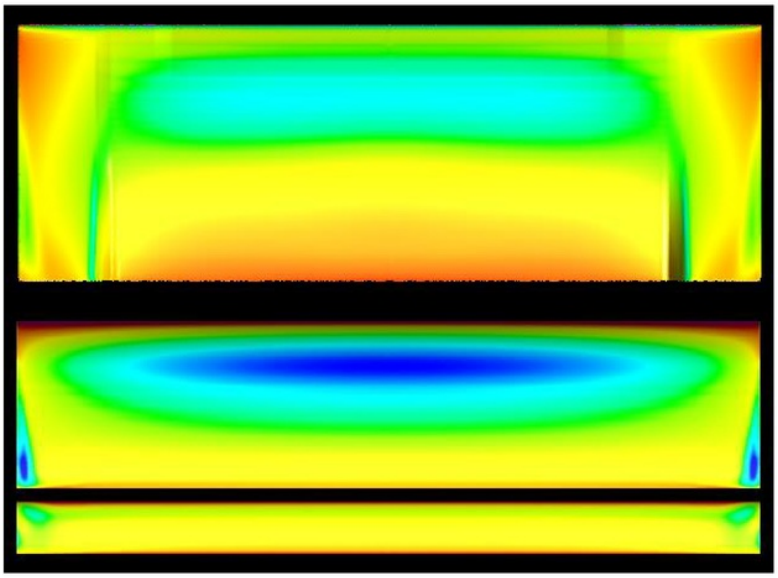


*Figure 64 - Baseline Splitter vs New Concept (Lower Surface Pressure Contours)*

The total chord length of the new concept (both profiles) is also smaller than that of the baseline, therefore a smaller aspect ratio can only be achieved, resulting in a considerable loss in the downforce produced, however, the gain in Cd has increased the drag by 5N.

Pressure contours (*Figure* 64) show that a greater peak negative pressure is achieved, however, it is contained in a very concentrated area, which may result in dynamic performance irregularities when applied to the car. Although the new concept does perform favourably in terms of allowing less high pressure bleed rolling around the edges of the wing.

High concentrations of low pressure can be observed on the edges at the rear of the main plane, which would suggest that powerful vortices have formed. A similar trait is visible on the baseline splitter, however, of a lesser intensity.

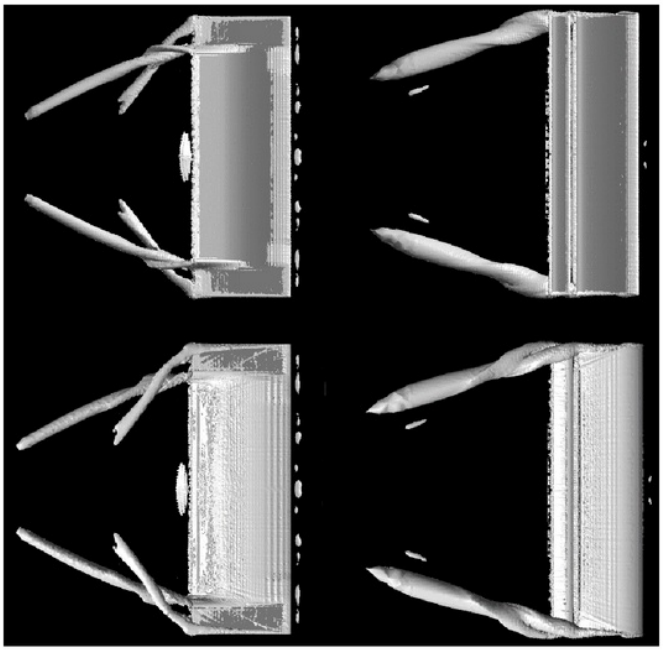


*Figure 65 - Baseline Splitter vs New Concept Vortices*

Both splitter concepts generate vortices that navigate in an inward trajectory, although the baseline splitter produces four smaller vortices. Examination of *Figure 65* reveals that the new concept also generates four vortices, which combine into two much larger vortices due to the location of each generating vortex. This would then create a greater amount of induced drag, therefore, substantially increasing the Cd value.

Improvement of the rolling lateral vortices on the lower surface of the new concept would suggest that considerably more energy is being generated in order to maintain the developed boundary layer, providing superior flow attachment.

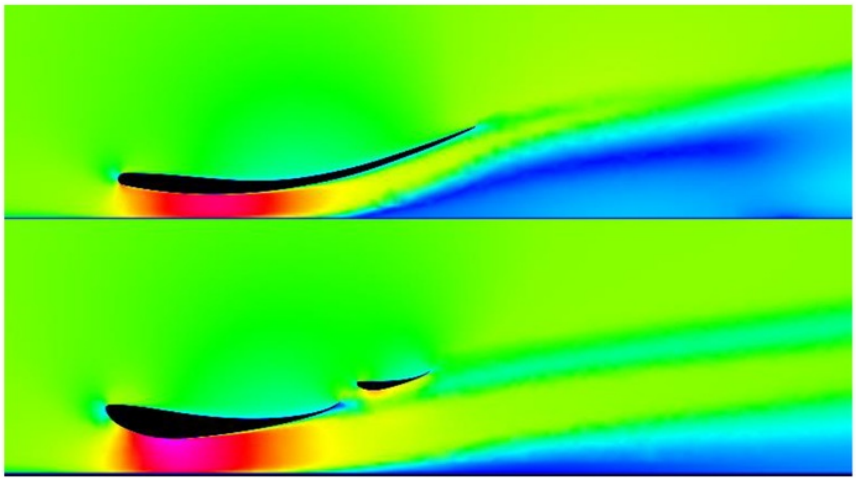
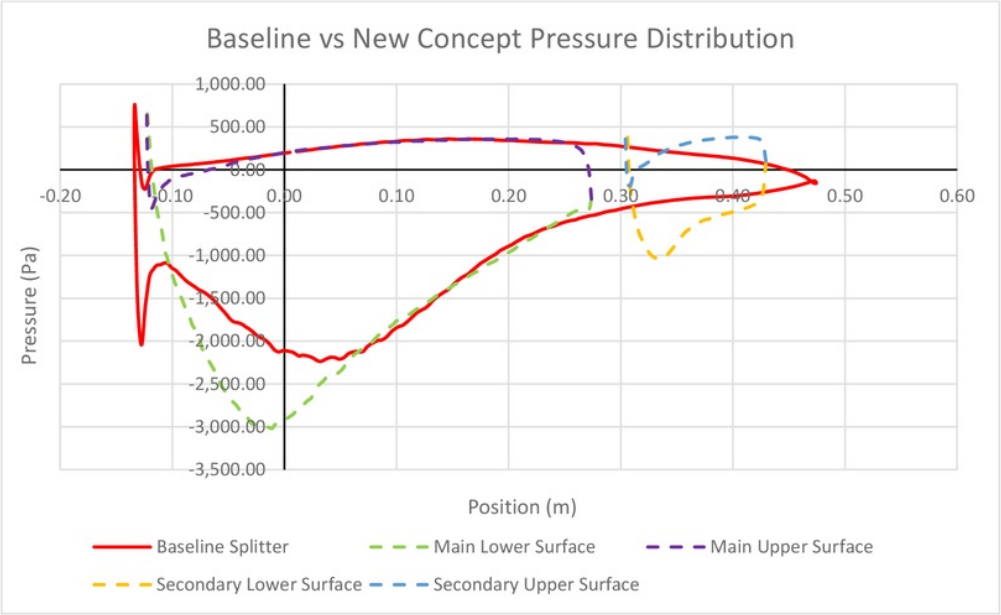


*Figure 66 - Baseline Splitter vs New Concept (Velocity Contours)*

The baseline splitter generates a greater amount of upwash, although this results in a larger rear wake region. However, the new concept allows a greater amount of higher velocity air to pass along its chord length, generating a smaller wake, which could then prove beneficial when implemented on the car (*Figure 66*).




*Graph 51 - Baseline vs New Concept Pressure Distribution*

Surface pressure similarities exist between the baseline and the new concept, with the main plane of the new concept displaying almost identical positive pressure distribution when compared to that of the baseline. The negative pressures produced are very similar also,

however, a greater peak negative pressure is achieved on the new concept, although their gradients are similar.

The greater peak negative pressure does, however, contribute to the formation of the intense vortices illustrated in *Figure 65*, but the introduction of end plates should contribute towards controlling this phenomenon.

### 5.6.1 Modified Main Plane

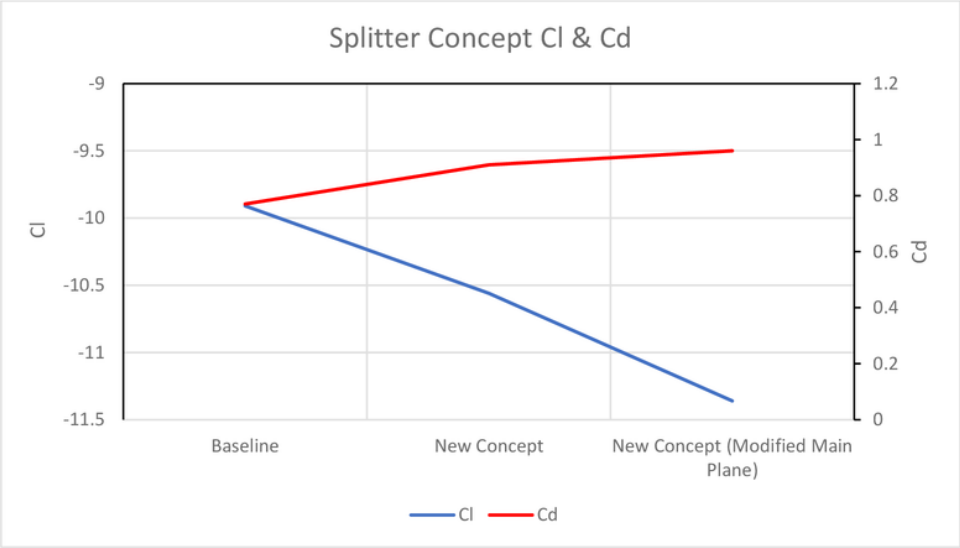



*Figure 67 - Modified Main Plane*

Having small areas of high peak pressure (negative or positive), can allow an aerodynamic device to become incredibly unpredictable in a dynamic situation, as has been previously discussed. As the current concept shows signs of highly concentrated peak pressures, a decision was made to rectify the issue.

One of the causes of this issue is the introduction of high camber geometry. The peak negative pressure builds between a small area on the underside of the profile and the ground. The proposal is to increase the surface area that the peak negative pressure is located on, by reducing the curve of the lower surface. The distance to the ground was also reduced from 60mm to 40mm in order to maintain the pressure differential.

The result of this is illustrated in *Figure 67.* Only a small amendment was introduced, so not as to dramatically affect how the wing performs, or bring about large deviations from the previous studies.



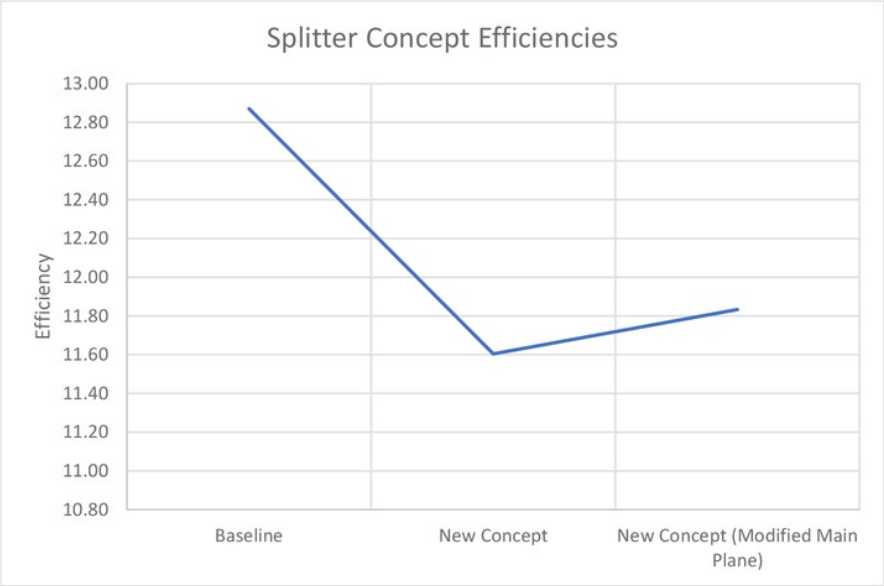

*Graph 52 - Splitter Concepts Cl & Cd*

Introducing these changes has dramatically improved the Cl output of the concept wing by 1.45 from the baseline splitter, with only a marginal increase in the Cd value (*Graph 52*).

*Table 17 - Splitter Concept (Drag & Downforce)*

| | Drag (N) | Downforce (N) |
|---|---|---|
| Baseline Splitter | 310.78 | 3999.76 |
| New Concept | 315.20 | 3657.66 |
| New Concept (Modified Main Plane | 330.35 | 3909.11 |

Downforce production has been raised by 251.45N when compared to that of the new concept prior to modification, with only a 15.15N increase in drag force, thereby improving its efficiency (*Graph 53*). However, these values are not an improvement on the baseline splitter.




*Graph 53 - Splitter Concepts Efficiency*

Reducing the height of the main plane has further improved the influence of ground effect, boosting downforce production, and flattening the lower surface has slowed the incline of drag force by lessening the adverse pressure gradient.

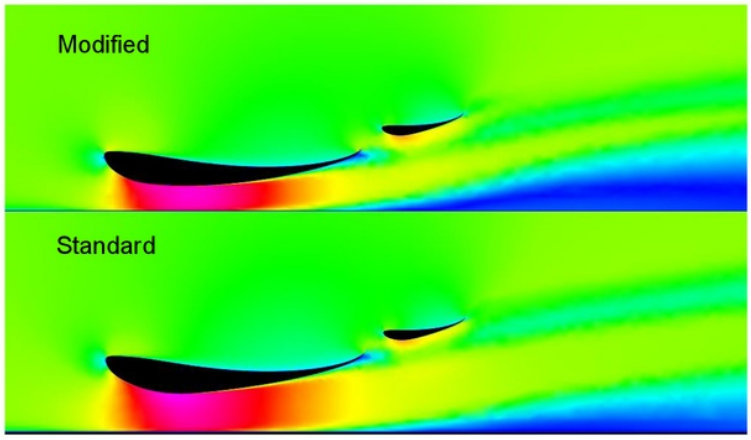
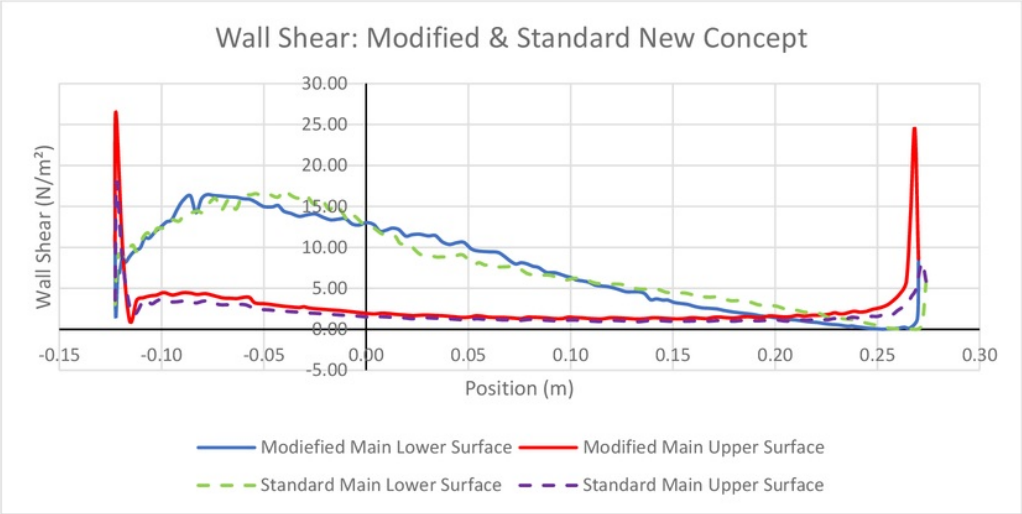



*Figure 68 - Modified & Standard Main Plane Velocity Contours*

The velocity profiles appear similar, thereby maintaining the consistent wall shear values along the chord length between the standard and modified concepts. However, the modified arrangement develops a sharp increase in shear factor at the leading and trailing edges, as a result of its closer proximity to the ground (*Graph 54*).




*Graph 54 - Wall Shear: Modified & Standard New Concept*

The upwash trajectory remains the same in both modified and standard cases, however, due to the reduction in the volume of air travelling beneath the modified main plane, a larger wake formation is apparent, which results in the minor increase in drag force value.

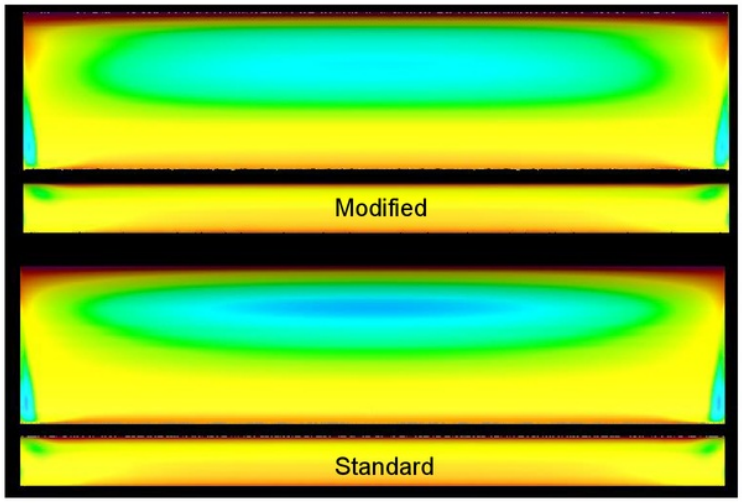
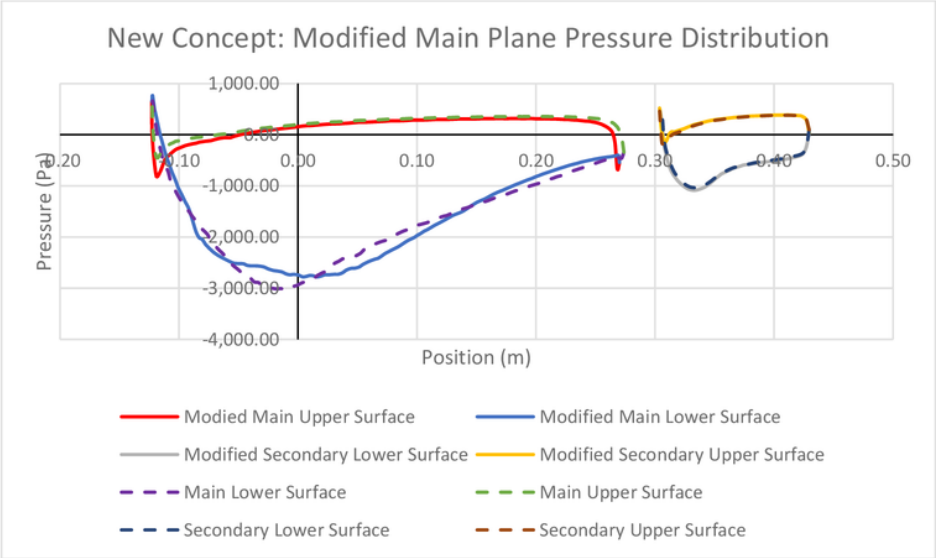



*Figure 69 – Modified & Standard Main Plane Lower Surface Pressure Contours*

A reduction in peak negative pressure has been achieved, producing a minor decrease in pressure differential. However, the distribution of negative pressure has uniformly increased (*Figure 69*), together with its gradient transition back to atmospheric pressure which has also increased (*Graph55*). This has resulted in a small increase in trailing edge separation on the main plane, which is also represented in the wall shear values (*Graph 54*).




*Graph 55 - New Concept: Modified Main Plane Pressure Distribution*

## 6.0.0 Whole Car Study

In order to apply the new concept, minor modifications were made to the front wheel pontoons to accommodate the new main plane and maximise its performance potential.

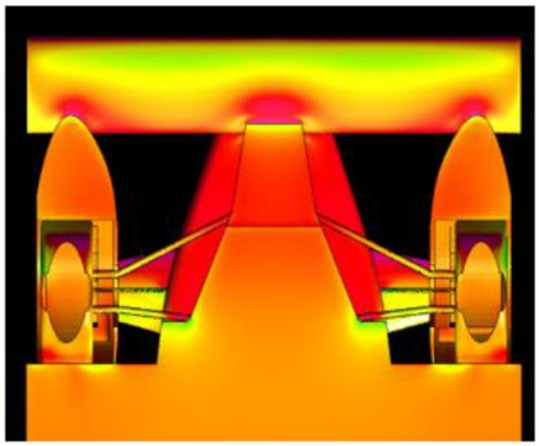


*Figure 70 - Lower Surface Pressure Stagnation*

Due to the geometry of the pontoons and crash box, pressure stagnation areas were created on the lower surface of the main plane, which inhibited its performance (*Figure 70*). In addition, the original front upper wishbone shroud geometry was also removed. This decision was resulted from earlier studies where it was found to be restricting the created upwash from the splitter and generating lift, thus counteracting the majority of the downforce produced (*Figure 71*).

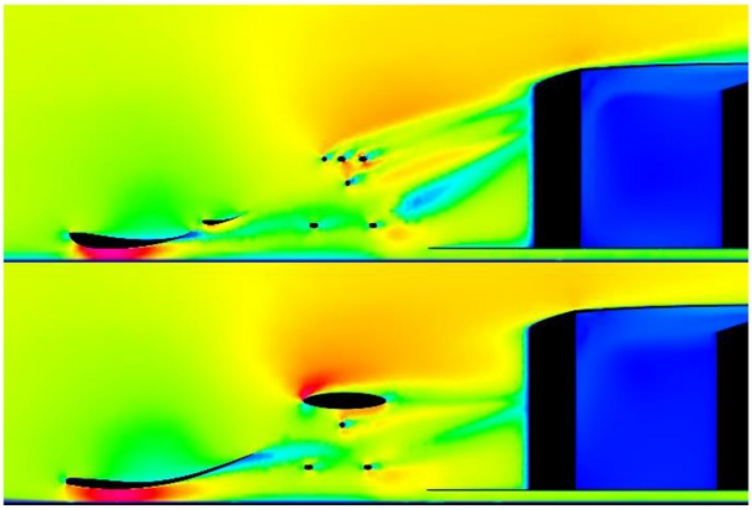


*Figure 71 - New Concept vs Baseline (Velocity Contours)*

A comparison between the new concept and the baseline indicates a much greater upwash flow field being produced. A greater velocity is reached beneath the main plane compared to that of the baseline splitter, resulting from the larger pressure differential being created. The velocity contours shown are projected onto a plane located 45mm parallel to the central longitudinal plane of the car.

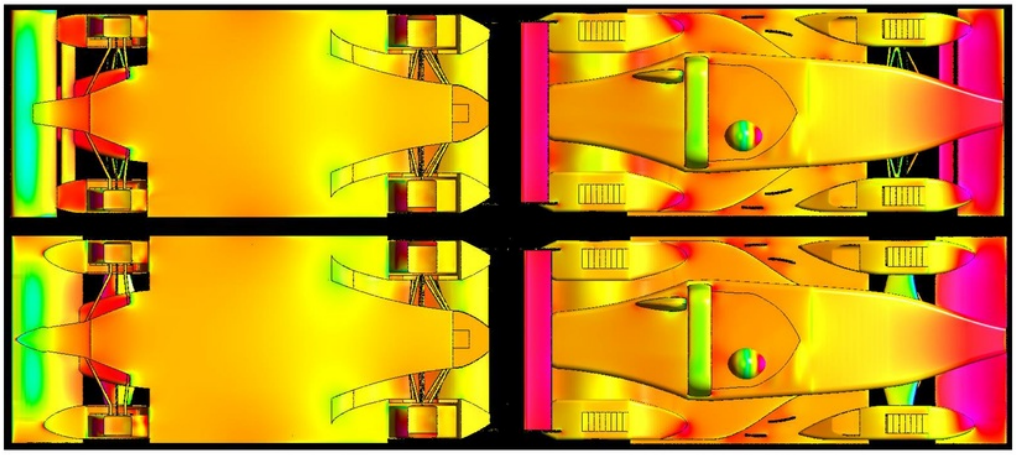


*Figure 72 - New Concept vs Old Concept Pressure Contours*

As *figure 72* illustrates, the negative pressure on the underside of the main plane has increased considerably in both area and strength. This is as a result of adjusting the pontoon geometry, which has subsequently created a high pressure region on the underside of both pontoons, as the leading edges were raised to the trailing edge of the main plane (*Figure 73*).

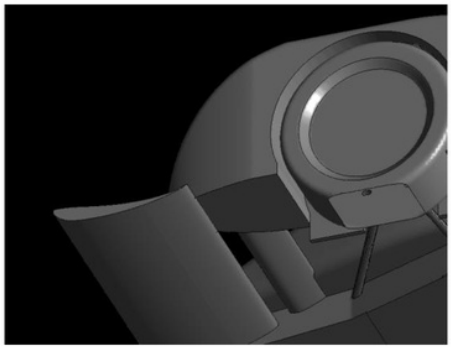
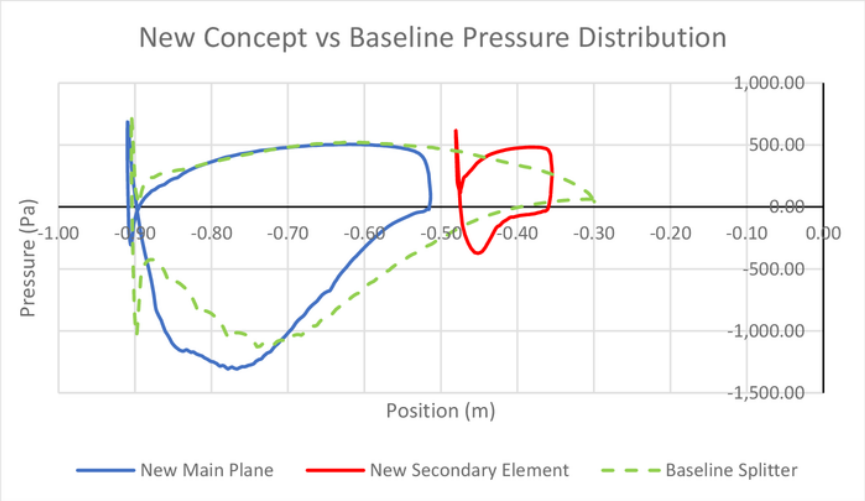


*Figure 73 - Front Pontoon Geometry Change*

The high pressure field on the upper surface of the wing has also been maintained, however, a minor amount of pressure is lost through the slot gap between profiles.

The new concept, in isolation, developed large vortices which spilled over its edges, increasing the induced drag force. It was decided not to extend the secondary element to the same span as the main plane, but to use the nose cone and wheel pontoons as end plates, which would thereby obstruct the positive pressure gradient, and reduce overall drag force.




*Graph 56 - New Concept vs Old Concept Pressure Distribution*

As predicted, a considerable loss of negative pressure can be observed when the new concept is applied to the car. A negative loss of 1450Pa is registered when comparing the new concept in isolation, to when it is applied to the car. This results from the stagnation build up at the frontal area of the vehicle bleeding forward, which then affects the pressures produced, thus decreasing the pressure differential.

A lesser amount of pressure difference can be observed on the baseline splitter from isolation to application, with only a loss of 800Pa, causing it to have a greater negative pressure over a longer chord distance.

The reason for this could be as a result of the new concept being developed in isolation, therefore, the constraints that the car would apply were not fully accounted for or understood, whereas the baseline splitter was fully developed on the car, with no isolated studies.

*Table 18 - New Concept vs Baseline Specifications*

| | Cl | Cd | Efficiency |
|---|---|---|---|
| **Baseline** | -1.58 | 0.54 | 2.93 |
| **New Concept** | -1.45 | 0.56 | 2.59 |
| **Difference** | -0.13 | 0.02 | 0.34 |

*Table 18,* indicates the coefficients that both the baseline and the current new concept produce. As the figure below (*Figure* 74) illustrates, a much larger edge vortex is produced by the new concept splitter. As has been previously discussed, the concave geometry of the S1223 generates a greater pressure gradient, creating an intense vortex, whereas the baseline splitter has almost symmetrical edges, therefore the pressure on the top surface and bottom surface do not generate the intense vortices.

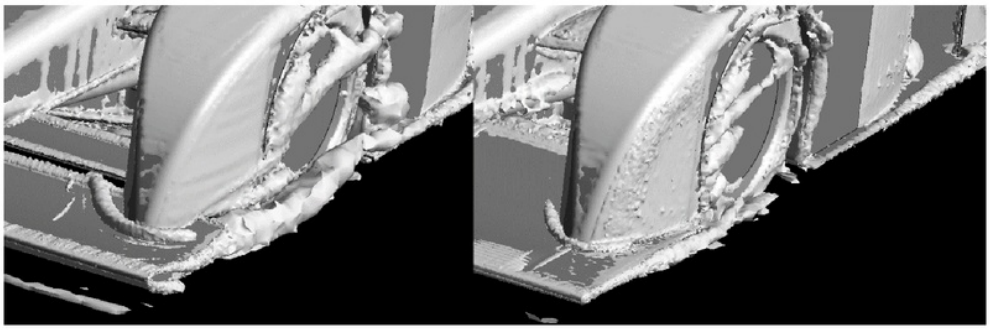


*Figure 74 - New Concept & Baseline Edge Vortices*

Both new concept and baseline show vortex development on the lower leading edge of the pontoon as the high pressure mixes with the lower pressure developed on the pontoon sides. The new concept, however, displays a larger vortex interacting with the secondary element (*Figure 74*).

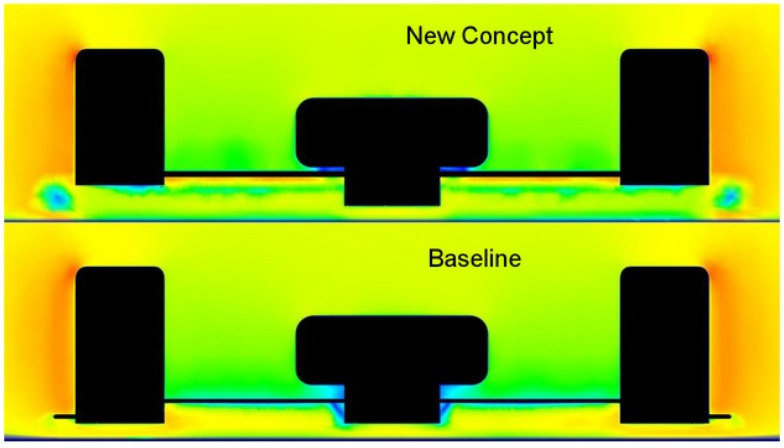



*Figure 75 - Splitter Edge Vortex Velocity Contours*

Fixing end plate components allows a constant separation of adverse pressures, which reduces wing tip vortex development, and allows greater surface area usage, and a greater pressure differential. This reduces induced drag and potentially increases downforce, thus improving aerodynamic efficiency (www.caeses.com, 2018).

The vortex generation between both baseline and the new concept is illustrated above in terms of velocity (*Figure 75*). As can be observed, considerable differences are apparent in velocity during the swirling motion of the vortex.

A reduction in vortex size could be achieved by reducing the camber on the edges of the main plane, however, this may reduce the downforce production, therefore, end plates will maximise downforce while still controlling vortex development.

## 6.1.0 End Plate Development

Five end plate developments were constructed, each subsequent design developed from the previous, starting with a generic rectangle plate fixed to the edge of the wing (*Figure 76*).

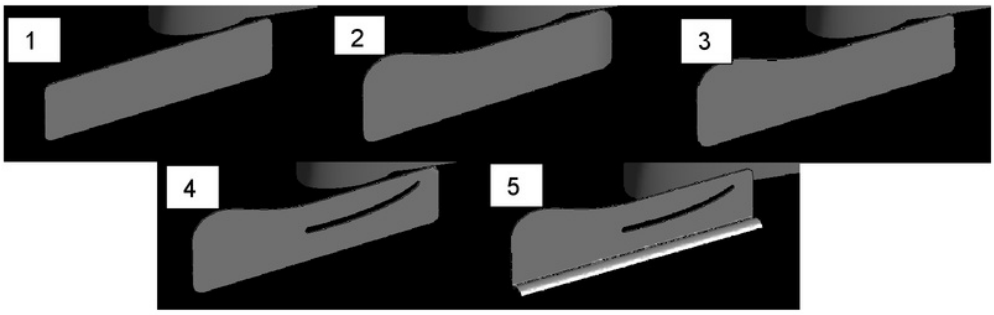



*Figure 76 - End Plate Development Geometries*

As the main plane is a set at a 40mm ground clearance, the end plate lower edge falls 40mm to the ground, therefore it is tangential to the main plane lower surface.

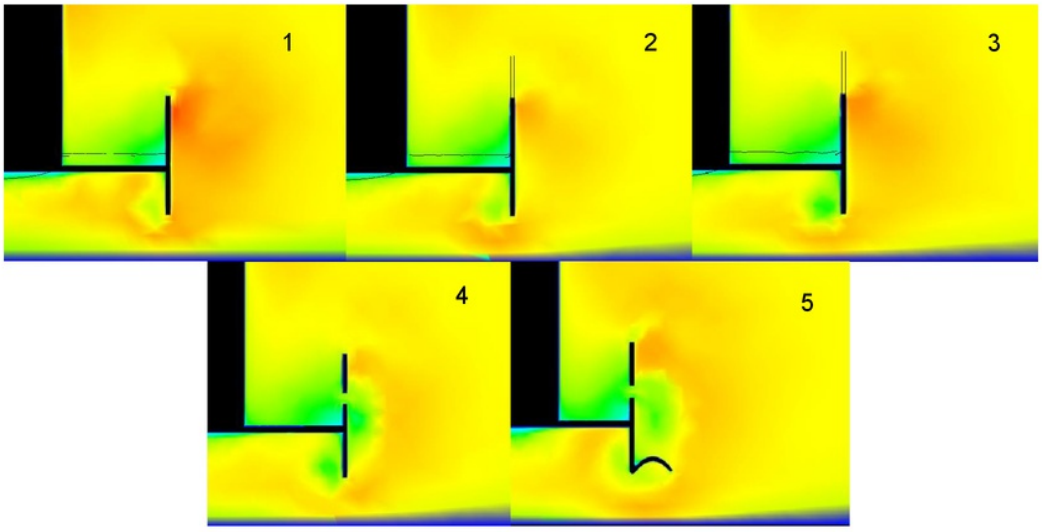



*Figure 77 - End Plate Development Velocity Contours*

The above velocity contours (*Figure 77*), project from a plane located perpendicular to the longitudinal axis at a, distance of 0.55m forward of the front axle.

In each case, vortex development is still present, however, reducing the size of the vortex and changing its location were paramount. Even with the introduction of an end plate, ambient pressure air was still bleeding onto the low pressure side of the main plane. A study previously conducted, discovered the same characteristics when examining an aeroplane wing in ground effect, and that the vortex velocities were significantly reduced on the high

pressure side of the wing, thereby increasing the pressure differential (Jung, et al., 2012). It has also been discussed that as ride height reduced, the developed edge vortices increased in intensity and gathered a formation along the inner edges of front wing end plates (Zhang, et al., 2006), as can be observed in *Figure 77*.

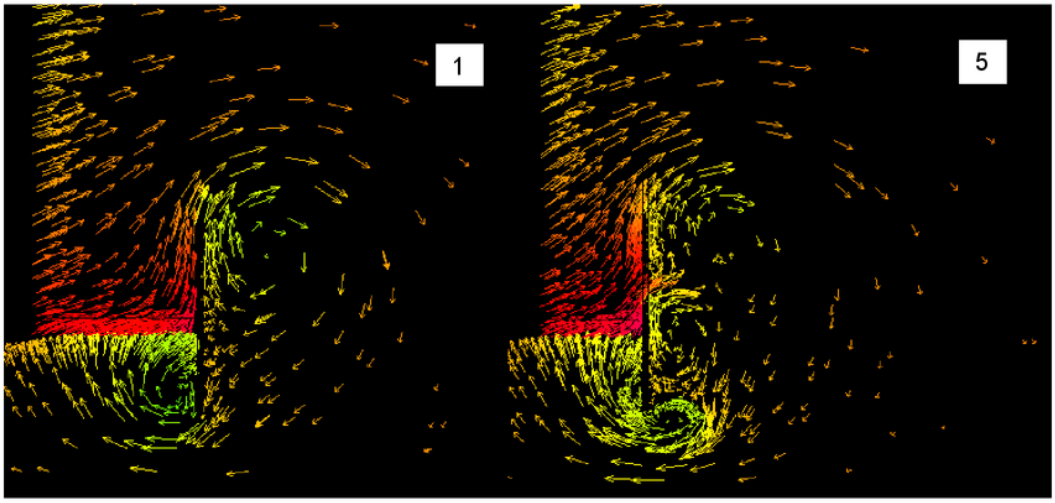



*Figure 78 - End Plate Development 1 & 5 Pressure Vectors*

Even with the employment of end plates, a large vortex formation was still developing at the top edge of the end plate, which then bled onto the underside. A commonly used technique is to introduce slats within the main body of the end plate above the high pressure side of the wing. As *Figure 78* illustrates, high pressure is able to bleed through the slot and obstruct the larger vortex. The slot also allows an equalisation of surface pressure, lowering the pressure gradient, and reducing the size of the wing tip vortices. (Mullen, 2017). A “foot plate” was also introduced to further the obstruction of the vortex. The curved geometry of the foot plates captures any pressure bleed and controls its trajectory, stopping any lower surface interference and directing any vortex towards sealing the floor of the car. To accommodate the foot plate, the main plane span was reduced by 30mm to maintain regulation legality.

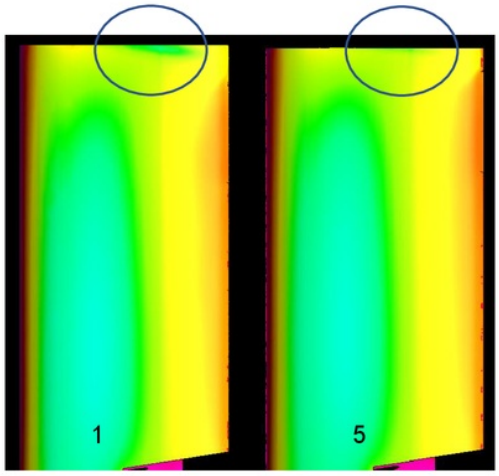



*Figure 79 - End Plate Development Pressure Bleed*

As highlighted in *Figure 79*, the final end plate development has significantly reduced the pressure bleed.

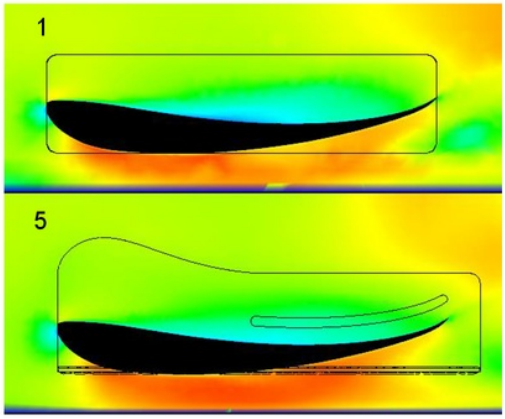



*Figure 80 - Wing Edge Velocity Contours*

Reducing its vortex formation increases the predictability of the front wing, thereby providing a greater uniformity of pressure distribution. *Figure 80,* illustrates the increase of velocity at a point 30mm inboard of the end plate, displaying a greater uniformity of velocity across the span of the wing.

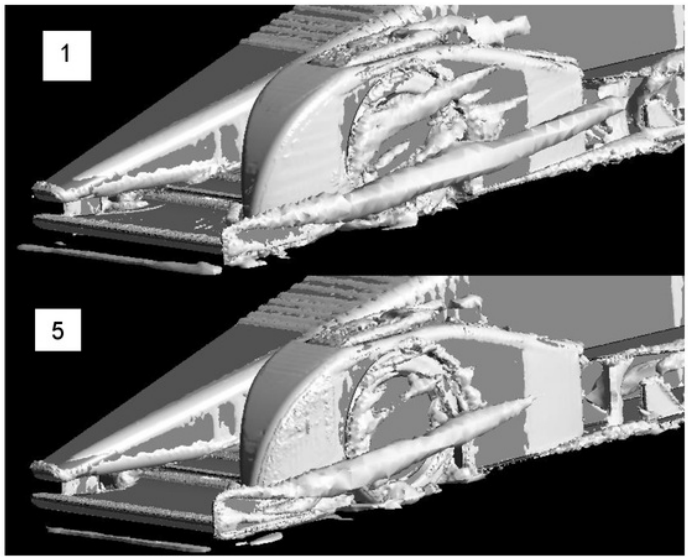


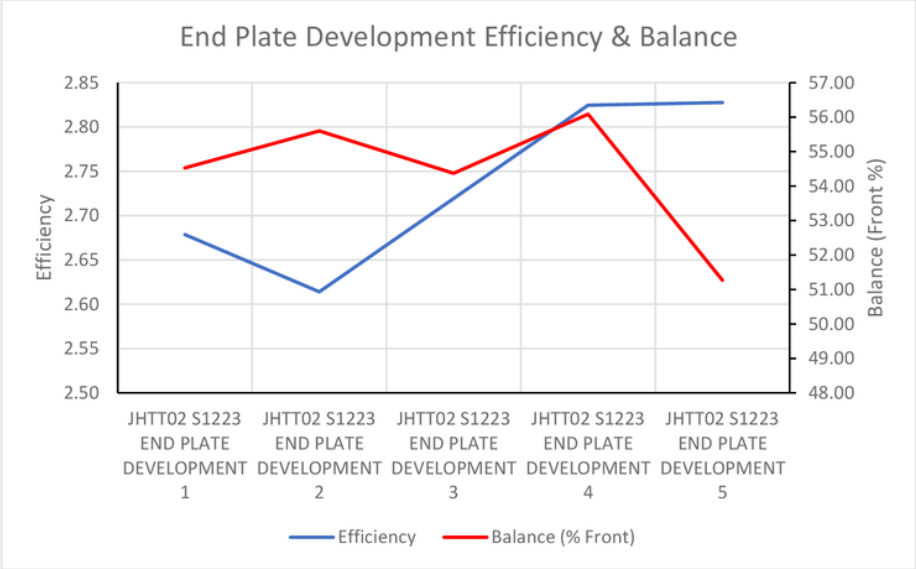

*Figure 81 - End Plate Development Vortices*

The magnitude and intensity of the vortices illustrated in *Figure* 81 has been considerably reduced, however, *Graph 57* indicates an increase in Cd value, resulting in a 20N increase in drag force. This results from the generation of three vortices and the use of blockage, thereby increasing the induced drag, although its benefit is reflected in the major increase of 137N of downforce.




*Graph 57 - End Plate Development Cl & Cd*

Further investigation is needed regarding the development and justification of end plates, though the components benefits are clear, a sharp incline of Cd is seen, though efficiency is improved (*Graph 58*).




*Graph 58 - End Plate Development Efficiency & Balance*

Although a decrease in frontal balance is seen (*Graph 58*), it still displays an increase of 3.7% from the baseline geometry.

*Table 19 - Baseline Car & New Concept Car Specifications*

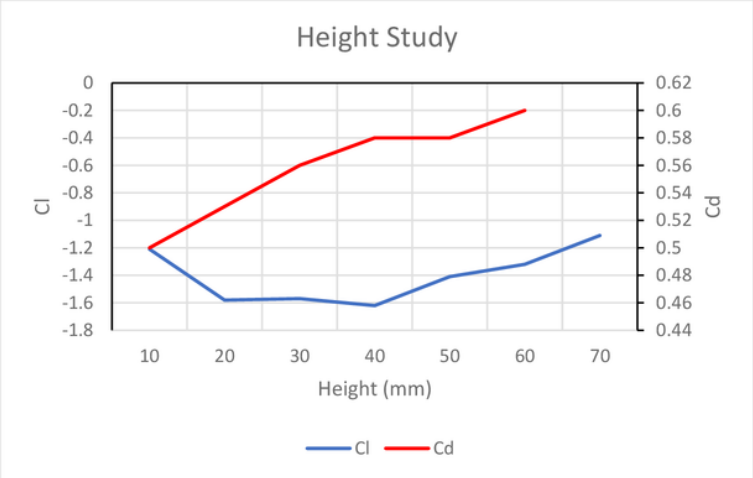
| | DRAG (N) | DOWNFORCE (N) | DOWNFORCE (KG) | EFFICIENCY | BALANCE (% Front) | FRONT DOWNFORCE (N) | REAR DOWNFORCE (N) | CoP Distance Behind Coord (m) | Cd | Cl |
|---|---|---|---|---|---|---|---|---|---|---|
| JHTT02 (OSS BASELINE) | 529 | 1549 | 158 | 2.93 | 47.56 | 737 | 812 | 1.3601 | 0.54 | -1.58 |
| JHTT02 S1223 END PLATE DEVELOPMENT 5 | 569 | 1608 | 164 | 2.83 | 51.27 | 824 | 783 | 1.264 | 0.58 | -1.64 |

Despite a small increase in frontal balance, the overall frontal downforce production has increased by almost 100N with frontal downforce now greater than rear downforce. Although, these results remain questionable as only half car models were utilised for the simulation studies in order to maintain efficient time management. This provides relativity for the end plate development, although comparing these results to results produced from a full car model may prove to be numerically uncertain.

## 6.2.0 Attitude Study

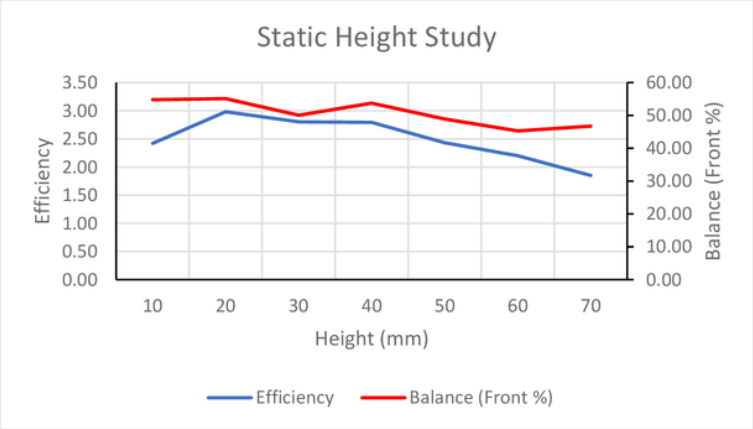
Potential gains in efficiency could be made through an attitude study, investigating steady state (static) setup and dynamic variables.

### 6.2.1 Height



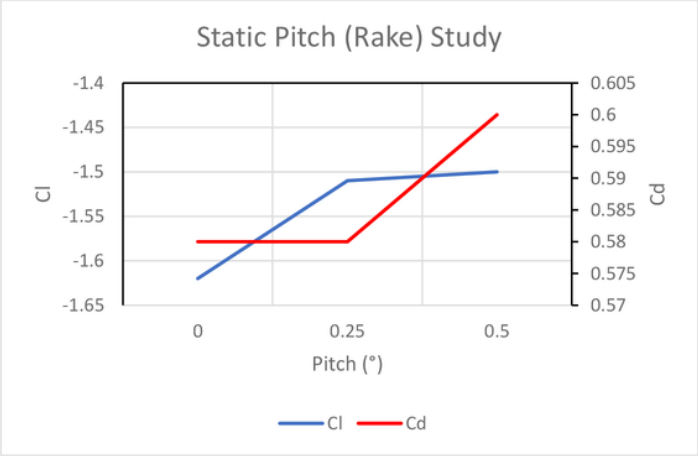

*Graph 59 - Height Cl & Cd*

A study has been produced that shows that a close proximity to ground enhances downforce production from a wing, until boundary layers began to mix, causing a blockage of free stream air, thereby reducing overall downforce (Ranzenbach & Barlow, 1994). A height of 40mm was found to produce the maximum downforce, however a height of 20mm produced superior efficiency. A 50% balance of aerodynamic force was achieved at a height of 40mm, therefore allowing the car to remain neutral, although the Cp is still located forward of the CoG, which is preferable (Katz, 1995).




*Graph 60 - Height Efficiency & Balance*

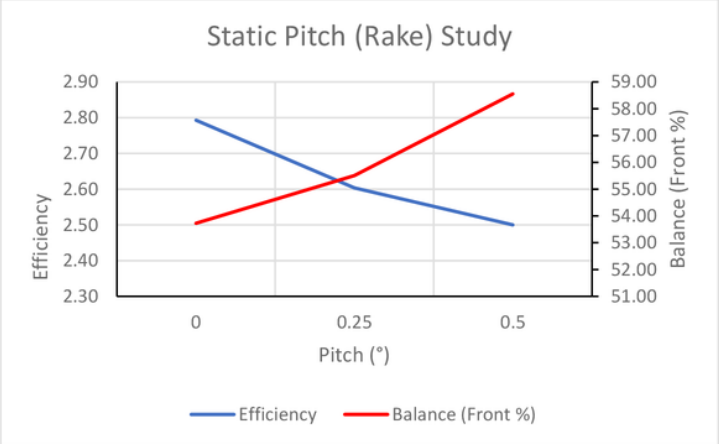
### 6.2.2 Static Pitch




*Graph 61 - Static Pitch Cl & Cd*

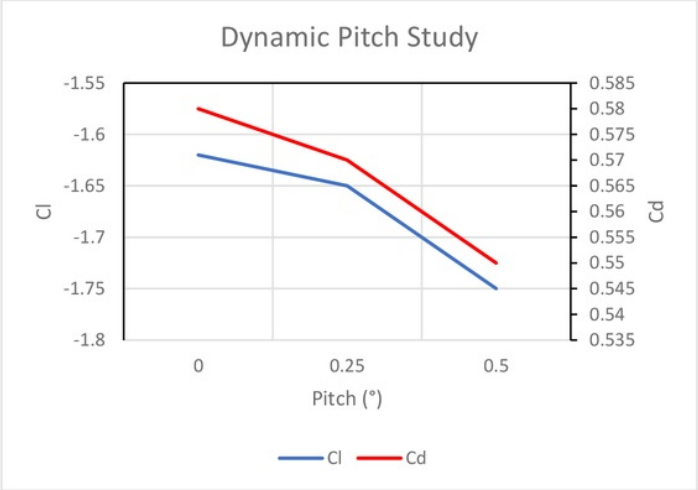
Static pitch is defined as a change in angle whereby the front ride maintains a 40mm height from the ground while a negative incidence angle is applied, effectively mimicking steady state conditions.

It has been suggested that angles no greater than 2° are used, as the generated expansion becomes too great. This consequently creates a pressure differential from front to rear that the contained energies within the air flow cannot overcome, thus separation begins to occur (McBeath, 1998). Interestingly, despite only a minimal angle of incidence, *Graphs 61* and *62* each illustrate that the JHTT02 generates greater downforce and better efficiency at 0°, therefore being flat. As anticipated, the frontal balance increases as a greater rake angle is applied, resulting from the rear of the car being removed from ground effect influence.




*Graph 62 - Static Pitch Efficiency & Balance*

### 6.2.3 Dynamic Pitch




*Graph 63 - Dynamic Pitch Cl & Cd*

Unlike static pitch, dynamic pitch allows the front ride height to drop lower than the 40mm ride height, thus recreating a braking scenario (dive), as longitudinal load transfer occurs.

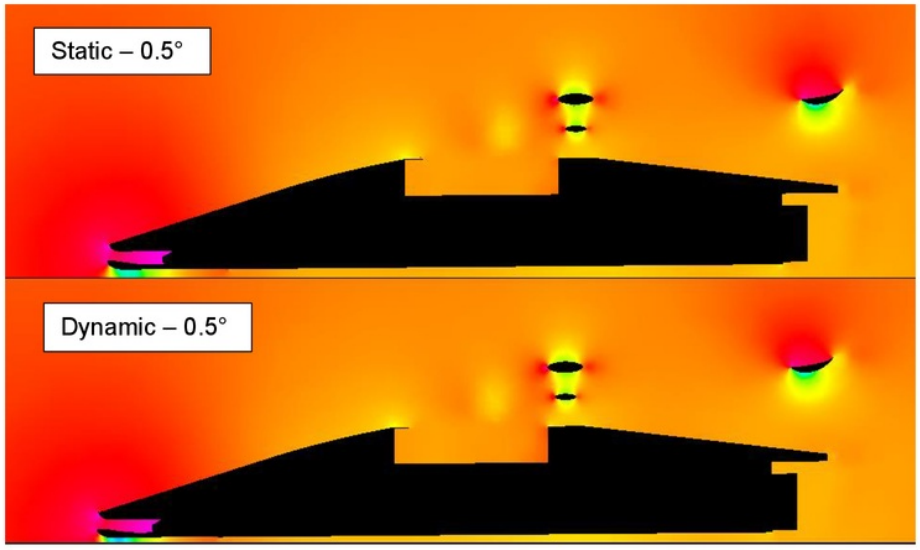
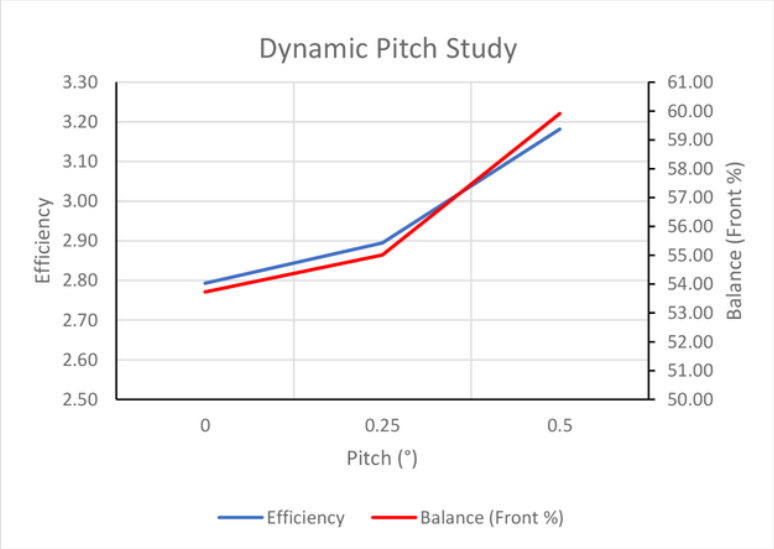



*Figure 82 - Symmetry Plane Pressure Contours*

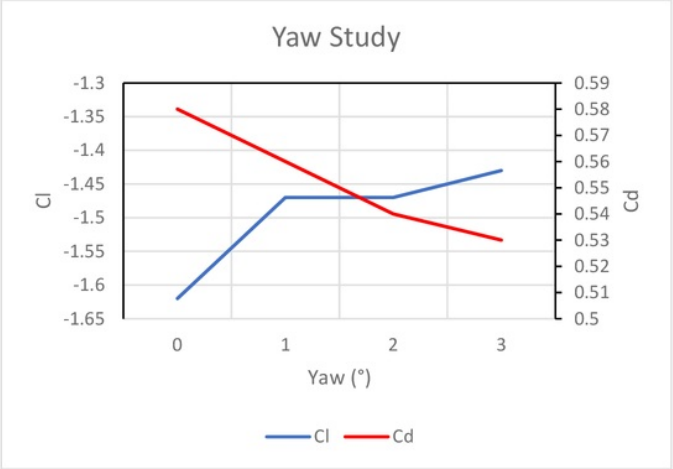
The results obtained are interesting, and unexpected, as Cl increases with a large gain in efficiency as pitch angle also increases. This could be as a result of the large negative pressure increase observed at the front wing when ground proximity is reduced. This is also reflected in *Graph 64*, with a large increase in frontal balance. When an overall lower ride

height is produced, a lower pressure is present along the entire length of the floor, in a dynamic situation (*Figure 82*).




*Graph 64 - Dynamic Pitch Efficiency & Balance*

### 6.2.4 Yaw




*Graph 65 - Yaw Study Cl & Cd*

A basic yaw study was conducted with a neutral ride height of 40mm. This simplifies the results as only the effects of yaw will impact on the results obtained.

As yaw angle is added, both Cl and Cd undergo significant drops, although a minor increase in drag force is observed due to the growth in the projected frontal area.

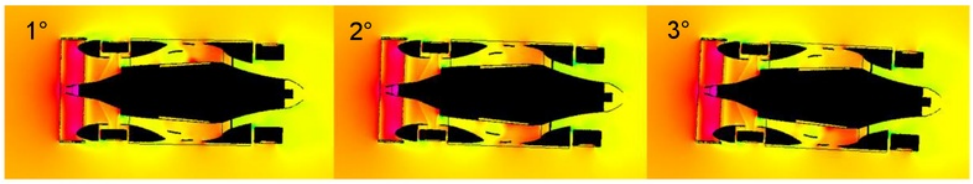
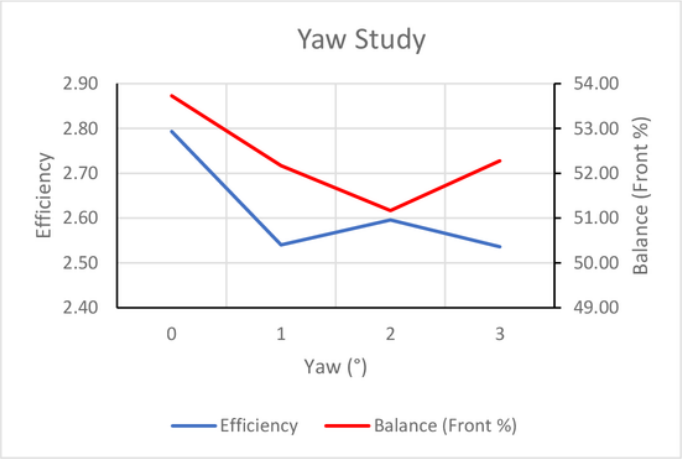



*Figure 83 - Yaw Angle Pressure Contours*




*Graph 66 - Yaw Study Efficiency & Balance*

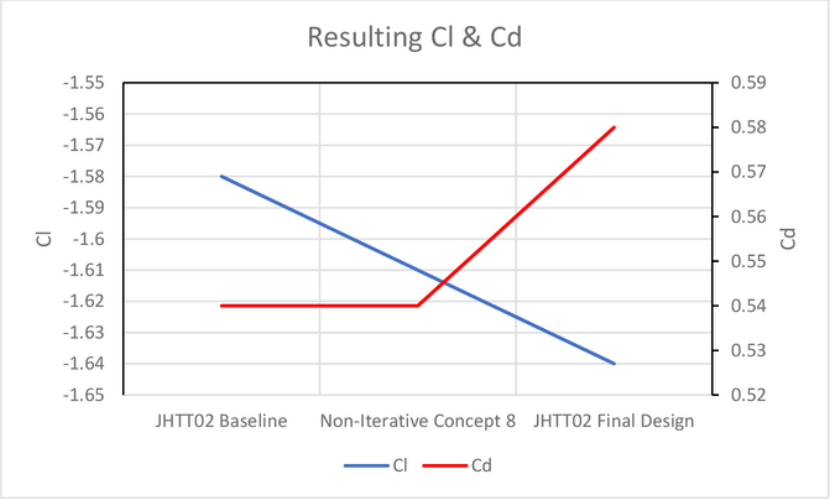
As the angle of yaw increases, it can be observed that the end plate vortex formation becomes asymmetric from each side, with the inner vortex shedding away from the car and the inner vortex being drawn into the outside front wheel. If further studies were conducted, it may be found that this has a significant detrimental effect further down the car, affecting the entire balance of the vehicle. However, the current studies show very little change, though it can be observed that as the yaw angle increases, the bias of aerodynamic balance develops rearwards.

# 7.0.0 Conclusion & Evaluation

*Table 20 – Final Results*

| | DRAG (N) | DOWNFORCE (N) | EFFICIENCY | BALANCE (% Front) | FRONT DOWNFORCE (N) | REAR DOWNFORCE (N) | CoP Distance Behind Coord (m) | Cd | Cl |
|---|---|---|---|---|---|---|---|---|---|
| JHTT02 Baseline | 529 | 1549 | 2.93 | 47.56 | 737 | 812 | 1.3601 | 0.54 | -1.58 |
| Non-Iterative Concept 8 | 529 | 1578 | 2.98 | 44.48 | 702 | 876 | 1.44 | 0.54 | -1.61 |
| JHTT02 Final Design | 569 | 1608 | 2.83 | 51.27 | 824 | 783 | 1.264 | 0.58 | -1.64 |

A design process was conducted on an OSS sports prototype racing car to improve frontal downforce and aerodynamic efficiency to create a wider working window of aerodynamic performance that would benefit the racing car in multiple dynamic situations.

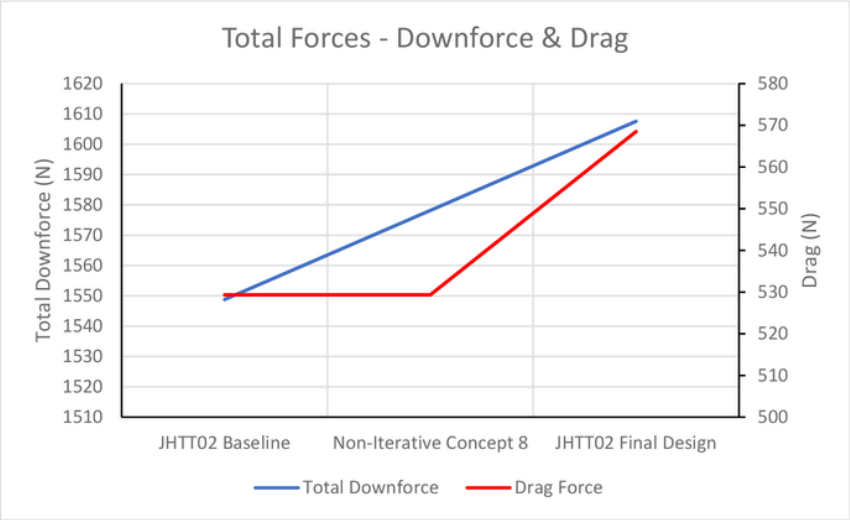



*Graph 67 - Resulting Cl & Cd*

A great improvement in Cl had been obtained through the iterative design process for a new front wing concept, experimenting with different heights and AoA, and employing DOE software to optimise design solutions.

As *Graph 67* describes, a vast improvement in overall Cl has been accomplished, although it has been obtained at the price of compounding Cd. This has therefore reduced the efficiency of the newly designed aerodynamic package (*Table 20*), which has conflicted with one of the main aims of this project, with the non-iterative design process possessing the greater efficiency.

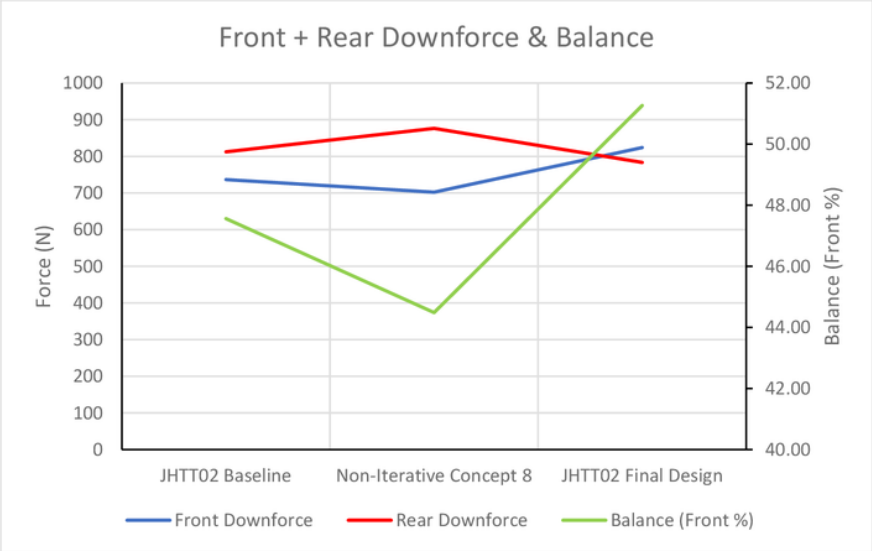
Regardless of this, a full design process needed to be conducted in order to obtain a fundamental understanding of the affects that different wing profiles and arrangements have on aerodynamic performance.




*Graph 68 - Total Forces*

The coefficients produced in *Graph 67* are reflected in *Graph 68*, with the JHTT02 Final Design (New Concept) producing the greatest amount of downforce, however, with a large drag force equivalent.

As has been previously discussed, the original splitter concept was designed based on the vehicle geometry as it was in its development stages. Therefore, the car was designed as a whole entity, whereas, this study involved embarking on a new concept from scratch, without making further significant changes to the previous bodywork.




*Graph 69 - Front + Rear Downforce & Balance*

Using the S1223 profiles, a gain in frontal downforce has been achieved, with previous designs having a bias towards rear downforce.

The initial concern regarding a high peak of concentrated negative pressure resulting from the highly cambered geometry of the selected S1223 profile was resolved, producing a gradual gradient of pressure along the main planes surface. Introducing a secondary element of the same profile induced a further pressure differential, greatly affecting the working nature of the main plane, thus further downforce generation was gained.

### 7.1.0 Recommended Further Work

On further reflection, it could be believed that some complications were to be expected from the very beginning of the project. To gain a full understanding of wings, standardised profiles were utilised, the baseline geometry included a fully developed non-standard profile, therefore being designed around the full concept of the car. If the same studies conducted in this report were conducted again, however, with a fully developed profile, further gains in efficiency could be made.

The combinations of profiles tested within the confines of this project were limited due to time constraints. If multiple profiles were tested, it may be found that gains could be made with increasing AoA without the dramatic increase in induced drag force observed.

An in-depth understanding of the DOE software needs to be gained. Several important decisions were made without a comprehensive knowledge or understanding of the software, especially within the area of optimisation. Maximum Cl values were pursued with the lowest possible Cd values. However, it may have been of value to pursue a lower Cl, in order to improve overall efficiency and accept the loss of total downforce, then subsequent developments could be introduced to recover any losses.

Although the end plates that were developed proved pivotal in front wing performance, additional developments could be introduced with regard to vortex control, and whether a full reduction in vortex formation could be made and if, indeed, it needs to be made.

In order to validate the final findings, it could be considered that a scale model of each of the designs presented in *Table 20* was constructed and individually tested in a wind tunnel. This would then confirm any fluid flow formation, and depending on the complexity of the model and wind tunnel, the figures for the downforce produced and the drag force could be obtained. Failing this, a simulator could be utilised with the concerned car modelled within its coding. Utilising this feature could prove effective in producing an optimal aerodynamic map, therefore, a further understanding of the full aerodynamic package could be obtained and subsequent design developments considered.

Further CFD cases could be made with regard to an attitude study, as these, along with the simulator would provide a fully comprehensive aerodynamic map. This should be considered more valuable than any of the whole car tests conducted within this report, as it will define how the car performs in a dynamic situation, rather than steady state, which is near impossible to achieve in reality.

## 8.0.0 References


Abdullah, A. et al., 2017. *Ground proximity effect on the flow over NACA 4412 multi-element airfoil in clean configuration,* Johor: IOP Publishing.

Abdulwahab, S. F., 2015. *AERODYNAMIC EVALUATION OF RACING WINGS OF A FORMULA CAR,* Hertfordshire: University of Hertfordshire.

Ahmad, N. E., Abo-Serie, E. & Gaylard, A., 2010. *Mesh Optimization for Ground Vehicle Aerodynamics,* Coventry: Coventry University.

Anderson, J. D., 1991. *FUNDAMENTALS OF AERODYNAMICS.* 2 ed. New York: McGraw-Hill.

Balmer, D., 2003. *Separation of Boundary Layers,* Edinburgh: University of Edinburgh.

Banihani, E., 2018. *Velocity boundary layer development on a flat plate.* [Online]
Available at: www.researchgate.net/figure/Velocity-boundary-layer-development-on-a-flat-plate-2_fig1_323218834
[Accessed 20 3 2019].

Birchall, M., 2011. *Aerofoil.* [Online]
Available at: www.aviationknowledge.wikidot.com/aviation:aerofoil
[Accessed 19 3 2019].

Bradshaw, P. & Huang, G. P., 1995. *Law of The Wall in Turbulent Flow,* Stanford: Stanford University.

Brookes, J., 1999. *#5 AMG Mercedes CLR LMGTP: Christophe Bouchut, Nick Heidfeld, Peter Dumbreck.* [Online]
Available at: ca.motorsport.com/lemans/photos/5-amg-mercedes-clr-lmgtp-christophe-bouchut-nick-heidfeld-peter-dumbreck-3/20285108/
[Accessed 13 3 2019].

Brooks, B. et al., 2003. Formula SAE Design; Test, Tune and Setup; A Design of Experiment Approach. *SAE Transactions,* 112(6), pp. 1397-1410.

BRSCC, 2019. *OSS CHAMPIONSHIP.* [Online]
Available at: www.brscc.co.uk/formulae/oss-championship/
[Accessed 18 3 2019].

Carney, D., 2016. *A 24-hour battle of speed and EFFICIENCY,* Chicago: SAE International.

Christopher, B., 2015. *Studying the Airflow Over a Car Using an Ahmed Body.* [Online] Available at: www.comsol.com/blogs/studying-the-airflow-over-a-car-using-an-ahmed-body/ [Accessed 23 3 2019].

Condra, L. W., 1991. *Reliability Improvement with Design of Experiments.* 2 ed. Seattle: Taylor & Francis Group.

Craig, C. & Passmore, M., 2014. *Methodology for the Design of an Aerodynamic Package for a Formula SAE Car,* Loughborough: SAE International.

Dominy, R. G., 2002. *Sports Prototype Race Car Optimization ,* Indianapolis: SAE International.

Durrer, S., 2016. *Aerodynamics of Race Car Wings, a CFD Study,* Allendale: Grand Valley State University.

Ferreira, S. C. et al., 2007. *Box-Behnken design: An alternative for the optimisation of analytical methods,* Bahia: Science Direct.

Fielding, S., 2005. *Laminar Boundary Layer Separation,* Manchester: The University of Manchester.

Fletcher, T., Altringham, J., Peakall, J. & Wignall, P. B., 2014. *Hydrodynamics of fossil fishes,* s.l.: Proceedings of The Royal Society.

Frei, W., 2017. *Which Turbulence Model Should I Choose for My CFD Application?.* [Online] Available at: uk.comsol.com/blogs/which-turbulence-model-should-choose-cfd-application/ [Accessed 23 3 2019].

Glownia, J. M., 2007. *Lift,* Stanford: Stanford University.

Hall, N., 2015. *Navier - Stokes Equations, 3 Dimensional, Unsteady.* [Online] Available at: www.grc.nasa.gov/www/k-12/airplane/nseqs.html [Accessed 23 3 2019].

Hall, N., 2018. *Incorrect Theory.* [Online] Available at: www.grc.nasa.gov/www/k-12/airplane/wrong1.html [Accessed 20 3 2019].

Hayes, C., 2016. *OSS Downforce* [Interview] (23 6 2016).

Hellio, C. & Yebra, D. M., 2009. *Advances in Marine Antifouling Coatings and Technologies.* 1 ed. s.l.:Woodhead Publishings.

history.nasa.gov, 2010. *SP-4103 Model Research - Volume 2.* [Online]
Available at: www.history.nasa.gov/SP-4103/app-f.htm
[Accessed 20 3 2019].

Hughes, J., 2018. *External Computational Fluid Dynamics Simulation Validation Experiment – MIRA Wind Tunnel,* Swansea: University of Wales Trinity Saint David.

Iley, J., 2018. *OSS Splitter Performance Window* [Interview] (7 11 2018).

Jackson, F. F., 2018. *Aerodynamic optimisation of Formula student vehicle using computational fluid dynamics,* Huddersfield: University of Huddersfield.

Jung, J. H. et al., 2012. Endplate effect on aerodynamic characteristics of three-dimensional wings in close free surface proximity. *Internation Journal of Naval Architecture and Ocean Engineering,* 4(4), pp. 477-487.

Kachare, S. C., 2017. *A CFD Study of a Multi-Element Front Wing for a Formula One Racing Car,* Allendale: Grand Valley State University.

Katz, J., 1995. *Race Car Aerodynamics: Designing For Speed.* 1 ed. Massachusetts: Bentley Publishers.

Lanfrit, M., 2005. *Best practice guidelines for handling Automotive External Aerodynamics with FLUENT,* Darmstadt: Fluent Deutschland GmbH.

Machin , R., 2015. *INTRODUCTION TO RACECAR AERODYNAMICS ,* s.l.: Brook Motorsport.

Marekk, 2011. *Diffuser functions.* [Online]
Available at: www.f1technical.net/forum/viewtopic.php?t=9813&start=60
[Accessed 25 3 2019].

McBeath, S., 1998. *Competition Car Downforce.* 1 ed. Nr Yeovil: Haynes Publishing.

McGraw-Hill Concise Encyclopedia of Physics, 2002. *Concise Encyclopedia of Physics.* s.l.:The McGraw-Hill Companies.

MCR Race Cars, Sports Racing Car Manufacturers, 2019. *Silverstone.* [Online]
Available at: www.facebook.com/MCRRaceCars/
[Accessed 17 3 2019].

MCR Race Cars, 2018. *MANUFACTURERS OF SPORTS PROTOTYPE RACING CARS.* [Online]

Available at: www.mcrracecars.co.uk
[Accessed 17 3 2019].

Mokhtar, W. & Durrer, S., 2016. *A CFD Analysis of a Race Car Front Wing in Ground Effect,* Allendale: American Society for Engineering Education.

Morris, S. & Williams, H., 2018. *SRCC SPORTS 2000 DURATEC CHAMPIONSHIP SPORTING & TECHNICAL REGULATIONS 2018,* Borough Green: SRCC .

Motorsport UK, 2019. *Technical Regulations,* Colnbrook: MSUK.

Mullen, J., 2017. *Case study – Rear Wing Endplate Variants,* Potterhanworth: JMRANALYTICAL.

Newton, I., 1687. *Philosophiæ Naturalis Principia Mathematica.* 1 ed. s.l.:Benjamin Motte.

Panchal , K., 2015. *Computational Assessment of Front and Rear Wing of Amity Racing Vehicle,* Noida: SAE International.

Proust, M., 2009. *Design of Experiments,* Cary: JMP.

Quintarelli, A., 2018. *Aerodynamic efficiency, balance and center of pressure.* [Online]
Available at: www.http://theracingline.net/2018/race-car-tech/race-tech-explained/aerodynamic-efficiency-balance-and-center-of-pressure/
[Accessed 22 3 2019].

Ranzenbach, R. & Barlow, J., 1994. *Two-Dimensional Airfoil in Ground Effect, An Experimental and Computational Study,* s.l.: SAE International.

Selig, M. S., Guglielmo, J. J., Broeren, A. P. & Giguere, P., 1995. *Summary of Low-Speed Airfoil Data,* Virginia Beach: SOARTECH PUBLICATIONS .

Seljak, G., 2008. *Race Car Aerodynamics,* Ljubljana: University of Ljubljana.

Sergio, 2017. *Validity of the Navier Stokes equations for turbulent flows.* [Online]
Available at: www.physics.stackexchange.com/questions/356407/validity-of-the-navier-stokes-equations-for-turbulent-flows
[Accessed 23 3 2019].

Sodja, J., 2007. *Turbulence Models in CFD,* Ljubljana: University of Ljubljana.

Soso , M. & Selig, M. S., 2002. *An Angle of Attack Correction Scheme for the Design of Low Aspect Ratio Wings With Endplates,* Indiana: SAE International.

symscape, 2013. *Caedium v5 Sneak Peek: Polyhedral Meshes Improve CFD.* [Online]
Available at: www.symscape.com/blog/caedium-v5-sneak-peek-polyhedral-meshes-improve-cfd
[Accessed 23 3 2019].

The Great Soviet Encylopedia, 1979. *The Great Soviet Encylopedia.* 3 ed. s.l.:The Gale Group.

Toet, W., 2019. *Willem Toet explains…CFD Post Processing.* London: Race Tech Motorsport Engineering.

Tudor, T., 2018. *Full Wing Case Study* [Interview] (15 10 2018).

uk.comsol.com, 2017. *Navier-Stokes Equations.* [Online]
Available at: uk.comsol.com/multiphysics/navier-stokes-equations
[Accessed 23 3 2019].

University of Wales Trinity Saint David, 2018. *Team MCR Triumph at Castle Combe.* [Online]
Available at: www.uwtsd.ac.uk/news/press-releases/press-2018/team-mcr-triumph-at-castle-combe-.html
[Accessed 22 11 2018].

Versteeg, H. K. & Malalasekera, W., 1995. *An Introduction to Computationa Fluid Dynamics: The Finite Volume Method.* 1 ed. Harlow: Longman Group.

www.caeses.com, 2018. *Simulation-Driven Design of a Race Car Rear Wing.* [Online]
Available at: www.caeses.com/blog/2018/simulation-driven-design-of-a-race-car-rear-wing/
[Accessed 6 4 2019].

www.grc.nasa.gov, 2018. *Density Effects on Aerodynamic Forces.* [Online]
Available at: www.grc.nasa.gov/www/k-12/airplane/density.html
[Accessed 16 3 2019].

Zhang, X., Toet, W. & Zerihan, J., 2006. *Ground Effect Aerodynamics of Race Cars,* Southampton: University of Southampton.

# 9.0.0 Appendix A

| | DRAG (N) | DOWNFORCE (N) | DOWNFORCE (KG) | EFFICIENCY | BALANCE (% Front) | FRONT DOWNFORCE (N) | REAR DOWNFORCE (N) | CoP Distance Behind Coord (m) | | | Drag Cd | Lift Cl |
|---|---|---|---|---|---|---|---|---|---|---|---|---|
| Naca 0009 1° | 50.18 | 837.23 | 85.3 | 16.68 | 57.19 | 478.81 | 358.42 | 0.031 | 0.428699 | 0.571901 | 0.19 | -3.17 |
| Naca 0011 1° | 44.90 | 758.00 | 77.3 | 16.88 | 55.68 | 422.03 | 335.97 | 0.037 | 0.443231 | 0.556769 | 0.17 | -2.87 |
| Naca 0012 1° | 44.90 | 681.40 | 69.5 | 15.18 | 54.92 | 374.23 | 307.17 | 0.04 | 0.450797 | 0.549203 | 0.17 | -2.58 |
| Naca 64A010 1° | 44.90 | 723.66 | 73.8 | 16.12 | 57.44 | 415.69 | 307.97 | 0.035 | 0.425578 | 0.574422 | 0.17 | -2.74 |
| Naca 651412 1° | 71.31 | 1521.27 | 155.1 | 21.33 | 58.70 | 893.04 | 628.24 | 0.025 | 0.412968 | 0.587032 | 0.27 | -5.76 |
| Naca 2212 1° | 60.75 | 1238.68 | 126.3 | 20.39 | 56.18 | 695.90 | 542.77 | 0.035 | 0.438187 | 0.561813 | 0.23 | -4.69 |
| Naca 4415 1° | 73.95 | 1341.68 | 136.8 | 18.14 | 51.39 | 689.48 | 652.20 | 0.054 | 0.486104 | 0.513896 | 0.28 | -5.08 |
| Naca 23012 1° | 52.82 | 1043.23 | 106.3 | 19.75 | 58.20 | 607.15 | 436.08 | 0.027 | 0.418012 | 0.581988 | 0.2 | -3.95 |
| **NACA 4412 HEIGHT STUDY** | | | | | | | | | | | | |
| 10 | 103.00 | 1080.21 | 110.1 | 10.49 | 45.94 | 495.18 | 585.03 | 0.078 | 0.541587 | 0.458413 | 0.39 | -4.07 |
| 20 | 103.00 | 1436.76 | 146.5 | 13.95 | 50.38 | 723.85 | 712.91 | 0.058 | 0.496192 | 0.503808 | 0.39 | -5.44 |
| 30 | 89.88 | 1537.12 | 156.7 | 17.12 | 52.65 | 809.30 | 727.82 | 0.049 | 0.473494 | 0.526506 | 0.34 | -5.82 |
| 40 | 79.23 | 1613.71 | 164.5 | 20.37 | 53.66 | 865.91 | 747.80 | 0.045 | 0.463407 | 0.536593 | 0.3 | -6.11 |
| 50 | 73.95 | 1510.71 | 154.0 | 20.43 | 53.41 | 806.83 | 703.88 | 0.046 | 0.465929 | 0.534071 | 0.28 | -5.72 |
| 60 | 68.67 | 1391.66 | 141.9 | 20.27 | 53.15 | 739.94 | 651.03 | 0.047 | 0.468451 | 0.531549 | 0.26 | -5.27 |
| 70 | 66.09 | 1315.27 | 134.1 | 19.92 | 52.90 | 695.81 | 619.45 | 0.048 | 0.470972 | 0.529028 | 0.25 | -4.98 |
| 80 | 60.75 | 1233.39 | 125.7 | 20.30 | 52.65 | 649.39 | 584.01 | 0.049 | 0.473494 | 0.526506 | 0.23 | -4.67 |
| 90 | 58.10 | 1154.16 | 117.7 | 19.86 | 52.40 | 604.76 | 549.40 | 0.05 | 0.476016 | 0.523984 | 0.22 | -4.37 |
| 100 | 58.10 | 1119.83 | 114.2 | 19.27 | 52.15 | 583.95 | 535.88 | 0.051 | 0.478538 | 0.521462 | 0.22 | -4.24 |
| 110 | 55.46 | 1063.72 | 108.5 | 19.14 | 51.89 | 550.97 | 512.75 | 0.052 | 0.48106 | 0.51894 | 0.21 | -4.03 |
| 120 | 52.82 | 1022.11 | 104.2 | 19.35 | 51.64 | 527.83 | 494.27 | 0.053 | 0.483582 | 0.516418 | 0.2 | -3.87 |
| 130 | 52.82 | 1000.98 | 102.0 | 18.95 | 51.39 | 514.40 | 486.58 | 0.054 | 0.486104 | 0.513896 | 0.2 | -3.79 |
| 140 | 52.82 | 961.36 | 98.0 | 18.20 | 51.14 | 491.61 | 469.75 | 0.055 | 0.488626 | 0.511374 | 0.2 | -3.64 |

| NACA 4412 AoA STUDY | | | | | | | | | | | | |
|---|---|---|---|---|---|---|---|---|---|---|---|---|
| 1 | 79.23 | 1613.71 | 164.5 | 20.37 | 53.66 | 865.91 | 747.80 | 0.045 | 0.463407 | 0.536593 | 0.3 | -6.11 |
| 2 | 92.44 | 1880.46 | 191.7 | 20.34 | 56.69 | 1065.95 | 814.51 | 0.033 | 0.433143 | 0.566857 | 0.35 | -7.12 |
| 3 | 100.36 | 1972.90 | 201.1 | 19.66 | 59.21 | 1168.11 | 804.79 | 0.023 | 0.407924 | 0.592076 | 0.38 | -7.47 |
| 4 | 105.64 | 2078.55 | 211.9 | 19.68 | 61.48 | 1277.83 | 800.71 | 0.014 | 0.385226 | 0.614774 | 0.4 | -7.87 |
| 5 | 113.57 | 2044.21 | 208.4 | 18.00 | 62.99 | 1287.66 | 756.55 | 0.008 | 0.370095 | 0.629905 | 0.43 | -7.74 |
| 6 | 121.49 | 2041.57 | 208.1 | 16.80 | 64.50 | 1316.89 | 724.68 | 0.002 | 0.354963 | 0.645037 | 0.46 | -7.73 |
| 7 | 126.77 | 1964.98 | 200.3 | 15.50 | 65.64 | 1289.78 | 675.19 | -0.0025 | 0.343614 | 0.656386 | 0.48 | -7.44 |
| 8 | 134.70 | 1917.44 | 195.5 | 14.24 | 66.50 | 1275.02 | 642.42 | -0.0059 | 0.33504 | 0.66496 | 0.51 | -7.26 |
| 9 | 137.34 | 1772.18 | 180.7 | 12.90 | 67.15 | 1190.05 | 582.13 | -0.0085 | 0.328483 | 0.671517 | 0.52 | -6.71 |
| 10 | 142.62 | 1661.25 | 169.3 | 11.65 | 67.66 | 1123.94 | 537.31 | -0.0105 | 0.323439 | 0.676561 | 0.54 | -6.29 |
| 11 | 147.90 | 1560.89 | 159.1 | 10.55 | 67.93 | 1060.37 | 500.52 | -0.0116 | 0.320665 | 0.679335 | 0.56 | -5.91 |
| 12 | 150.54 | 974.57 | 99.3 | 6.47 | 64.50 | 628.63 | 345.94 | 0.002 | 0.354963 | 0.645037 | 0.57 | -3.69 |
| 13 | 155.82 | 924.39 | 94.2 | 5.93 | 64.25 | 593.93 | 330.45 | 0.003 | 0.357485 | 0.642515 | 0.59 | -3.5 |
| 14 | 155.82 | 884.77 | 90.2 | 5.68 | 64.76 | 572.94 | 311.83 | 0.001 | 0.352441 | 0.647559 | 0.59 | -3.35 |
| 15 | 155.82 | 818.74 | 83.5 | 5.25 | 64.38 | 527.09 | 291.66 | 0.0025 | 0.356224 | 0.643776 | 0.59 | -3.1 |
| S1223 HEIGHT STUDY | | | | | | | | | | | | |
| 10 | 227.13 | 1117.19 | 113.9 | 4.92 | 47.86 | 534.67 | 582.51 | 0.068 | 0.521411 | 0.478589 | 0.86 | -4.23 |
| 20 | 206.01 | 1378.65 | 140.5 | 6.69 | 45.84 | 631.99 | 746.66 | 0.076 | 0.541587 | 0.458413 | 0.78 | -5.22 |
| 30 | 208.65 | 2878.80 | 293.5 | 13.80 | 44.83 | 1290.64 | 1588.16 | 0.08 | 0.551675 | 0.448325 | 0.79 | -10.9 |
| 40 | 198.08 | 2992.37 | 305.0 | 15.11 | 44.83 | 1341.55 | 1650.81 | 0.08 | 0.551675 | 0.448325 | 0.75 | -11.33 |
| 50 | 187.52 | 2828.62 | 288.3 | 15.08 | 44.08 | 1246.74 | 1581.88 | 0.083 | 0.55924 | 0.44076 | 0.71 | -10.71 |
| 60 | 182.24 | 2762.59 | 281.6 | 15.16 | 43.57 | 1203.70 | 1558.89 | 0.085 | 0.564284 | 0.435716 | 0.69 | -10.46 |
| 70 | 176.95 | 2683.36 | 273.5 | 15.16 | 43.07 | 1155.65 | 1527.71 | 0.087 | 0.569328 | 0.430672 | 0.67 | -10.16 |
| 80 | 169.03 | 2577.71 | 262.8 | 15.25 | 42.56 | 1097.15 | 1480.57 | 0.089 | 0.574372 | 0.425628 | 0.64 | -9.76 |
| 90 | 166.39 | 2524.89 | 257.4 | 15.17 | 42.18 | 1065.11 | 1459.78 | 0.0905 | 0.578155 | 0.421845 | 0.63 | -9.56 |
| 100 | 163.75 | 2416.61 | 246.3 | 14.76 | 41.81 | 1010.29 | 1406.31 | 0.092 | 0.581938 | 0.418062 | 0.62 | -9.15 |
| 110 | 158.47 | 2371.71 | 241.8 | 14.97 | 41.30 | 979.56 | 1392.15 | 0.094 | 0.586982 | 0.413018 | 0.6 | -8.98 |
| 120 | 158.47 | 2321.53 | 236.6 | 14.65 | 41.05 | 952.98 | 1368.55 | 0.095 | 0.589504 | 0.410496 | 0.6 | -8.79 |
| 130 | 155.82 | 2260.78 | 230.5 | 14.51 | 40.55 | 916.64 | 1344.14 | 0.097 | 0.594548 | 0.405452 | 0.59 | -8.56 |
| 140 | 153.18 | 2205.32 | 224.8 | 14.40 | 40.29 | 888.59 | 1316.73 | 0.098 | 0.59707 | 0.40293 | 0.58 | -8.35 |

| | | | | | | | | | | | | |
|---|---|---|---|---|---|---|---|---|---|---|---|---|
| **S1223 AoA STUDY** | | | | | | | | | | | | |
| 1 | 198.08 | 2992.37 | 305.0 | 15.11 | 44.83 | 1341.55 | 1650.81 | 0.08 | 0.551675 | 0.448325 | 0.75 | -11.33 |
| 2 | 206.01 | 2778.44 | 283.2 | 13.49 | 45.59 | 1266.67 | 1511.77 | 0.077 | 0.544109 | 0.455891 | 0.78 | -10.52 |
| 3 | 208.65 | 2812.77 | 286.7 | 13.48 | 47.86 | 1346.16 | 1466.61 | 0.068 | 0.521411 | 0.478589 | 0.79 | -10.65 |
| 4 | 216.57 | 2720.33 | 277.3 | 12.56 | 49.12 | 1336.22 | 1384.11 | 0.063 | 0.508802 | 0.491198 | 0.82 | -10.3 |
| 5 | 221.85 | 2651.66 | 270.3 | 11.95 | 50.38 | 1335.93 | 1315.73 | 0.058 | 0.496192 | 0.503808 | 0.84 | -10.04 |
| 6 | 227.13 | 2575.07 | 262.5 | 11.34 | 51.39 | 1323.32 | 1251.75 | 0.054 | 0.486104 | 0.513896 | 0.86 | -9.75 |
| 7 | 232.42 | 2509.05 | 255.8 | 10.80 | 52.40 | 1314.70 | 1194.35 | 0.05 | 0.476016 | 0.523984 | 0.88 | -9.5 |
| 8 | 229.78 | 2260.78 | 230.5 | 9.84 | 52.90 | 1196.02 | 1064.77 | 0.048 | 0.470972 | 0.529028 | 0.87 | -8.56 |
| 9 | 229.78 | 2073.26 | 211.3 | 9.02 | 53.15 | 1102.04 | 971.22 | 0.047 | 0.468451 | 0.531549 | 0.87 | -7.85 |
| 10 | 229.78 | 1904.23 | 194.1 | 8.29 | 53.15 | 1012.19 | 892.04 | 0.047 | 0.468451 | 0.531549 | 0.87 | -7.21 |
| 11 | 235.06 | 1861.98 | 189.8 | 7.92 | 53.91 | 1003.82 | 858.16 | 0.044 | 0.460885 | 0.539115 | 0.89 | -7.05 |
| 12 | 235.06 | 1724.64 | 175.8 | 7.34 | 54.16 | 934.13 | 790.51 | 0.043 | 0.458363 | 0.541637 | 0.89 | -6.53 |
| 13 | 235.06 | 1090.77 | 111.2 | 4.64 | 45.59 | 497.27 | 593.50 | 0.077 | 0.544109 | 0.455891 | 0.89 | -4.13 |
| 14 | 240.34 | 1061.72 | 108.2 | 4.42 | 45.59 | 484.03 | 577.69 | 0.077 | 0.544109 | 0.455891 | 0.91 | -4.02 |
| 15 | 242.98 | 1043.23 | 106.3 | 4.29 | 46.35 | 483.49 | 559.74 | 0.074 | 0.536543 | 0.463457 | 0.92 | -3.95 |
| **S1223 MAIN PLANE DOE STUDY** | | | | | | | | | | | | |
| 40/1.95 | 203.36 | 2878.80 | 293.5 | 14.16 | 46.35 | 1334.20 | 1544.60 | 0.074 | 0.536543 | 0.463457 | 0.77 | -10.9 |
| 40/7.41 | 229.78 | 2392.84 | 243.9 | 10.41 | 53.15 | 1271.91 | 1120.93 | 0.047 | 0.468451 | 0.531549 | 0.87 | -9.06 |
| 40/13 | 240.34 | 1125.11 | 114.7 | 4.68 | 45.84 | 515.76 | 609.34 | 0.076 | 0.541587 | 0.458413 | 0.91 | -4.26 |
| 75/2.86 | 184.88 | 2627.89 | 267.9 | 14.21 | 46.35 | 1217.92 | 1409.98 | 0.074 | 0.536543 | 0.463457 | 0.7 | -9.95 |
| 82.5/13 | 213.93 | 1357.53 | 138.4 | 6.35 | 50.13 | 680.51 | 677.02 | 0.059 | 0.498714 | 0.501286 | 0.81 | -5.14 |
| 82.5222/7.42384 | 208.65 | 2424.53 | 247.1 | 11.62 | 51.64 | 1252.07 | 1172.46 | 0.053 | 0.483582 | 0.516418 | 0.79 | -9.18 |
| 103/0 | 142.62 | 2139.29 | 218.1 | 15.00 | 39.28 | 840.40 | 1298.89 | 0.102 | 0.607157 | 0.392843 | 0.54 | -8.1 |
| 118./8.385 | 203.36 | 2234.37 | 227.8 | 10.99 | 50.89 | 1136.96 | 1097.41 | 0.056 | 0.491148 | 0.508852 | 0.77 | -8.46 |
| 125/13 | 219.21 | 1891.03 | 192.8 | 8.63 | 52.65 | 995.64 | 895.39 | 0.049 | 0.473494 | 0.526506 | 0.83 | -7.16 |
| 140/0 | 132.06 | 1946.49 | 198.4 | 14.74 | 38.02 | 740.12 | 1206.37 | 0.107 | 0.619767 | 0.380233 | 0.5 | -7.37 |
| 140/4.68 | 174.31 | 2226.45 | 227.0 | 12.77 | 46.09 | 1026.25 | 1200.20 | 0.075 | 0.539065 | 0.460935 | 0.66 | -8.43 |

| S1223 MAIN PLANE DOE OPTIMISATION STUDY | | | | | | | | | | | | |
|---|---|---|---|---|---|---|---|---|---|---|---|---|
| 60/0.00000304 | 157.57 | 2405.50 | 245.2 | 15.27 | 41.30 | 993.52 | 1411.99 | 0.094 | 0.586982 | 0.413018 | 0.6 | -9.16 |
| 60/1.47 | 183.78 | 2748.83 | 280.2 | 14.96 | 44.96 | 1235.84 | 1512.99 | 0.0795 | 0.550414 | 0.449586 | 0.7 | -10.47 |
| 60/0.19 | 162.83 | 2505.47 | 255.4 | 15.39 | 42.31 | 1060.08 | 1445.39 | 0.09 | 0.576894 | 0.423106 | 0.62 | -9.54 |
| 60/0.59 | 174.31 | 2641.10 | 269.2 | 15.15 | 43.19 | 1140.78 | 1500.32 | 0.0865 | 0.568067 | 0.431933 | 0.66 | -10 |
| 60/0.96 | 179.59 | 2709.77 | 276.2 | 15.09 | 44.08 | 1194.36 | 1515.41 | 0.083 | 0.55924 | 0.44076 | 0.68 | -10.26 |
| 60/4.49 | 203.36 | 2683.36 | 273.5 | 13.19 | 49.75 | 1334.98 | 1348.38 | 0.0605 | 0.502497 | 0.497503 | 0.77 | -10.16 |
| NACA 4412 SECONDARY ELEMENT DOE STUDY | | | | | | | | | | | | |
| 19.7995/1.18671/29.0138 | 185.67 | 2729.84 | 278.3 | 14.70 | 40.42 | 1103.38 | 1626.46 | 0.0975 | 0.595809 | 0.404191 | 0.37 | -5.44 |
| 32.115/9.875/8.01002 | 365.66 | 3790.51 | 386.4 | 10.37 | 26.17 | 991.98 | 2798.52 | 0.154 | 0.738298 | 0.261702 | 0.71 | -7.36 |
| 5/8.75/36.25 | 307.03 | 3303.03 | 336.7 | 10.76 | 32.85 | 1085.15 | 2217.87 | 0.1275 | 0.671467 | 0.328533 | 0.62 | -6.67 |
| 40.357/0/9.64298 | 206.01 | 2513.27 | 256.2 | 12.20 | 41.81 | 1050.70 | 1462.57 | 0.092 | 0.581938 | 0.418062 | 0.4 | -4.88 |
| 24.6414/5.41415/19.9445 | 284.71 | 3335.18 | 340.0 | 11.71 | 32.60 | 1087.31 | 2247.87 | 0.1285 | 0.673989 | 0.326011 | 0.56 | -6.56 |
| 41.4552/8.54478/0 | 344.27 | 3776.51 | 385.0 | 10.97 | 26.52 | 1001.65 | 2774.86 | 0.1526 | 0.734767 | 0.265233 | 0.66 | -7.24 |
| 13.1235/11/25.8765 | 371.14 | 3680.90 | 375.2 | 9.92 | 28.31 | 1042.20 | 2638.70 | 0.1455 | 0.716862 | 0.283138 | 0.73 | -7.24 |
| 5/1.125/43.875 | 203.03 | 2436.41 | 248.4 | 12.00 | 43.70 | 1064.66 | 1371.76 | 0.0845 | 0.563023 | 0.436977 | 0.41 | -4.92 |
| 27.7533/0/22.2467 | 205.21 | 2423.74 | 247.1 | 11.81 | 39.91 | 967.43 | 1456.31 | 0.0995 | 0.600852 | 0.399148 | 0.37 | -4.37 |
| 12.9754/0/37.0246 | 194.91 | 2273.99 | 231.8 | 11.67 | 41.43 | 942.07 | 1331.92 | 0.0935 | 0.585721 | 0.414279 | 0.36 | -4.2 |
| 22.8278/11/16.1722 | 410.43 | 3954.52 | 403.1 | 9.64 | 21.68 | 857.38 | 3097.13 | 0.1718 | 0.783189 | 0.216811 | 0.74 | -7.13 |
| 48.8995/1.10051/0 | 234.73 | 2884.54 | 294.0 | 12.29 | 38.40 | 1107.71 | 1776.83 | 0.1055 | 0.615984 | 0.384016 | 0.45 | -5.53 |

| | | | | | | | | | | | | |
|---|---|---|---|---|---|---|---|---|---|---|---|---|
| **S1223 SECONDARY ELEMENT DOE STUDY** | | | | | | | | | | | | |
| 41.6686/8.33141/0 | 537.27 | 4731.07 | 482.3 | 8.81 | 11.01 | 521.05 | 4210.02 | 0.2141 | 0.889867 | 0.110133 | 1.03 | -9.07 |
| 49.3089/0.691099/0 | 427.73 | 3776.51 | 385.0 | 8.83 | 28.94 | 1093.08 | 2683.42 | 0.143 | 0.710557 | 0.289443 | 0.82 | -7.24 |
| 24.153/12/13.847 | 427.73 | 3776.51 | 385.0 | 8.83 | 12.05 | 454.97 | 3321.54 | 0.21 | 0.879527 | 0.120473 | 0.82 | -7.24 |
| 5/1.125/43.875 | 475.40 | 3694.24 | 376.6 | 7.77 | 34.39 | 1270.51 | 2423.73 | 0.1214 | 0.656083 | 0.343917 | 0.96 | -7.46 |
| 32.3459/12/5.65405 | 607.72 | 4614.53 | 470.4 | 7.59 | 10.03 | 462.83 | 4151.70 | 0.218 | 0.899702 | 0.100298 | 1.18 | -8.96 |
| 23.2449/6.03753/20.7176 | 452.49 | 4133.39 | 421.3 | 9.13 | 19.69 | 813.81 | 3319.57 | 0.1797 | 0.803112 | 0.196888 | 0.89 | -8.13 |
| 27.0619/0/22.9381 | 442.32 | 3665.65 | 373.7 | 8.29 | 31.37 | 1149.74 | 2515.90 | 0.1334 | 0.686346 | 0.313654 | 0.87 | -7.21 |
| 5/9.75/35.25 | 455.59 | 3738.81 | 381.1 | 8.21 | 23.50 | 878.50 | 2860.30 | 0.1646 | 0.765031 | 0.234969 | 0.92 | -7.55 |
| 12.544/12/25.456 | 567.04 | 4270.39 | 435.3 | 7.53 | 14.32 | 611.39 | 3659.00 | 0.201 | 0.856829 | 0.143171 | 1.13 | -8.51 |
| 15.9302/0/34.0698 | 461.66 | 3693.31 | 376.5 | 8.00 | 32.58 | 1203.13 | 2490.18 | 0.1286 | 0.674241 | 0.325759 | 0.92 | -7.36 |
| 32.2939/4.08531/13.6208 | 417.16 | 3790.51 | 386.4 | 9.09 | 24.78 | 939.41 | 2851.10 | 0.1595 | 0.752169 | 0.247831 | 0.81 | -7.36 |
| 41.2288/0/8.77123 | 437.76 | 3723.55 | 379.6 | 8.51 | 29.88 | 1112.50 | 2611.05 | 0.1393 | 0.701226 | 0.298774 | 0.85 | -7.23 |
| **NACA 4412 SECONDARY ELEMENT DOE OPTIMISATION STUDY** | | | | | | | | | | | | |
| 46.37/3.62/0 | 271.24 | 3343.57 | 340.8 | 12.33 | 33.00 | 1103.53 | 2240.03 | 0.1269 | 0.669954 | 0.330046 | 0.52 | -6.41 |
| 5/4.91/40 | 252.36 | 3090.09 | 315.0 | 12.24 | 31.37 | 969.22 | 2120.87 | 0.1334 | 0.686346 | 0.313654 | 0.49 | -6 |
| **S1223 SECONDARY ELEMENT DOE OPTIMISATION STUDY** | | | | | | | | | | | | |
| 43.7/6.29/0 | 495.54 | 4595.45 | 468.4 | 9.27 | 12.50 | 574.49 | 4020.96 | 0.2082 | 0.874987 | 0.125013 | 0.95 | -8.81 |
| 6.56/2.36/41.06 | 435.78 | 3501.11 | 356.9 | 8.03 | 34.90 | 1221.75 | 2279.36 | 0.1194 | 0.651039 | 0.348961 | 0.88 | -7.07 |
| 5/2.59/42.4 | 453.21 | 3651.45 | 372.2 | 8.06 | 34.87 | 1273.29 | 2378.16 | 0.1195 | 0.651291 | 0.348709 | 0.88 | -7.09 |

| | | | | | | | | | | | | |
|---|---|---|---|---|---|---|---|---|---|---|---|---|
| 60/0.00000304 | 157.57 | 2405.50 | 245.2 | 15.27 | 41.30 | 993.52 | 1411.99 | 0.094 | 0.586982 | 0.413018 | 0.6 | -9.16 |
| 60/1.47 | 183.78 | 2748.83 | 280.2 | 14.96 | 44.96 | 1235.84 | 1512.99 | 0.0795 | 0.550414 | 0.449586 | 0.7 | -10.47 |
| 60/0.19 | 162.83 | 2505.47 | 255.4 | 15.39 | 42.31 | 1060.08 | 1445.39 | 0.09 | 0.576894 | 0.423106 | 0.62 | -9.54 |
| 60/0.59 | 174.31 | 2641.10 | 269.2 | 15.15 | 43.19 | 1140.78 | 1500.32 | 0.0865 | 0.568067 | 0.431933 | 0.66 | -10 |
| 60/0.96 | 179.59 | 2709.77 | 276.2 | 15.09 | 44.08 | 1194.36 | 1515.41 | 0.083 | 0.55924 | 0.44076 | 0.68 | -10.26 |
| 60/4.49 | 203.36 | 2683.36 | 273.5 | 13.19 | 49.75 | 1334.98 | 1348.38 | 0.0605 | 0.502497 | 0.497503 | 0.77 | -10.16 |
| **S1223 SECONDARY ELEMENT DOE CHORD STUDY (Increased Angle of Attack & Chord Length Changes)** | | | | | | | | | | | | |
| 5/0/62.5 | 321.16 | 3220.03 | 328.2 | 10.03 | 36.38 | 1171.58 | 2048.45 | 0.1135 | 0.63616 | 0.36384 | 0.76 | -7.62 |
| 27.5/10/62.5 | 435.25 | 4098.99 | 417.8 | 9.42 | 25.04 | 1026.19 | 3072.79 | 0.1585 | 0.749647 | 0.250353 | 1.03 | -9.7 |
| 5/10/25 | 350.74 | 4284.92 | 436.8 | 12.22 | 40.44 | 1733.01 | 2551.91 | 0.0974 | 0.595556 | 0.404444 | 0.83 | -10.14 |
| 5/10/100 | 552.91 | 4699.77 | 479.1 | 8.50 | 9.20 | 432.26 | 4267.51 | 0.2213 | 0.908025 | 0.091975 | 1.06 | -9.01 |
| 5/20/62.5 | 511.65 | 3631.45 | 370.2 | 7.10 | 22.65 | 822.60 | 2808.85 | 0.16795 | 0.773479 | 0.226521 | 1.23 | -8.73 |
| 27.5/0/25 | 260.81 | 3113.20 | 317.3 | 11.94 | 43.32 | 1348.62 | 1764.58 | 0.086 | 0.566806 | 0.433194 | 0.79 | -9.43 |
| 27.5/20/25 | 378.54 | 3471.53 | 353.9 | 9.17 | 34.87 | 1210.55 | 2260.98 | 0.1195 | 0.651291 | 0.348709 | 1.17 | -10.73 |
| 27.5/0/100 | 406.86 | 3672.19 | 374.3 | 9.03 | 27.68 | 1016.58 | 2655.60 | 0.148 | 0.723167 | 0.276833 | 0.78 | -7.04 |
| 27.5/20/100 | 721.94 | 4224.90 | 430.7 | 5.85 | 5.82 | 245.81 | 3979.09 | 0.2347 | 0.941819 | 0.058181 | 1.42 | -8.31 |
| 50/0/62.5 | 354.96 | 3655.28 | 372.6 | 10.30 | 36.13 | 1320.72 | 2334.56 | 0.1145 | 0.638682 | 0.361318 | 0.84 | -8.65 |
| 50/10/25 | 300.89 | 3494.18 | 356.2 | 11.61 | 37.27 | 1302.16 | 2192.01 | 0.11 | 0.627333 | 0.372667 | 0.93 | -10.8 |
| 50/20/62.5 | 561.56 | 3781.20 | 385.4 | 6.73 | 18.76 | 709.19 | 3072.01 | 0.1834 | 0.812443 | 0.187557 | 1.35 | -9.09 |
| 50/10/100 | 589.43 | 4971.01 | 506.7 | 8.43 | 9.32 | 463.48 | 4507.53 | 0.2208 | 0.906764 | 0.093236 | 1.13 | -9.53 |

| | | | | | | | | | | | | |
|---|---|---|---|---|---|---|---|---|---|---|---|---|
| **S1223 SECONDARY ELEMENT DOE OPTIMISATION 2** | | | | | | | | | | | | |
| 20/10/31.4263 | 326.63 | 3517.32 | 358.5 | 10.77 | 36.11 | 1269.99 | 2247.33 | 0.1146 | 0.638934 | 0.361066 | 0.95 | -10.23 |
| 20.4203/10/31.6473 | 327.18 | 3557.61 | 362.7 | 10.87 | 36.08 | 1283.63 | 2273.97 | 0.1147 | 0.639186 | 0.360814 | 0.95 | -10.33 |
| 20.4851/10.014/31.6994 | 350.61 | 3703.30 | 377.5 | 10.56 | 33.66 | 1246.54 | 2456.76 | 0.1243 | 0.663397 | 0.336603 | 0.96 | -10.14 |
| 20/10/31.995 | 328.03 | 3518.56 | 358.7 | 10.73 | 35.90 | 1263.33 | 2255.22 | 0.1154 | 0.640951 | 0.359049 | 0.95 | -10.19 |
| 20/10/32.0409 | 328.14 | 3550.85 | 362.0 | 10.82 | 36.06 | 1280.30 | 2270.55 | 0.1148 | 0.639438 | 0.360562 | 0.95 | -10.28 |
| 20.9523/10/31.9162 | 327.83 | 3561.32 | 363.0 | 10.86 | 36.13 | 1286.77 | 2274.55 | 0.1145 | 0.638682 | 0.361318 | 0.95 | -10.32 |
| 21.2905/10/32.1575 | 324.97 | 3581.61 | 365.1 | 11.02 | 36.26 | 1298.62 | 2282.99 | 0.114 | 0.637421 | 0.362579 | 0.94 | -10.36 |
| 20.0001/10.1557/31.6735 | 327.20 | 3533.79 | 360.2 | 10.80 | 35.96 | 1270.58 | 2263.20 | 0.1152 | 0.640447 | 0.359553 | 0.95 | -10.26 |
| 21.5747/10/32.2315 | 325.15 | 3549.00 | 361.8 | 10.91 | 36.06 | 1279.63 | 2269.37 | 0.1148 | 0.639438 | 0.360562 | 0.94 | -10.26 |
| 20.0001/10/32.9771 | 330.44 | 3600.09 | 367.0 | 10.89 | 35.80 | 1288.98 | 2311.12 | 0.1158 | 0.64196 | 0.35804 | 0.95 | -10.35 |
| **S1223 SECONDARY ELEMENT NEGATIVE OVERHANG STUDY** | | | | | | | | | | | | |
| 21.2905/10/32.1575/-10 | 325.59 | 3630.01 | 370.0 | 11.15 | 35.25 | 1279.55 | 2350.46 | 0.118 | 0.647508 | 0.352492 | 0.94 | -10.48 |
| 21.2905/10/32.1575/-20 | 318.66 | 3657.69 | 372.9 | 11.48 | 34.37 | 1257.02 | 2400.67 | 0.1215 | 0.656335 | 0.343665 | 0.92 | -10.56 |
| 21.2905/10/32.1575/-30 | 315.20 | 3657.66 | 372.9 | 11.60 | 33.61 | 1229.34 | 2428.32 | 0.1245 | 0.663901 | 0.336099 | 0.91 | -10.56 |
| 21.2905/10/32.1575/-40 | 339.44 | 3668.02 | 373.9 | 10.81 | 32.60 | 1195.82 | 2472.21 | 0.1285 | 0.673989 | 0.326011 | 0.98 | -10.59 |
| 21.2905/10/32.1575/-50 | 308.26 | 3643.75 | 371.4 | 11.82 | 31.79 | 1158.50 | 2485.25 | 0.1317 | 0.682059 | 0.317941 | 0.89 | -10.52 |
| | | | | | | | | | | | | |
| S1223 60/1.47/21.2905/10/32.1575/-30 (END PLATE TEST) | 183.58 | 2396.88 | 244.3 | 13.06 | 35.10 | 841.25 | 1555.62 | 0.1186 | 0.649021 | 0.350979 | 0.53 | -6.92 |
| S1223 60/1.47/21.2905/10/32.1575/-30 (3 ELEMENT TEST) | 349.75 | 4134.13 | 421.4 | 11.82 | 21.38 | 883.82 | 3250.32 | 0.173 | 0.786215 | 0.213785 | 0.89 | -10.52 |
| S1223 40/1.47/21.2905/10/32.1575/-30 | 332.51 | 3688.83 | 376.0 | 11.09 | 34.24 | 1263.07 | 2425.76 | 0.122 | 0.657596 | 0.342404 | 0.96 | -10.65 |
| S1223 40/1.47/21.2905/10/32.1575/-30 (MODIFIED MAIN PLANE) | 330.35 | 3909.11 | 398.5 | 11.83 | 33.23 | 1299.06 | 2610.05 | 0.126 | 0.667684 | 0.332316 | 0.96 | -11.36 |
| | | | | | | | | | | | | |
| JHTT02 BASELINE SPLITTER (40mm HEIGHT) | 310.78 | 3999.76 | 407.7 | 12.87 | 35.17 | 1406.86 | 2592.91 | 0.1183 | 0.648265 | 0.351735 | 0.77 | -9.91 |

| | DRAG (N) | DOWNFORCE (N) | DOWNFORCE (KG) | EFFICIENCY | BALANCE (% Front) | FRONT DOWNFORCE (N) | REAR DOWNFORCE (N) | CoP Distance Behind Coord (m) | | | Drag Cd | Lift Cl |
|---|---|---|---|---|---|---|---|---|---|---|---|---|
| Baseline (White Car - Windtunnel) | 500 | 382 | 39 | 0.76 | 16.34 | 62 | 319 | 2.17 | 0.83655 | 0.163447 | 0.506 | -0.386 |
| Yellow MCR (50mm Longer Splitter) (Wing Angle 7.36°)(NO GURNEY) | 455 | 662 | 68 | 1.46 | 71.47 | 473 | 189 | 0.74 | 0.28534 | 0.714658 | 0.46 | -0.67 |
| Yellow MCR (JHTT02 Splitter) (Wing Angle 7.36°) (NO GURNEY) | 465 | 890 | 91 | 1.91 | 83.80 | 746 | 144 | 0.42 | 0.16199 | 0.838006 | 0.47 | -0.9 |
| Yellow MCR (John Iley Splitter) (Wing Angle 7.36°) (NO GURNEY) | 475 | 910 | 93 | 1.92 | 75.32 | 686 | 225 | 0.64 | 0.2468 | 0.753204 | 0.48 | -0.92 |
| Yellow MCR (50mm Longer Splitter) (Wing Angle 8.8°) | 490 | 800 | 82 | 1.63 | 51.42 | 411 | 388 | 1.26 | 0.48578 | 0.514218 | 0.49 | -0.80 |
| Yellow MCR (50mm Longer Splitter) (Wing Angle 5.1°) | 455 | 771 | 79 | 1.70 | 59.13 | 456 | 315 | 1.06 | 0.40869 | 0.59131 | 0.46 | -0.78 |
| Yellow MCR (Standard Splitter) (Wing Angle 7.36°)(NO GURNEY) | 455 | 663 | 68 | 1.46 | 61.06 | 405 | 258 | 1.01 | 0.38942 | 0.610583 | 0.46 | -0.67 |
| JHTT02 (OSS BASELINE) (60mm Ride Height) (Splitter 48mm Height) | 500 | 1137 | 116 | 2.27 | 47.18 | 536 | 601 | 1.37 | 0.52818 | 0.471817 | 0.51 | -1.16 |
| JHTT02 Baseline | 529 | 1549 | 158 | 2.93 | 47.56 | 737 | 812 | 1.3601 | 0.52437 | 0.475633 | 0.54 | -1.58 |
| Splitter Concept 1 | 520 | 1215 | 124 | 2.34 | 32.92 | 400 | 815 | 1.74 | 0.6708 | 0.329196 | 0.53 | -1.24 |
| Splitter Concept 2 | 520 | 1245 | 127 | 2.40 | 30.22 | 376 | 869 | 1.81 | 0.69779 | 0.302214 | 0.53 | -1.27 |
| Splitter Concept 3 | 520 | 1255 | 128 | 2.42 | 29.45 | 370 | 885 | 1.83 | 0.7055 | 0.294504 | 0.53 | -1.28 |
| Splitter Concept 4 (0.5° Rake) | 520 | 1304 | 133 | 2.51 | 41.01 | 535 | 769 | 1.53 | 0.58986 | 0.410143 | 0.53 | -1.33 |
| Splitter Concept 5 | 559 | 1598 | 163 | 2.86 | 44.48 | 711 | 887 | 1.44 | 0.55517 | 0.444835 | 0.57 | -1.63 |
| Splitter Concept 6 | 559 | 1529 | 156 | 2.74 | 46.03 | 704 | 825 | 1.4 | 0.53975 | 0.460253 | 0.57 | -1.56 |
| Splitter Concept 7 | 529 | 1549 | 158 | 2.93 | 46.80 | 725 | 824 | 1.38 | 0.53204 | 0.467962 | 0.54 | -1.58 |
| Splitter Concept 8 | 529 | 1578 | 161 | 2.98 | 44.48 | 702 | 876 | 1.44 | 0.55517 | 0.444835 | 0.54 | -1.61 |
| Splitter Concept 9 | 520 | 1451 | 148 | 2.79 | 46.80 | 679 | 772 | 1.38 | 0.53204 | 0.467962 | 0.53 | -1.48 |
| Splitter Concept 10 | 539 | 1559 | 159 | 2.89 | 46.80 | 729 | 829 | 1.38 | 0.53204 | 0.467962 | 0.55 | -1.59 |
| Splitter Concept 11 | 510 | 1264 | 129 | 2.48 | 41.40 | 523 | 741 | 1.52 | 0.586 | 0.413998 | 0.52 | -1.29 |

| | | | | | | | | | | | | |
|---|---|---|---|---|---|---|---|---|---|---|---|---|
| S1223 60/1.47 (60mm Ride Height) | 529 | 951 | 97 | 1.80 | 16.65 | 158 | 792 | 2.162 | 0.83347 | 0.166531 | 0.54 | -0.97 |
| S1223 60/1.47 (40mm Ride Height) | 500 | 1049 | 107 | 2.10 | 13.26 | 139 | 910 | 2.25 | 0.86739 | 0.13261 | 0.51 | -1.07 |
| S1223 40/1.47 (40mm Ride Height) | 490 | 1108 | 113 | 2.26 | 19.27 | 213 | 894 | 2.094 | 0.80726 | 0.192743 | 0.5 | -1.13 |
| S1223 40/1.47 (MODIFIED) 21.2905/10/32.1575/-30 | 549 | 1421 | 145 | 2.59 | 49.90 | 709 | 712 | 1.2995 | 0.50101 | 0.498992 | 0.56 | -1.45 |
| JHTT02 S1223 END PLATE DEVELOPMENT 1 | 549 | 1470 | 150 | 2.68 | 54.52 | 802 | 669 | 1.1795 | 0.45475 | 0.545247 | 0.56 | -1.5 |
| JHTT02 S1223 END PLATE DEVELOPMENT 2 | 559 | 1461 | 149 | 2.61 | 55.60 | 812 | 648 | 1.1516 | 0.444 | 0.556002 | 0.57 | -1.49 |
| JHTT02 S1223 END PLATE DEVELOPMENT 3 | 559 | 1519 | 155 | 2.72 | 54.37 | 826 | 693 | 1.1835 | 0.45629 | 0.543706 | 0.57 | -1.55 |
| JHTT02 S1223 END PLATE DEVELOPMENT 4 | 559 | 1578 | 161 | 2.82 | 56.09 | 885 | 693 | 1.139 | 0.43914 | 0.560859 | 0.57 | -1.61 |
| JHTT02 S1223 END PLATE DEVELOPMENT 5 | 569 | 1608 | 164 | 2.83 | 51.27 | 824 | 783 | 1.264 | 0.48732 | 0.512676 | 0.58 | -1.64 |
| **Attitude Study** | | 137 | | | | | | | | | | |
| JHTT02 S1223 (10mm Ride Height) | 490 | 1186 | 121 | 2.42 | 54.78 | 650 | 536 | 1.173 | 0.45225 | 0.547753 | 0.5 | -1.21 |
| JHTT02 S1223 (20mm Ride Height) | 520 | 1549 | 158 | 2.98 | 55.11 | 854 | 695 | 1.1643 | 0.44889 | 0.551106 | 0.53 | -1.58 |
| JHTT02 S1223 (30mm Ride Height) | 549 | 1539 | 157 | 2.80 | 50.07 | 771 | 768 | 1.295 | 0.49927 | 0.500727 | 0.56 | -1.57 |
| JHTT02 S1223 (40mm Ride Height) | 569 | 1588 | 162 | 2.79 | 53.73 | 853 | 735 | 1.2002 | 0.46273 | 0.537268 | 0.58 | -1.62 |
| JHTT02 S1223 (50mm Ride Height) | 569 | 1382 | 141 | 2.43 | 48.92 | 676 | 706 | 1.325 | 0.51084 | 0.489163 | 0.58 | -1.41 |
| JHTT02 S1223 (60mm Ride Height) | 588 | 1294 | 132 | 2.20 | 45.28 | 586 | 708 | 1.4193 | 0.54719 | 0.452814 | 0.6 | -1.32 |
| JHTT02 S1223 (70mm Ride Height) | 588 | 1088 | 111 | 1.85 | 46.77 | 509 | 579 | 1.3807 | 0.53231 | 0.467693 | 0.6 | -1.11 |
| JHTT02 S1223 (Static 0.25Deg 40mm) | 569 | 1480 | 151 | 2.60 | 55.51 | 822 | 659 | 1.154 | 0.44492 | 0.555077 | 0.58 | -1.51 |
| JHTT02 S1223 (Static 0.5Deg 40mm) | 588 | 1470 | 150 | 2.50 | 58.55 | 861 | 609 | 1.075 | 0.41447 | 0.585528 | 0.6 | -1.5 |
| JHTT02 S1223 (Dynamic 0.25Deg) | 559 | 1617 | 165 | 2.89 | 55.01 | 890 | 728 | 1.1669 | 0.4499 | 0.550104 | 0.57 | -1.65 |
| JHTT02 S1223 (Dynamic 0.5Deg) | 539 | 1715 | 175 | 3.18 | 59.91 | 1028 | 688 | 1.0397 | 0.40086 | 0.599135 | 0.55 | -1.75 |
| JHTT02 S1223 (Yaw 1Deg) | 567 | 1441 | 147 | 2.54 | 52.17 | 752 | 689 | 1.2406 | 0.4783 | 0.521696 | 0.56 | -1.47 |
| JHTT02 S1223 (Yaw 2Deg) | 555 | 1441 | 147 | 2.60 | 51.17 | 737 | 704 | 1.2666 | 0.48833 | 0.511674 | 0.54 | -1.47 |
| JHTT02 S1223 (Yaw 3Deg) | 553 | 1402 | 143 | 2.54 | 52.28 | 733 | 669 | 1.2378 | 0.47722 | 0.522775 | 0.53 | -1.43 |

# 10.0.0 Appendix B

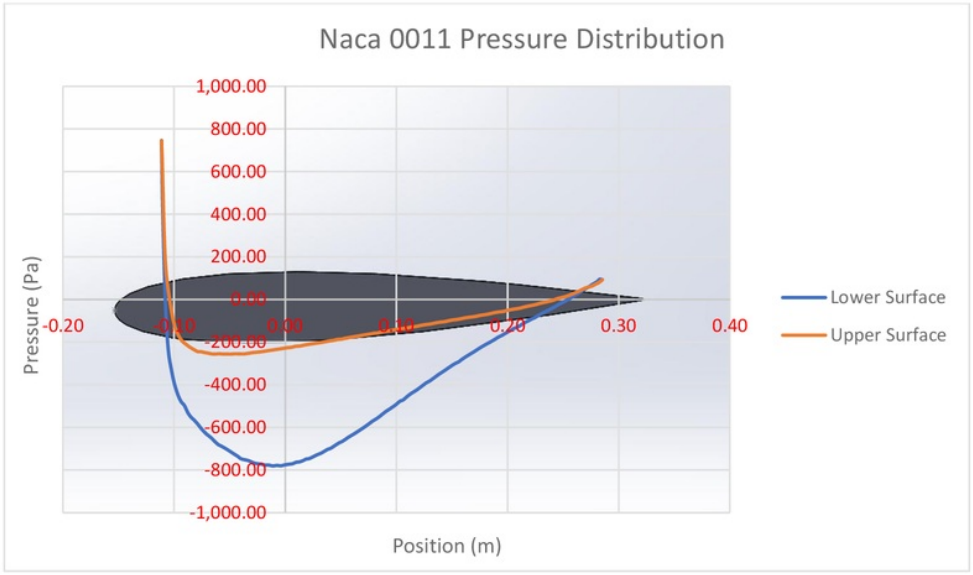
| Domain | |
|---|---|
| X (m) | 5 |
| Y (m) | 1.5 |
| Z (m) | 3 |
| Dis to origin (m) | 1.5 |

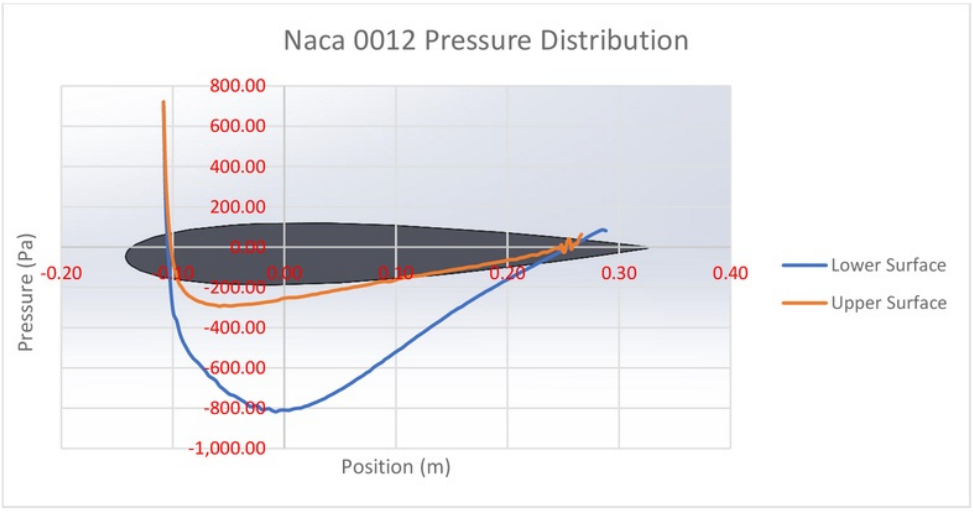
| Density Box | |
|---|---|
| Element size (m) | 0.02 |
| X | 5 |
| Y | 7 |
| Z | 1.5 |

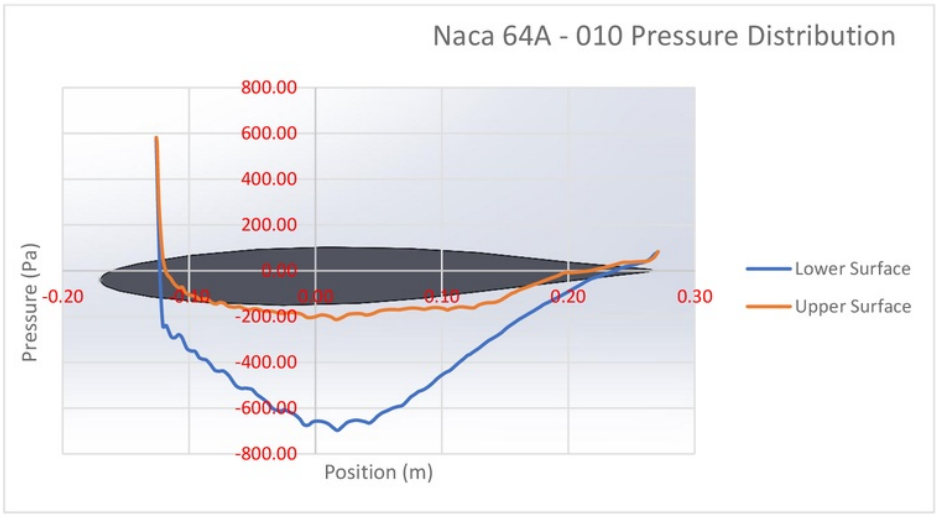
| | |
|---|---|
| Global Mesh (m) | 0.5 |
| Edge Criterion | 0.09 |
| Prism Layers | 5 |
| Part Element Size (m) | 0.004 |

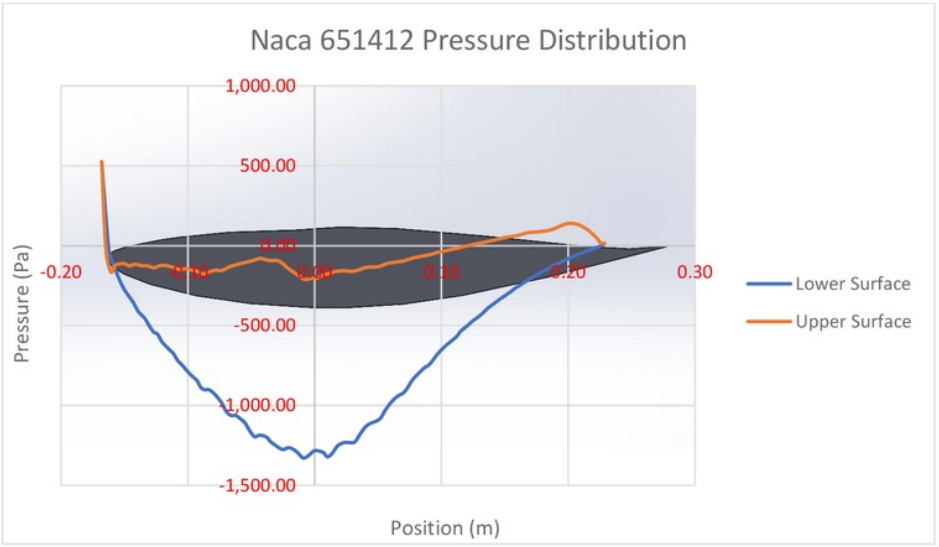
| Aerofoil Dimensions (mm) | |
|---|---|
| Chord | 369.67 |
| Span | 882.3 |
| Distance to Ground | 40 |

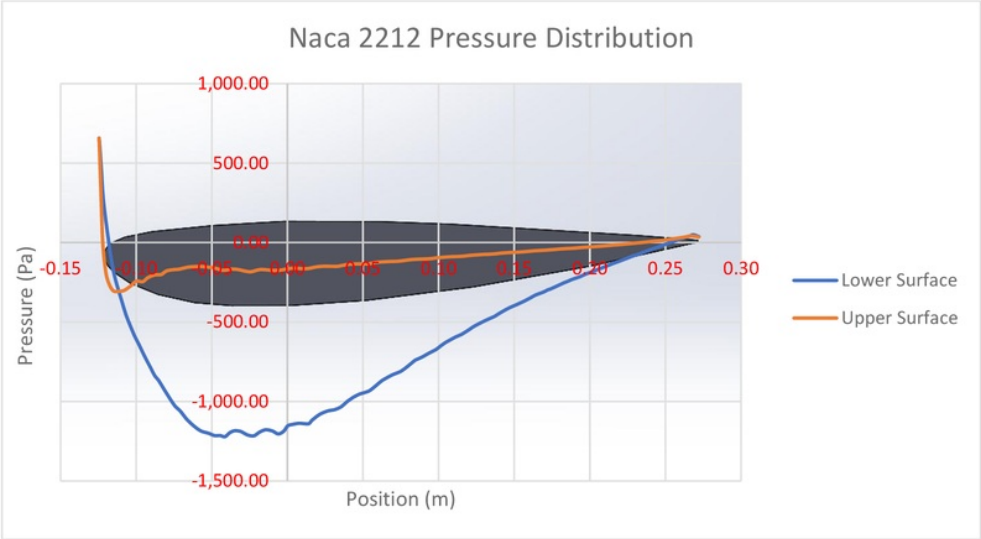
## 11.0.0 Appendix C

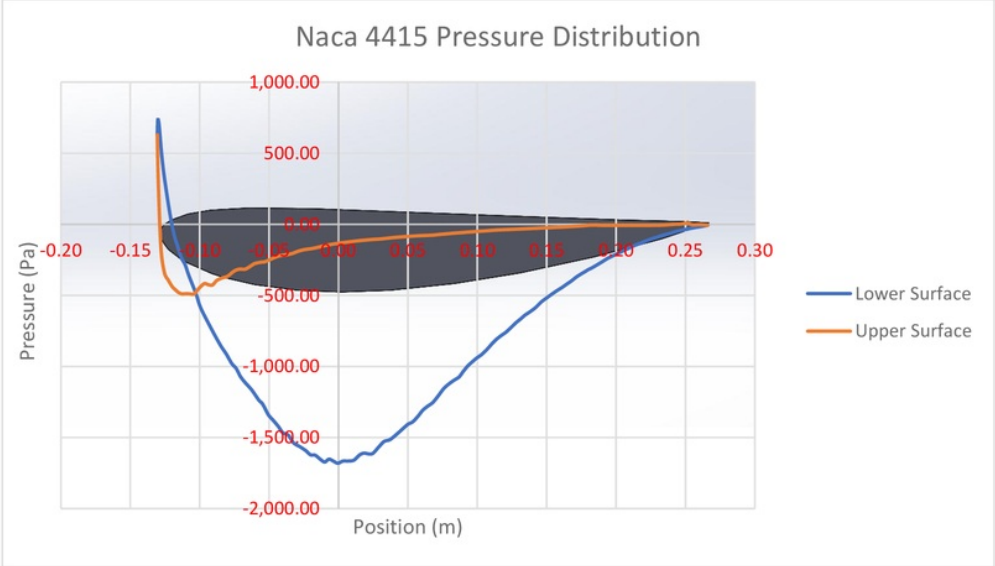


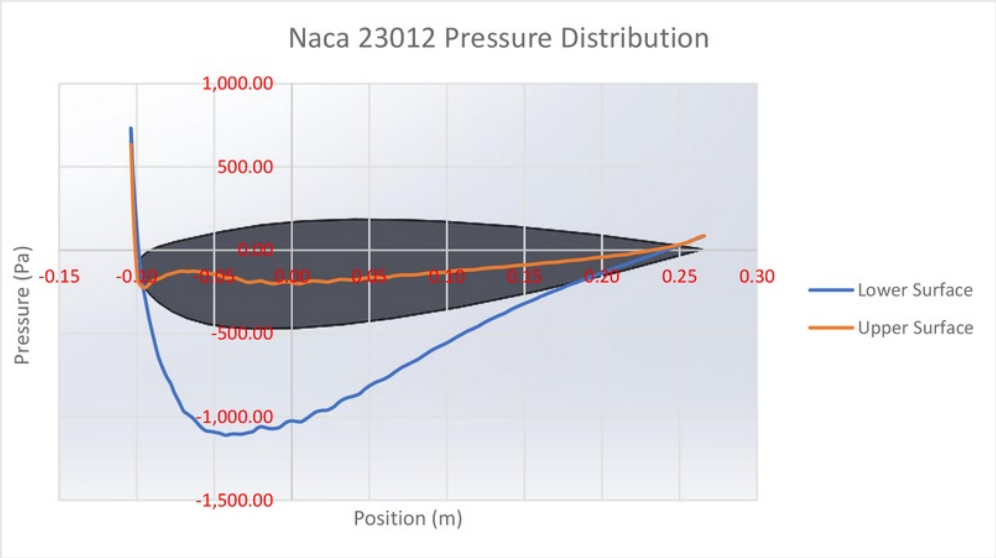




Naca 64A - 010 Pressure Distribution
800.00
600.00
400.00
200.00
0.00
-200.00
-400.00
-600.00
-800.00
-0.20
0.10
0.00
0.10
0.20
0.30
Pressure (Pa)
Position (m)
Lower Surface
Upper Surface


Naca 651412 Pressure Distribution
1,000.00
500.00
0.00
-500.00
-1,000.00
-1,500.00
-0.20
0.10
0.00
0.10
0.20
0.30
Pressure (Pa)
Position (m)
Lower Surface
Upper Surface


Naca 2212 Pressure Distribution
1,000.00
500.00
0.00
-500.00
-1,000.00
-1,500.00
-0.15
0.25
0.30
Pressure (Pa)
Position (m)
Lower Surface
Upper Surface


Naca 4415 Pressure Distribution
1,000.00
500.00
0.00
-500.00
-1,000.00
-1,500.00
-2,000.00
-0.20
-0.15
0.25
0.30
Pressure (Pa)
Position (m)
Lower Surface
Upper Surface


Naca 23012 Pressure Distribution
1,000.00
500.00
0.00
-500.00
-1,000.00
-1,500.00
-0.15
0.25
0.30
Pressure (Pa)
Position (m)
Lower Surface
Upper Surface

# 12.0.0 Appendix D

